INFORMATION TO USERS

This manuscript has been reproduced from the microfilm master. UMI films the text directly from the original or copy submitted. Thus, some thesis and dissertation copies are in typewriter face, while others may be from any type of computer printer.

The quality of this reproduction is dependent upon the quality of the copy submitted. Broken or indistinct print, colored or poor quality illustrations and photographs, print bleedthrough, substandard margins, and improper alignment can adversely affect reproduction.

In the unlikely event that the author did not send UMI a complete manuscript and there are missing pages, these will be noted. Also, if unauthorized copyright material had to be removed, a note will indicate the deletion.

Oversize materials (e.g., maps, drawings, charts) are reproduced by sectioning the original, beginning at the upper left-hand corner and continuing from left to right in equal sections with small overlaps. Each original is also photographed in one exposure and is included in reduced form at the back of the book.

Photographs included in the original manuscript have been reproduced xerographically in this copy. Higher quality 6" x 9" black and white photographic prints are available for any photographs or illustrations appearing in this copy for an additional charge. Contact UMI directly to order.

U·M·I

University Microfilms International
A Bell & Howell Information Company
300 North Zeeb Road, Ann Arbor, MI 48106-1346 USA
313/761-4700 800/521-0600

Order Number 9207130

The mechanics of transcapillary exchange

Tsay, Ruey-Yug, Ph.D.

City University of New York, 1991

U·M·I

300 N. Zeeb Rd.
Ann Arbor, MI 48106

A

THE MECHANICS OF TRANSCAPILLARY EXCHANGE

by

Ruey-Yug Tsay

A dissertation submitted to
the Graduate Faculty in Engineering
in partial fulfillment of the requirements
for the degree of Doctor of Philosophy
The City University of New York.

1991

This manuscript has been read and accepted for the Graduate Faculty in Engineering in satisfaction of the dissertation requirement for the degree of Doctor of Philosophy.

5/30/91
Date

Professor Sheldon Weinbaum
Chair of Examining Committee

5/30/91
Date

Professor Gerard Lowen
Executive Officer

Dr. Fitz-Roy E. Curry
Dr. Andreas Acrivos
Dr. Charles Maldarelli
Dr. Peter Ganatos

Supervisory Committee

The City University of New York

Abstract

THE MECHANICS OF TRANSCAPILLARY EXCHANGE

by

Ruey-Yug Tsay

Adviser: Professor Sheldon Weinbaum

The interendothelial cleft is the principal pathway for water and hydrophilic solute transport across the capillary wall. Existing theories, based largely on one-dimensional models, have had limited success in correlating capillary permeability data and junctional ultrastructure. A new theoretical framework has been developed herein to examine the role of the detailed structure of the intercellular cleft in the regulation of capillary permeability.

The new three-dimensional junction-pore-matrix model has been used to examine the transport behavior of a cleft with a junction strand with discrete pores and fiber matrix components in its wide part. The results indicate that for a cleft with infrequent larger pores, the lateral spreading at the entrances/exits of the junctional pores can be very significant. New hydrodynamic theories have been developed for the effect of fibers in the wide part of the cleft. A rigorous solution for a channel flow through a square array of fibers with aspect ratio B>5 provides convincing evidence for the accuracy of a Brinkman approximation for long slender fibers.

The new theoretical models developed herein indicate that neither a junction-pore model with small pores of the required size for them to be the primary molecular sieve nor a simple fiber matrix filling the entire cleft can explain all the measured data for capillary permeability. Feasibility studies show that a cleft with

larger junctional breaks, typically 22x44 nm in cross-section, and with a fiber layer at the cleft entrance is the most likely cleft structure to reconcile the structural and permeability data. The present model predicts that a cleft with 22x44 nm pores, with pore spacing of 480 nm, when combined with a fiber matrix with open spacing Δ=7 nm can fit the measured values for the hydraulic conductivities with and without a fiber layer. This structure can also fit the measured values of diffusive permeability for small ions and large solutes of size close to albumin. However, this model still does not fit the diffusive permeability data for intermediate size solutes of 1-2 nm radius. Experiments based on the present study are suggested for the future work.

ACKNOWLEDGEMENTS

The author would like to express her profoundest gratitude to her mentor, Professor Sheldon Weinbaum, who in addition to being a source of continued advice and support throughout the course of this work, provided her with a stimulating environment which led her to her enthusiasm for research and gave her the confidence to pursue new ideas.

Special thanks are due to provost Robert Pfeffer, whose generous support and guidance made it possible for the author to enter into this challenging field of research. Thanks are also due to Dr. Fitz-Roy E. Curry and Professor Peter Ganatos for their thought provoking discussions.

Finally, the author wishes to dedicate this work to her parents and husband Shi-Yow for their continuous encouragement and support.

TABLE OF CONTENTS

LIST OF TABLES

LIST OF FIGURES

CHAPTER I

INTRODUCTION

Physiologic data indicates that the interendothelial cleft is the principal pathway for water and hydrophilic solute transport across the capillary wall (Pappenheimer 1953, Landis and Pappenheimer 1963, Wissig 1979). Direct and indirect morphological evidence shows that there are junctional protein strands and fiber matrix components in the junctional cleft which could serve as the major molecular sieve for solute transport. Both existing pore-slit and fiber-matrix models have had limited success in correlating junctional ultrastructure and capillary permeability data. The objective of the present research is to develop a new conceptual theoretical framework based on ultrastructure and microperfusion studies to examine the role of the intercellular cleft and its structural components in the regulation of capillary permeability.

The microvascular bed is the primary location where water and solutes associated with nutrition and metabolism are exchanged between blood and tissue. Capillaries are the smallest ramifications of the microvessels. Capillary walls consist of endothelium, basal lamina and pericytes. The detailed structure of each capillary segment varies according to the nature and activity of the surrounding tissue. In general, the main types of capillaries encountered are: continuous, fenestrated, and discontinuous capillaries (Simionescu and Simionescu 1984). The present study will concentrate on continuous capillaries which are the most common type of capillary encountered in

somatic tissue. The endothelium of continuous capillaries are devoid of fenestrations (large open pores). The endothelial interface between plasma and interstitial fluid is the major barrier for water, solutes and macromolecular transport. Vascular endothelium is a complex structure which offers several pathways for exchange. These pathways include: cellular, fenestrae, vesicular, fused vesicular, and intercellular junction pathways (Renkin 1977, Curry 1984). Although, the "large pores" by which hydrophilic macromolecules cross the microvascular endothelium remain controversial, there is a large body of evidence showing that most of the transcapillary exchange of water and small hydrophilic solutes occurs via the water-filled clefts between endothelial cells in continuous capillaries (Starling 1909, Pappenheimer 1951, Karnovsky 1967,68, Renkin & Curry 1978). The likelihood that this intercellular space forms the "small pore" has been widely accepted (Wissig 1979, Bundgaard 1980, Crone 1981), and it is believed that only a fraction of the clefts need to be permeable to account for the measured capillary permeability (Lassen & Trap-Jensen 1970). Because diffusion through the small pores of molecules with a molecular weight larger than 40,000 daltons is severely restricted, the transport of macromolecules relies mainly on the large pore pathway (Karnovsky 1967, Wissig 1979). The present study will focus on searching for the structural component of the small pore which regulates the passive transcapillary exchanges of water and small hydrophilic solutes.

Conventional electron microscopic studies show that the cleft width (gap height) along the entire intercellular channel is almost uniform except for one or more sites of closer membrane apposition or fusion (Casley-Smith *et al.* 1975, Perry 1980, Bundgaard & Frokjner-Jensen 1982). In freeze-fracture studies these sites appear as continuous (Simionescu *et al.* 1975) or discontinuous (Wissig 1979) alignments of particles which are called junctional strands.

Cytochemical studies also indicate that all or part of the cleft may be filled with a fibrous matrix. These two structures form the principle barriers for water and solute transport in the capillary wall.

Numerous investigators have attempted to resolve the detailed organization of the junctions using freeze-fracture studies or thin section electron microscopic techniques with or without tracers. Karnovsky (1967,68) showed that the tight junctions of heart or skeletal muscle capillaries were permeable to horse-radish peroxidase molecules (HRP, molecular diameter $\simeq$ 5 nm). Wissig (1979) proposed that the passage of microperoxidase molecules (MP, molecular diameter $\simeq$ 2 nm) in the clefts of mouse skeletal muscle capillaries could occur via the tortuous pathways formed by the discontinuities in the junctional protein strands or directly through the protein strands. Ward *et al.* (1988) examined the structure of rat cardiac capillaries and found that Cytocrome C (diameter 3 nm) and HRP both crossed the endothelium to the subendothelial space while Haemoglobin (6.4nm) and catalase (10.4nm) did not penetrate the endothelium. Firth *et al.* (1983) in his random thin section and freeze-fracture studies for pig placental capillaries indicated that there were one to five tight junction strands. He proposed that the tight junctions were formed by equally spaced junctional bars with 5.5 x 11 nm rectangular pores between them and the diameter of these junctional bars was approximately the same as the 11 nm space between them. Sibley *et al.* (1982, 83) showed that the hemepeptide tracers up to a molecular diameter of about 6 nm can penetrate the lateral intercellular space of a pig placental capillary. These studies confirmed that the junctional cleft is the major route for small hydrophilic solute transport. However, they have provided limited information on the three-dimensional organization of the junctions and the structural

basis of the filter within the interendothelial clefts remains controversial.

Bundgaard, in his pioneering paper in (1984); was the first to attempt to examine the three-dimensional junction ultrastructure. In this study, rat heart capillaries were reconstructed using conventional 40 nm thin and 12.5 nm ultrathin serial section electron microscopy. Large pores of 10-20 nm x 20-80 nm and small pores of 4-5 nm x 5-30 nm were observed. Bundgaard suggested that these pores were the structural correlate of the tortuous pathway proposed by Wissig (1979). Bundgaard sketched these pores as short discontinuities in the junction protein strands. In contrast to Bundgaard's work, Ward *et al.* (1988) examined the three dimensional features of the junctions of rat cardiac capillaries by using a goniometric tilting technique. After considering the tilting effects, they claimed that more than 70 percent of the random thin sections of junctional clefts were actually open and concluded that the pathways for small and intermediate solutes were not formed by interruption in continuous lines of membrane fusion but by continuous junctional regions with an approximate opening of 5 nm width. Further studies are needed to resolve this discrepancy.

The structure of a fiber matrix in the intercellular pathway is less clearly identified. Using ruthenium red staining, Luft (1966) showed that there is a 'fluffy layer' on the luminal surface of endothelial cells. Turner *et al.* (1983) indicated that cationized ferritin was bound in a thin layer of 20-30 nm thickness near the endothelial cell surface and native ferritin was excluded from the endothelial coat. Recent studies indicate that in general there are anionic sites on the endothelial surface which correspond to sialated glycoproteins embedded in the cell plasma membrane in association with proteoglycan and plasma proteins (Gingell 1976; Simionescu *et al.* 1981, 1985; Schneeberger and Hamelin 1984). This endothelial cell

glycocalyx may correspond to the fiber matrix in the fiber-matrix hypothesis (Curry and Michel 1980). Adamson (1990) studied the fiber matrix hypothesis by comparing normal capillary hydraulic conductivity L_p with L_p measured after partial degradation of the endothelial cell glycocalyx. He observed a 2-3 fold increase in capillary L_p in frog mesentery capillary. Other investigations have suggested the presence of larger cross-bridging fiber structures in the wide part of the cleft. Firth *et al.* (1983), in his work on pig placental capillaries, suggested that there were linking molecules with radius 5 to 10 nm with a spacing as large as 19 nm in the wide portion of the clefts. Silberberg (1987) also proposed that the linking molecules might be necessary to provide the nearly uniform cleft width in the wide portion of the clefts.

Permeability studies show that the capillary wall behaves as a passive membrane for water and small hydrophilic solute transport (Crone & Levitt 1984, Michel 1984). This allows the interpretation of permeability properties in terms of capillary wall structure. It has been nearly four decades since Pappenheimer first proposed the pore theory. However, the effort to correlate capillary permeability and morphological data has not been very successful. The major difficulties encountered include: (i) experimental limitations, (ii) lack of definitive studies on three-dimensional junction structure, and (iii) the heterogeneity of the microvessel bed.

First, the limitations in experiments may due to the specimen shrinkage and distortion in sample preparation and the incomplete electron opacity of "electron-opaque" membrane structures in electron microscopy studies.

Secondly, crucial information on the three dimensional organization of junctional structure, such as the frequency of pores in the junctional strands is not available. For example, the tissues for which complete single vessel perfusion measurements of the

transport coefficients exist, the frog mesentery and muscle capillaries, have not been systematically examined for their ultrastructure. Due to the experimental limitations mentioned above and lateral diffusion effects in tracer experiments, the conventional random thin section EM studies can not offer a complete picture of the three-dimensional junctional structure. Therefore, experiments combining freeze fracture and serial section electron microscopic studies are needed.

Finally, the heterogeneity of the microvessel bed causes problems when the measurements of the transport coefficients have not been directly related to the cleft dimensions of the same tissue specimens. Before the 1970s, the permeability properties of mammalian capillaries were measured by whole organ methods which greatly compromised the correlation between the individual capillary structure and its permeability properties. The development of the single capillary microocclusion technique (Michel *et al.* 1974; Curry *et al.* 1983) makes it possible to investigate the permeability properties for a single microvessel. One of the major advantages of using this technique is that we can investigate the ultrastructure of the walls of a single capillary in which the hydraulic conductivity and permeability of the vessel walls have been measured. No experiment has been performed to directly correlate structural dimensions and transport properties in the same tissue specimen until the recent studies by Clough & Michel (1988). Using fiber matrix theory for an infinite medium, they showed that the hydraulic conductivity could be accommodated if half of the intercellular cleft length is fully open. Lanthanum staining of clefts from luminal to abluminal surface was seen in 58 out of 108 random TEM sections. Without considering the effects of lateral diffusion, these observations were interpreted as indicating that approximately 50 % of the junctional strand length is open in frog mesentery.

According to the Kedem-Katchalsky equations, a passive membrane can be quantitatively characterized by three parameters, a filtration coefficient Lp, a permeability coefficient ω, and an osmotic reflection coefficient σ. These three principal parameters, which are measured experimentally, are related to cleft structure using theoretical models. At present there are two major theories, pore-slit theory and fiber matrix theory, which attempt to correlate cleft structure and the large amount of experimental data for these coefficients measured by whole organ or single capillary techniques.

The principal assumption in the derivation of the pore equations is that the hydrodynamic relations describing flow and viscous drag forces in macroscopic flow systems are applicable in channels of molecular dimensions (O(10 nm)) (Curry 1984). In pore-slit theory the hydrophilic pathways in transcapillary transport are assumed to be formed by the discontinuities in the junctional strand arrays. The classical pore theory first proposed by Pappenheimer *et al.* (1951,53) used uniform cylindrical pores or uniform slits to describe these pathways. Since a uniform width slit could not account for both hydraulic conductivity and reflection coefficient data, this simple model was then modified by including a narrow region which is formed by a junction region inside the channel. This junction region serves as the molecular filter. The width of the junctional region has been chosen to fit the large body of osmotic reflection coefficient data for hydrophilic solutes with radii smaller than 3.5 nm. A simple one-dimensional model is used to describe the permeability of water flow and solute transport. The basic assumption of this one-dimensional model is that the lateral spreading at the entrance (exit) of junctional gaps is negligible and that there is no interaction between water and solute passing through each pathway. Permeability is thus proportional to the length of open junction. This one-dimensional model, which has been used in the analysis of all experimental

measurements of permeability data to date, will be strongly challenged by the new three-dimensional models proposed herein.

The major discrepancies between the predictions of one-dimensional pore-slit model and the experimental measurements are summarized below.

(1) This model underestimates the diffusive resistance to large solutes when the length of open junction is set to account for the diffusive permeability to small solutes. The model predicts only 20 % of the diffusive resistance for molecules with radii between 1.5 and 3.5 nm (Curry 1984). In other words, no current pore-slit model describes a sufficient change in resistance with increasing solute size to enable the constricted region to account for most of the diffusive resistance to large solutes. If this condition is not met, the constriction cannot be the site of the molecular filter.

(2) This model overestimates the hydraulic resistance of water flow when the cleft dimensions are set to account for the diffusive permeability to small solutes. The equivalent slit width that describes the hydraulic conductivity of the capillary wall is larger than the equivalent slit width that describes the selectivity of the capillary wall. This is usually explained by assuming that the narrow region is the major molecular filter and the equivalent slit width is chosen to account for the reflection coefficient data.

(3) The assumption that the constricted region forms the molecular filter makes it difficult to explain the observation that the removal of plasma proteins from the perfusate decreases the effective osmotic reflection coefficient (Curry 1985, Curry *et al.* 1987).

(4) Experiments show that the reflection coefficient for frog mesentery capillary is the same as that for frog skeletal muscle capillary, but the hydraulic conductivity and small solute permeability for frog mesentery capillary are 7 to 10 times larger

than those for frog muscle capillaries. Because the constriction contributes much of the hydraulic resistance, but little of the diffusive resistance to small solutes, one would not expect hydraulic conductivity and permeability to change in a nearly proportional manner. This is usually interpreted as indicating variation in the length of open junctional strand. This length is calculated to vary from less than 10 % in skeletal muscle to as much as 90 % in mesenteric capillaries. This prediction is hard to reconcile with the structural organization of the tight junction regions observed in random thin sectioning (Clough & Michel 1988) and ultrathin serial sectioning studies (Bundgaard *et al.* 1982, Bundgaard 1984).

Because of the limited success of the pore-slit model, Michel (1978, 79) reintroduced the idea that the principle molecular sieving sites of the capillary wall may lie within a network of proteoglycan molecules in the intercellular junctional pathways. The fiber matrix model (figure 2(b)) proposed by Curry & Michel (1980) provided the first attempt to analyze this idea quantitatively. This model assumed that the major resistance to transcapillary exchange comes from the fiber matrix, so the filtration, permeation, and sieving properties depend on the total available channel area only and will not be affected by the specific geometry of the channels.

In the fiber matrix theory, the hydrodynamic resistance is described by the Carmen-Kozeny equation (Sullivan *et al.* 1942), the diffusive resistance is described by a stochastic model for diffusion within a fibrous network (Ogston *et al.* 1973), and the sieving properties are approximated by applying the equation proposed by Anderson *et al.* (1974, 81), which implies a pseudo-Poiseuillean velocity profile between fibers. Because of its flexibility in choosing the fiber radius and density, this model is able to quantitatively account for many of the inconsistencies noted in the one-dimensional pore-slit model.

The principal drawbacks of the fiber matrix model are: (1) the model assumes that the presence of the junction strands only affects the total effective area for exchange. This assumption is based on a one-dimensional model which neglects the lateral spreading at the entrance/exit of junctional gaps and the interaction between water and solute passing through each pathway; (2) the effect of the adjacent plasma membranes (slit walls) is neglected and the membrane coefficients (Lp, ω, σ) are derived as if the fiber matrix is in an infinite domain. This is true only when the spacing between fibers is small enough for the fibers themselves to offer the major transport resistance. The treatment of wall and fiber boundary conditions in a rigorous theory for water filtration in this dissertation has lead to the conclusion that the hydraulic conductivity predicted by the Carmem-Kozeny equation is substantially underestimated when the gap spacing between fibers is larger than the half width of the junctional cleft; (3) although the ruthenium red staining shows that a glycocalyx exists on the luminal surface of endothelium cells, the limitation on the resolution of EM pictures still prevents further direct identification of the existence of fiber matrix in the interendothelial clefts. (4) experimental results show that junctional clefts of rat heart capillaries are permeable to HRP molecules (molecule diameter $\simeq$ 5-6 nm) but impermeable to hemoglobin molecules (molecule diameter $\simeq$ 6.4 nm) (Ward *et al.*, 1988). Although charge and molecular configuration effects may affect the exchange, the original random fiber matrix model would have difficulty in explaining such a sharp cut off in sieving properties. Curry (1985) proposed that the presence of albumin might somewhat order the fiber array and increase the molecular selectivity of fiber matrix. To test this idea, hydrodynamic and diffusive theories for flow and solute diffusion through an ordered fiber array need to be established.

In the present research a more realistic three-dimensional model which attempts to more rigorously satisfy the three dimensional boundary conditions imposed by the walls of cleft, the junction strands and fiber components is proposed. In chapter 2, this three dimensional model is set up and theories which account for the lateral spreading at the entrances/exits of junctional pores and interactions between pores are developed for water filtration. Also a preliminary study for the effect of fiber matrix in the junction has been conducted. In chapter 3, the rigorous solutions for water filtration and the theories for estimating the diffusive permeability of particles through a confined fibrous bed are developed. The rigorous solutions have provided a rational justification for using a simple Brinkman approximation in estimating the hydraulic resistance across a confined fibrous bed. In chapter 4, The combined junction-pore-matrix model with a fiber matrix filling all or part of the cleft is presented. Based on the EM studies, the transport properties of junctions with three different possible junctional pores, i.e.; cylindrical pores of 4.5-5.5 nm radius, rectangular slits of 8 nm width, and large tortuous pores open to the full channel height, are closely examined. Finally, The last chapter summarizes the major results and gives recommendations for future research.

CHAPTER II

A NEW MODEL FOR CAPILLARY FILTRATION BASED ON RECENT ELECTRON MICROSCOPIC STUDIES OF ENDOTHELIAL JUNCTIONS

2.1 Introduction

The classical theories of capillary permeability have had only limited success in explaining the large body of existing data on hydraulic conductivity, solute permeability and selectivity (osmotic reflection coefficient) (Crone and Levitt, 1984; Curry, 1984; Michel, 1984). This data contains three fundamental features that are difficult to reconcile using either the classical cylindrical pore model first proposed by Pappenheimer *et al.* (1951) or its various extensions including the constricted channel as summarized by Curry (1984). (1) The theoretical predictions of these models for the hydraulic conductivity show that the width of the hydrophilic channel required to accommodate the measured water flux is significantly larger than the channel width required to predict the measured permeability coefficients for the diverse assortment of solute molecules (0.5 to 3.5 nm radii) that have been used to analyze the transcapillary pathways for small and intermediate size solutes, e.g. the data for frog mesentery show that a slit model with 8 nm constriction, which satisfactorily describes the hydraulic conductivity, predicts a solute diffusive resistance which is a factor of five larger than the measured permeability coefficients for solutes with radii between 1.5 and 3.5 nm (Curry 1986). (2) the data for the osmotic reflection coefficients which describe the size of the

molecular sieve in these models, correspond to either a slit of 6 to 8 nm width or a circular cylindrical pore of 5 to 6 nm radius (Curry 1986). These predictions are also not compatible with the permeability coefficients just cited. (3) Measurements of small ion permeability and hydraulic conductivity in frog and mammalian capillaries summarized in Crone and Levitt (1984) and Crone (1984) suggest a cleft that is open from 5-10 percent of its total length in heart, lung and skeletal muscle and as much as eighty percent open in frog mesentery using existing slit models (Lassen and Trap-Jensen, 1970; Perl, 1971; Casley-Smith *et al.*, 1975; Perry, 1980; Crone and Levitt, 1984). This prediction is hard to reconcile with the structural organization of tight junctions observed in freeze-fracture (Simionescu *et al.*, 1975; Firth *et al.*, 1983) and ultrathin serial sectioning studies (Bundgaard, 1982, 84) in which the tight junctions are almost continuous except for infrequent small breaks and more numerous shorter gaps the length of one or two proteins. A lucid summary of these and related contradictions are presented in an excellent recent review article by Curry (1986).

The inability of classical pore and slit theory to reconcile these various inconsistencies has provided the motivation for the development of an alternative fiber matrix theory for capillary permeability (Curry and Michel, 1980). The predictions of this theory and its extensions are summarized in Curry (1984) and Michel (1985). The fiber matrix model, because of its greater flexibility, is able to quantitatively account for the major discrepancies in the predicted results for the various membrane coefficients. This theory rests on a fundamental hypothesis that the wide portion of the intercellular cleft is filled with a glycocalyx of proteoglycans. Although a surface glycocalyx at the luminal front of endothelial cells was first reported more than twenty years ago (Luft, 1966), no direct evidence to support the existence of such a network in the intercellular cleft

has emerged from the numerous electron microscopic studies of junctional complexes that have been conducted in the intervening years. In this paper a new model for capillary permeability will be proposed which we believe is more consistent with detailed studies of junction ultrastructure that have been obtained from freeze fracture electron microscopic studies and serial section reconstruction techniques (Simionescu *et al.*, 1975; Bundgaard, 1984). The model differs conceptually from previous theoretical models in that the pores are short discrete holes formed by individual missing proteins in the interwoven array of protein strands that form the junctional complexes and that the multidimensional interaction between the fluxes entering and leaving these discrete pores are considered for the first time. The present paper will concentrate on the hydraulic conductivity and membrane selectivity of the new model. The results provide important new insights into the possible structure of junction strands and are able to reconcile some of the important contradictions mentioned at the beginning of the introduction. The effect of fibers or bridging molecules in the wide portion of the cleft will also be examined using a more rigorous hydrodynamic approach based on a modified Hele-Shaw theory. This theory indicates that the Carmen-Kozeny equation grossly underpredicts the resistance of cross-linking fibers in a narrow channel because it neglects the influence of the viscous layers that on along the walls of the channel and the interaction of these layers with the cross-bridging fibers.

(a) Previous models

Although the early hydrophilic pore theory was based on a cylindrical pore (Curry, 1984; Pappenheimer *et al.*, 1951), electromicroscopic studies strongly suggested that the intercellular cleft was the primary pathway via which water and small and intermediate size solutes (less than 3.5 nm radius) cross vascular endothelium. The occasional openings of 4-6 nm gap width observed in

transmission electron micrographs of the cross-section of an interendothelial cleft suggested that these openings were the ultrastructure correlated small pore and that molecules as large as HRP (molecular diameter 5 nm) (Karnovsky, 1967, 68) could cross the junctional array of protein strands via a tortuous path through these openings (Wissig 1979). Several investigators proposed that the pores were long slender rectangular slits of 6 nm gap width and several hundred nm length interspersed between tight junction regions and developed simple one-dimensional models to predict length of junction that needed to be open to obtain the measured values for the filtration coefficient L_p and permeability coefficient ω in various tissues. In the most detailed of these one-dimensional models (Perry 1980) the variation in gap width along the entire depth of the cleft was constructed using data for lung and skeletal muscle capillaries. The model by Gosselin and Stibitz (1977), which was based on the morphometry suggested in Casley-Smith et al. (1975), also examined the lateral spreading from these isolated slits in the wide portion of the cleft using a numerical generated random walk model to simulate the three-dimensional diffusion effects. As shown in (Crone and Levitt, 1984) either large gap widths are required or substantial lengths of the channel need to be open in the constricted regions if the water and solute fluxes predicted by these one-dimension models are to match the experimental data.

The foregoing one-dimensional models in which long rectangular slits of varying width are placed in series along the depth dimension of the cleft were based on random sampling electron micrographs with typical section thicknesses of 40-60 nm which do not show the three-dimensional organization of the junction or the length of the gaps. These models do not correspond well to the latest detailed serial reconstructions of the junctional regions of rat heart muscle capillaries observed by Bundgaard (1984) or the enface topography of

the junctional strands observed in freeze cleavage studies of the junctional complex (Simionescu *et al.*, 1975; Firth *et al.*, 1983). Using a section thicknesses of only 10 to 15 nm Bundgaard was able to show that there are frequent small gaps in the junctional strands of between 10 to 20 nm length, that are totally missed by conventional sectioning techniques, in addition to the statistically infrequent tortuous pathways formed by larger breaks [40 nm or larger] as suggested by Wissig (1979). In our model the small gaps correspond to only one or two missing junctional proteins. This view is consonant with the freeze cleavage studies of junctions just cited in which junctional strands form an interlaced lattice in which occasional missing proteins are observed as schematically shown in Figure 2.1. Since the small pores in Figure 2.1 occupy such a small fraction of the length of the junction and the junctional arrays often consist of two or more strands in series, it is hard to conceive that sufficient water and solute could pass through such a barrier when models for the much longer slits mentioned above predict that these slits are only sufficient when significant lengths of cleft are open.

The pore interaction model proposed herein will offer a very plausible explanation to this paradox. This explanation was first suggested by the results of another study in which the authors constructed a model to simulate the macromolecular diffusion across an arterial wall (Weinbaum *et al.*, 1985). It was observed in the latter investigation that large increases in permeability were possible if only a few endothelial cells in a thousand had fully open junctions provided the spacing of such cells was comparable to or smaller than the thickness of the artery wall. Furthermore, if the junctions around all cells were open to a width of 20 nm the macromolecular permeability would be nearly the same as if the entire endothelium were denuded although the cross-sectional area of the channels was only 0.3 percent of the surface. In the context of the present

problem numerous small holes in the junctional strands caused by isolated missing proteins could result in large increases in hydraulic conductivity and solute permeability provided the average spacing between these pores is small compared to the depth of the cleft. We shall show that for these conditions the simple formulas relating the primary hydraulic resistance to the fourth power of the radius of the smallest pores does not apply, since the interaction between the fluxes entering and leaving the pores in the wide portion of the cleft is the controlling influence on the pressure distribution throughout the channel. Similarly, we shall demonstrate that the generally accepted concept that the flux is proportional to the open junction length is not valid since the interaction between the pores due to their spacing changes the resistance of each pore pathway.

2.2 Model Development

2.2.1 Simplified Mathematical Model

The three-dimensional structure suggested by the experimental studies of Wissig (1979), Firth *et al.* (1983) and Bundgaard (1984) and shown in Figure 2.1, has been converted into a simplified mathematical model which is shown schematically in Figures 2.2a,b. Figure 2.2a is a three-dimensional sketch of the model showing the direction of the top and side views which are shown in detail with dimensions in Figure 2.2b. The linking molecules (fibers) shown in Figure 2.2b have been omitted from Figure 2.2a to simplify the latter sketch. The tight junctional strands have been converted into a barrier that is impermeable except for the small holes of radius r_p that are periodically distributed along the length of the protein strand. While freeze cleavage studies showing the junctional proteins enface indicate that these intramembranous particles are approximately 10 nm diameter, a better estimate for the present purposes of the size of these pores can be deduced from the theoretical predictions of the

osmotic reflection coefficient shown in Figure 2.3 taken from Curry (1986). The data for capillaries in the rat hind quarter (Rippe and Haraldsson, 1983), rabbit heart (Vargas and Blackshear, 1980) and frog mesentery (Curry *et al.*, 1976; Michel, 1980) show that the available data for all solutes from 0.5 to 3.5 nm radius can be fit by a selective sieve which is between 5 and 6 nm radius. Equally important is the observation in (Curry *et al.*, 1976; Curry and Frokjaer-Jensen, 1984) that the solute reflection coefficient in frog muscle and mesentery capillaries is nearly identical for the same size molecules although the hydraulic conductivity and the small ion permeability of the latter is approximately seven times the former. This strongly suggests that selective structure is the same and that the large differences in L_p and ω are only related to the number of such opening. The location of this sieving structure could lie at the entrance to the junctional pores or in the wide portion of the cleft as proposed in the fiber matrix theory (Curry and Michel, 1980; Michel, 1985). Both these possibilities will be discussed later in the context of the numerical results.

The solute reflection coefficient curve used to estimate r_p in Figure 2.3 is only an initial guess since σ also depends on the solute concentration gradient in the wide portion of the cleft. The distribution of the diffusive resistance depends on r_p, the pore spacing and the dimensions of the wide portion of the channel. A simple one-dimensional series resistance model will be introduced later in the paper, once the relation between L_p, r_p and the pore spacing is determined, to estimate the effect of the wide portion of the cleft on σ. It will be shown that the influence of the wide portion will be about seven percent for frog mesentery and about one percent for frog muscle capillaries and thus the above estimate for r_p will not be significantly altered.

The length L_2 of the cylindrical pores shown in Figure 2.2a,b will be the same as their diameter if one considers a single intramembranous particle strand with roughly spherical missing proteins. The strands, however, appear in staggered line arrays that can be viewed as resistances in series as sketched in Figure 2.1. The small enclosed regions between strands will have a very small resistance compared to the pores in the strands if these regions can be treated as nearly constant pressure enclosures. For the pressure drop in the wide regions between strands to be neglected, their spacing must be small compared to the total depth of the cleft. Electron microscopic studies have indicated that when multiple strands are present they occupy the order of ten percent of the cleft depth (Perry, 1980) and therefore this a reasonable approximation. If each line in the array has roughly the same pore distribution and size then the cleft of the multiple strands can be treated by making L_2 a multiple of $2r_p$ if the small pressure drop between strands is neglected. The resistance of a single equivalent strand for a multiple strand array can therefore be approximated by a pore of depth $L_2=2nr_p$, where n is the number of strands. L_1 and L_3 are the depths of the cleft on each side of this equivalent strand at the lumen and tissue fronts of the endothelial cell respectively. D is the half distance between the centers of two adjacent pores in the periodic array and B is the half cleft width of the wide portion of the cleft which is assumed uniform for mathematical convenience. The fact that the cleft half width widens over several nm from the region of close apposition at the junctional strand to the full half width B of 8.5 nm is of little consequence since near the tight portion this is effectively dead space and the interaction distances for the mixing of the pore entrance and exit fluxes, L_1 and L_3, are large compared to this region of non-uniformity. The actual diameter, length and frequency of the holes in the protein strands are very difficult to

determine from electron microscopy and it is one of the most attractive features of the simplified model formulation that the role of each of these parameters, as well as the position of the equivalent junctional strand in the cleft, can be relatively easily explored within the framework of the closed form analytical solutions presented herein.

Another simplification that will be introduced in the model is the approximation for the shape of the pore at the entrance and exit boundary of the junctional strand. The pore itself will be treated as a short circular cylinder since this shape as noted above provides a good estimate of the osmotic reflection coefficient. This shape, however, is inconvenient for treating the interacting parallel channel flows in the wide portion of the cleft on each side of the equivalent junctional strands, which will be analyzed using two-dimensional Hele-Shaw theory. The latter requires a rectangular opening which is the full height 2B of the channel flow. Thus in the model we shall use rectangular entrance and exit ports whose area 4Bd (d is the half gap length) and flux just match the area πr_p^2 and flux of the circular pores. This simplification will have little effect on the results since it is the lateral spread of the entrance and exit jets in the plane of the channel and the interaction between the jets that determines the overall hydraulic resistance rather than the details of the entrance profile.

Although the basic formulation of the cleft model, which we shall now describe, will not include the effect of cross-linking proteins or fine fibers spanning the width of the cleft in the wide portion, it is not difficult to include these effects in an approximate manner at the end of the analysis. The existence of cross-linking proteins has been suggested by Silberberg (1987). Firth *et al.* (1983) have observed patterns after tannic acid staining that are vaguely suggestive of such structures. Silberberg (1987) has proposed that structures of

this nature might be necessary to provide the nearly uniform spacing that is characteristic of the wide portion of the cleft. The fine 0.3 to 0.6 nm fibers that are part of the fiber matrix theory (Curry and Michel, 1980) can be treated in a similar manner to these cross-linking proteins and the Hele-Shaw analysis modified at the end to include the additional resistance that would result from having a small volume fraction of cross-bridging molecules of either nature. This theoretical approach, which was recently proposed by Hsiung (1984), is an interesting extension of the septal post model introduced be Lee and Fung (Lee, 1969; Lee and Fung, 1969) to describe the alveolar sheet flow in the lung.

2.2.2 Governing Equations and Boundary Conditions

In regions 1 and 3 the (x,y,z) coordinate system is chosen such that x,y plane is chosen parallel to the walls of the two adjacent endothelial cells and the origin of the z coordinate taken as the midplane of the cleft, see Figure 2.2a. Since the width of the cleft 2B is small compared to both the average distance 2D between the pores and the depths L_1 and L_3 the velocity component in the z direction can be neglected. Similarly, velocity gradients in the x,y directions in the viscous terms in the momentum equation will be small compared to those in the z direction. This approximation for a narrow viscous channel flow in which the flow moves as parallel sheets in the x,y plane and nonlinear inertial terms can be neglected is referred to as Hele-Shaw flow. The continuity and momentum equations for this flow are:

$$\frac{\partial u}{\partial x} + \frac{\partial v}{\partial y} = 0 \qquad (2.1)$$

$$\nabla p = \mu \frac{\partial^2 \vec{u}}{\partial z^2}, \qquad \vec{u} = ui + vj \qquad (2.2)$$

Here u,v are the x,y components of the fluid velocity and w = 0. The boundary conditions at the boundary plasmalemma membranes of the cleft are no slip

$$u = v = 0 \qquad z = \pm B \tag{2.3}$$

The solution of Equation (2.2) which satisfies equation (2.3) is

$$\vec{u} = \vec{u}_o\left(1 - \frac{z^2}{B^2}\right) \tag{2.4}$$

where

$$\vec{u}_o = - \frac{B^2}{2\mu} \nabla P \tag{2.5}$$

is the velocity at the centerplane z=0 of the cleft.

From Equation (2.5) one can show that the x,y components of the centerline velocity satisfy

$$\frac{\partial u_o}{\partial y} - \frac{\partial v_o}{\partial x} = 0 \tag{2.6}$$

Combining Equations (2.4) and (2.5) and substituting in equation (2.1), one obtains

$$\frac{\partial^2 P}{\partial x^2} + \frac{\partial^2 P}{\partial y^2} = 0 \tag{2.7}$$

Equations (2.6) and (2.7) illustrate the two essential features of Hele-Shaw flow. Equation (2.6) shows that the z component of the vorticity vanishes and the motion in the x,y plane is irrotational. The velocity components in this plane thus satisfy a potential flow equation and it is therefore not possible to satisfy no slip boundary conditions in the x, y plane when equation (2.2) is used as the approximate momentum equation. Equation (2.7) shows that the pressure

field also satisfies Laplaces equation in the x, y plane. The viscous resistance in Hele-Shaw flow originates from the sharing stress at the boundary plasmalemma membranes at z = ±B rather than the vertical boundaries or obstacles in the x, y plane, where as just noted no slip boundary conditions cannot be satisfied. Thus, to determine the additional resistance that results from cross-bridging molecules or fibers in the wide portion of the gap, equation (2.2) must be generalized to include the shear stress terms involving the second partial derivatives of u, v with respect to x, y. The inclusion of these higher derivative terms will make it possible to satisfy viscous no-slip boundary conditions on any vertical boundaries and find the additional resistance that arises from any cross-bridging molecules in the flow. This generalization of the theory will be presented after the solution to the basic Hele-Shaw problem for the interaction between flows passing through the junction pores.

As shown in Figure 2.2 the interaction between the pores created by the occasional missing proteins (or groups of missing proteins if wider breaks in the junctional proteins strands are present) can be represented by a periodic boundary value problem which satisfies the following boundary conditions on the velocity field in region 3. Equivalent boundary conditions can be written for region 1.

$$u_o = -\frac{B^2}{2\mu}\frac{\partial P}{\partial x} = u_o(L_2') \qquad x = -L_1 + L_1 - L_2' \qquad -d<y<d \tag{2.8}$$

$$u_o = 0 \qquad x = L_2', \qquad d<|y|<D \tag{2.9}$$

$$v_o = 0 \qquad L_2' \leq x \leq L, \qquad y = 0 \tag{2.10}$$

$$v_o = 0 \qquad L_2' \leq x \leq L, \qquad y = D \tag{2.11}$$

Equations (2.8) and (2.9) describe the impenetrability of the junctional strand except for the region -d<y<d of the missing protein or proteins, whereas equations (2.10) and (2.11) are symmetry or periodicity conditions. For the reasons already discussed, one can not satisfy no slip boundary conditions on the v component of the velocity along either surface of the junctional strand. This approximation will have only a very minor effect on the results, since the numerical solutions indicate that the velocities induced along the wall of the junctional strand by the fluid jets through the pores are very small even when there is slip along this boundary. In addition to boundary conditions (2.8) through (2.11) we require that the total pressures on the lumen and tissue sides of the cleft P_L and P_A be constants determined by local difference in hydrostatic pressure across the endothelial layer.

2.2.3 Solution Procedure

The solution to equation (2.7) subject to boundary conditions (2.8) through (2.11) written for region 3 is

$$P(x,y) = P_A + a_o(x-L) + \sum_{n=1}^{\infty} B_n \cos(\lambda_n y) \times [-\tanh(\lambda_n L_3)\cosh(\lambda_n(x-L_2')) + \sinh(\lambda_n(x-L_2'))] \qquad (2.12)$$

where

$$a_o = 2\mu u_o(L_2')d/(B^2D)$$
$$B_n = -4\mu u_o(L_2')\sin(\lambda_n d)/(B^2\lambda_n^2 D) \qquad (2.13)$$
$$\lambda_n = n\pi/D \qquad n=1,2,3,....$$

The average pressure $\bar{P}_2$ at the exit of the pore at $x = L_2'$ is

$$\bar{P}_2 = \int_{-d}^{d} P(L_2',y)\, dy/2d \qquad (2.14)$$

The pressure across region 3 is

$$\Delta P = \bar{P}_2 - P_A = -a_o L_3 - \sum_{n=1}^{\infty} B_n \sin(\lambda_n d)\tanh(\lambda_n L_3)/\lambda_n \qquad (2.15)$$

For region 1, the solution procedure is similar to region 3. The pressure drop across this region is

$$\Delta P = P_L - \bar{P}_1 = -a_o L_1 - \sum_{n=1}^{\infty} B_n \sin(\lambda_n d)\tanh(\lambda_n L_1)/\lambda_n \qquad (2.16)$$

where a_o, B_n and λ_n are defined by equation (2.13) and $\bar{P}_1$ is the average pressure at the pore entrance defined in the same manner as equation 2.14).

In region 2 we neglect entrance and exit effects which have been shown by Dagan *et al.* (1982) to be small and assume for convenience a simple Poisseuille relation between flow rate and pressure drop,

$$\bar{P}_1 - \bar{P}_2 = \frac{8\mu L_2 Q}{\pi r_p^4} \qquad (2.17)$$

The volumetric flow rate Q in equation (2.17) needs to matched to the flow leaving region 1 and entering region 3. A simple approximation is to use a parabolic channel flow of width 2d and height 2B at the pore entrance and exit in the Hele-Shaw regions. This leads to the following relation between Q and the centerline velocity $u_o(L_2')$

$$u_o(L_2') = \frac{3Q}{8Bd} \qquad (2.18)$$

According to the Kedem-Katchalsky relations the volumetric flux J_v across the endothelium is

$$J_v = L_p(\Delta P - \sigma\Delta\pi) \qquad (2.19)$$

where L_p, the hydraulic conductivity, is defined by $(J_v/\Delta P)_{\Delta\pi=0}$. Because J_v is defined as the volumetric flow rate per unit surface area of capillary, we first need to relate J_v and Q. If L_j is the total junction length per unit capillary surface area, then $L_j/2D$ is the number of pores per unit surface area and hence $J_v = QL_j/2D = L_p\Delta P$ or

$$L_p = \frac{QL_j}{2D\Delta P} \tag{2.20}$$

Adding the results for the pressure drop across regions 1, 2 and 3. We obtain from equations (2.15), (2.16) and (2.17)

$$P_L - P_A = J_v(R_1 + R_2 + R_3) \tag{2.21}$$

where

$$R_i = 2D\,[3\mu L_i/4B^3D + (3\mu/2B^3d^2D) \times \sum_{n=1}^{\infty} \tanh(\lambda_n L_i)\,\sin^2(\lambda_n d)\,/\lambda_n^3\,]\,/\,L_j \qquad (i=1,3) \tag{2.22}$$

$$R_2 = \frac{8\mu L_2}{\pi r_p^4}\left(\frac{2D}{L_j}\right) \tag{2.23}$$

The hydraulic conductivity can thus be expressed only in terms of membrane structure parameters and is given by

$$L_p = [R_1 + R_2 + R_3]^{-1} \tag{2.24}$$

2.2.4 Model For Resistance of Bridging or Linking Molecules

The basic formulation just described for the interaction of small pores connecting two Hele-Shaw type flow regions can be easily modified to include the hydrodynamic resistance of either cross-linking molecules or transverse fine fibers in the wide portion of the cleft. The model for the latter can be viewed as an alternative formulation of the fiber matrix theory proposed by Curry and Michel

(1980) which is based on the Carmen-Kozeny equation. The later equation is an approximate expression which attempts to describe the hydraulic resistance of a random fibrous network in an infinite medium. This phenomenological equation is non-rigorous in that there is no attempt to satisfy the viscous flow boundary conditions on the surface of the fibers or the walls of the channel. In the present study, an idealized doubly periodic geometry will be assumed for the distribution of molecules or fibers as shown in Figure 2.2. The basic model for a cleft with bridging molecules for a non-interacting pore flow was proposed by Silberberg (1987). The mathematical approach is a straightforward adaption of the parallel sheet flow model developed by Lee and Fung (1969) for the flow past a circular cylinder and extended by Lee (1969) to a doubly periodic array of septal posts in a model for lung alveoli.

In Lee (1969) a two term doubly periodic solution to the Stokes' equation and equation of continuity is presented which approximately satisfies the no-slip boundary conditions on the surface of the circular cylinders in Figure 2.2 and the periodicity conditions for the cylinder configuration shown in this figure. Of particular interest in the present study is the relative resistance of the flow past a periodic unit with the cylinders arranged in a square diagonal array to the resistance if these cylinders are absent. This resistance ratio is given by

$$f = \frac{1-b_1 S}{1+b_1 S} \tag{2.25}$$

where S is the fiber solid fraction defined as

$$S = \frac{\pi a^2}{2w^2} \tag{2.26}$$

and b_1 is a constant determined by the solution of a complicated linear matrix equation given by Lee (1969). When the cylinders are far apart compared to their radii, as is the case of present interest, b_1 can be approximated by

$$b_1 = -\frac{K_2(\frac{\pi a}{2B})}{K_o(\frac{\pi a}{2B})} \tag{2.27}$$

where the K_n are modified Bessel functions of the second kind of order n. The approximate results described by equations (2.25) to (2.27) are shown in Lee (1969) to be very accurate when the spacing Δ between cylinders is greater than 2B and $B/a<5$. Experiments indicate, however, that global results such as the expression for the increased resistance (2.25) can be applied to even larger values of B/a although the no-slip boundary conditions may not be satisfied accurately at all points on the surface of the cylinders.

One would like to incorporate result (2.25) in the general expressions for the resistance of the interacting pore flows described by Eq. (2.22). Each periodic unit in Figure 2.2 contains numerous bridging fibers or molecules and thus the array of linking molecules can be viewed as a continuum rather than discrete cylindrical obstacles. Their effect is equivalent to increasing the local effective viscosity of the fluid to an effective value

$$\mu_{eff} = \frac{1-b_1 S}{1+b_1 S}\,\mu \tag{2.28}$$

in Eq. (2.2) for the Hele-Shaw flow. If the cylindrical posts are uniformly distributed the correction for viscosity will be the same everywhere and Eq. (2.22) needs only be modified by replacing μ by μ_{eff} in Eq. (2.28).

2.3 Results

(a) Input Parameters

The important geometrical parameters that appear in the model are the junction length per unit capillary wall area L_j, cleft depth L, position of the proteins strands L_1/L, junctional strand pore radius r_p, junction pore length $L_2=2nr_p$, cleft width 2B, distance between junction pores 2D and the radius a and spacing 2W of the bridging molecules or fibers. Three of these parameters L_j, 2B and r_p are well documented by available data and do not appear to vary significantly between capillaries in different tissues. With small deviations values for L_j and 2B that are representative of frog, rat and dog skeletal muscle and diaphragm (Crone and Levitt, 1984) are 2000 cm/cm^2 and 17 nm respectively. As noted already in Figure 2.3 the value for r_p of 5.5 nm provides a very reasonable fit to the large body of available data for the reflection coefficient data for tracer molecules less than 3.5 nm radius. Although this value of r_p will be used as our initial estimate, we shall want to discuss (i) the effect of pore diameter on L_p, to demonstrate that the hydraulic conductance will no longer vary as the fourth power of the radius when the interaction between the pores is considered, and (ii) the effect of concentration gradients in the wide part of the cleft on σ. All the other parameters in the model will be varied to show how L_p is affected by their change. In particular, we shall want to examine how the location of the protein strand, the number of protein strands, the cleft depth, the spacing of the pores and the presence of fibers or bridging molecules alters the hydraulic conductivity of the cleft. Each of these factors will now be considered separately.

(b) Effect of the Position of Protein Strand

Freeze fracture and transmission electron microscopic studies indicate that the junctional protein strand can appear in any position between the lumen and tissue fronts of the cleft. This effect is

readily examined by varying the value of L_1/L between zero and one. Results are shown in Figure 2.4 for three representative values of the pore spacing, 2D equal 50, 200 and 1000 nm. This corresponds approximately to one missing junctional protein in 5, 20 and 100 respectively. It is clear from this figure that the relative position of the protein strand has virtually no effect on the hydraulic conductivity. A similar analysis could also be performed for two or more junctional strands in series. This analysis would lead to results that are similar to those shown for a single strand provided the spacing between strands is small compared to the cleft depth. The effect of multiple strands in this case is just additive and their relative position not significant.

(c) Effect of Cleft Depth

The cleft depth has been shown to vary significantly between various tissues. Commonly quoted values range from 700 nm for frog mesentery (Crone and Levitt, 1984) to 900 nm for skeletal muscle capillaries to 1400 nm for adult lung capillaries (Perry 1980). Results are shown in Figure 2.5 for five representative pore spacings. When the pores are more than 500 nm apart (roughly one junctional protein in 50 missing) the cleft depth plays a very minor role. In this case most of the hydraulic resistance is associated with the junctional strands and the interaction between pores in the wide part of the cleft is not important. As the pore spacing decreases to less than 200 nm, the effect of cleft depth becomes significant since the resistance of the wide portion of the channel becomes comparable to the pores themselves.

(d) Effect of Pore Diameter

The effect of pore radius is shown in Figure 2.6 for five representative pore spacings from 22 to 1000 nm. As noted previously the most commonly accepted value for the equivalent pore radius is 5.5 nm, which lies in the middle of the range for the values of r_p shown

in Figure 2.3. The striking feature of this figure is that L_p varies nearly linearly with increasing radius rather than as the fourth power of the radius (dashed curve in Figure 2.6), as would be the case for isolated non-interacting pores. The curve for L_p changes from slightly concave upward to downward as the pore spacing decreases. Normally one would anticipate that L_p would increase by roughly a factor of nine as the pore radius increases from 4.0 to 7.0 nm, according to the fourth power relationship, whereas the results in Figure 2.6 indicate only about one quarter this increase for 2D equal 22 nm and one half this increase for 2D equal 200 nm. The changing variation in L_p with r_p can be explained by the fact that whereas the resistance of the pores decreases as r_p increases there is an offsetting increase in the resistance of the interacting pore flow in the wide portion of the cleft whose magnitude increases significantly as the pore spacing decreases. For large pore spacing, 2D = 1000 nm, the increase in L_p approaches the fourth power relationship characteristic of an isolated pore.

(e) Effect of Pore Length

The pore length L_2 depends on the number of junctional protein strands in series. Each strand contributes a length of approximately 11 nm to L_2 and $L_2/2r_p$ is the average number of protein strands. In Figure 2.7 we have plotted how the total resistance increases with increasing strand number for five characteristic pore spacings. The curves show a linear increase in resistance with increasing strand number.

(f) Effect of Pore Spacing

The effect of pore spacing is the single most important parameter in determining L_p. Results are shown in Figure 2.8 for junctions with one to five protein strands and pore spacings between 22 and 1400 nm. A central assumption in previous analyses is that the hydraulic conductivity is proportional to the number of pores, since the latter

is proportional to the length of open cleft. The basic fallacy of this argument is shown in Figure 2.9 where L_p is plotted vs. $L_j/2D$, the number of pores or missing proteins per cm^2 of capillary surface area. When 2D is 200 nm, or roughly one protein in twenty is missing, there will be 10^8 pores/cm^2 if L_j = 2000 cm/cm^2. It is clear from this figure that when the pores are very far apart L_p is proportional to the number of pores, but that when the pores are close together L_p changes much less with spacing. The dashed lines in Figure 2.9 show how L_p would change if the hydraulic conductivity were proportional to the number of pores. The closest spacing that has been suggested in the literature is 22 nm (Firth *et al.*, 1983), where the junction strands are proposed to be alternating arrangement of junction bars and spaces, the latter being roughly 11 nm in length and 5 nm height. $L_j/2D$ for this close pore arrangement is 9×10^8. At very close pore spacings the resistance of the cleft is dominated by the interaction between the pores and the open pore area is of much less importance. As the number of protein strands increases, the pore resistance itself increases and the linear relationship between hydraulic conductivity and number of pores applies to somewhat closer pore spacings (note the point of deviation of the solid curves in Figure 2.9 from the dashed curves for the linear area relation).

(g) Effect of Junction Slit Length

In previous analyses the pores in the junction strands have not been the small effective circular cylindrical holes of 5.5 nm radius, as proposed in this study, but long rectangular slits of 500 nm length (Lassen and Trap-Jensen, 1970; Perl, 1975; Casley-Smith *et al.*, 1975; curry and Michel, 1980) or tortuous paths with breaks of at least 40 nm length (Wissig, 1979) (standard transmission electron microscopic section thickness). The basic question one asks is what is the relative contribution to the hydraulic conductivity of a small number of larger breaks (the tortuous pathways suggested by Wissig) compared

to the much more frequent 10-20 nm small gaps observed by Bundgaard (1984)? This question is addressed in Figure 2.10 where we have plotted the resistance of a cleft with periodically distributed rectangular slits as a function of slit length 2d for representative values of d/D, the fractional length of open cleft. The smallest value of 2d is 11 nm, the slit length corresponding to the alternating arrangement of junctional bars and spaces suggested by Firth *et al.* (1983), and the longest slit 500 nm as first proposed by Casley-Smith *et al.* (1975).

To make the comparison just described we have assumed in Figure 2.10 that the junctional pores are rectangular slits of variable length 2d, height 2b equal to 6 nm and depth L_2 equal to the thickness of a single protein strand 11 nm. A parabolic velocity profile is assumed in the slit. This leads to an equation for the hydraulic resistance in which equation (2.23) for a circular pore is replaced by $R_2 = (12\mu L_2/8b^3)(D/dL_j)$. The interaction between slits is treated in the same manner as the periodic Hele-Shaw model shown in Figure 2.2 for our equivalent circular cylindrical pore model. The entrance profile in the Hele-Shaw region is assumed to be parabolic, and the centerline velocity at the slit exit is chosen to satisfy the continuity relation $u_0 \times 17\ \text{nm} = u_s \times 6\ \text{nm}$ where u_s is the centerline velocity of the slit. One notes that there is a significant increase in resistance for a fixed value of d/D as the slit length is increased. This results from the factor as the slit length increases for a fixed value of d/D, the aspect ratio $2D/L_3$ of each periodic unit in the model increases and the interaction between the slits decreases. High aspect ratio periodic units ($2D/L_3 > 3$) do not significantly interact with one another and have a larger resistance since they never achieve the nearly uniform flow that would be obtained at large distance from the slit exit in a low aspect ratio periodic unit.

(h) Effect of Linking Molecules and Transverse Fibers in Wide Regions

The effect of having bridging molecules or a fine transverse fiber matrix in the wide portion of the cleft where there is an interacting Hele-Shaw flow is show in Figure 2.11. This theory is based on the modifications of equations (2.22) and (2.24) using equations (2.27) and (2.28) to describe the additional viscous resistance of cross-bridging molecules if arranged in a square array as shown in Figure 2.2. Three types of linking molecules are considered. The smallest a=0.6 nm is representative of a sulphated proteoglycan that has been hypothesized to be the basic matrix element in the fiber matrix theory. The largest a=5.0 nm represents the cross-bridging molecules that Firth *et al.* (1983) hypothesized might exist based on the pattern of staining they observed. For a=0.6 nm, the theory predicts very large increases in resistance (L_p approaches zero) when the solidity ratio S=0.013. This occurs because the viscous regions surrounding the fibers start to overlap causing a huge increase in resistance of the fiber matrix. In the limit of slender linking molecules, where the aspect ratio B/a is large, the two term asymptotic approximation becomes an increasingly poor approximation when the viscous layer overlap, since the no slip conditions on the fibers are not well satisfied. Also shown in the left hand margin is the limiting value of L_p if the junction strand was removed and only the periodic fiber array was present.

In Figure 2.12, one has plotted a comparison of the predictions for L_p of the Carmen-Kozeny equation used by Curry (1986) to describe the effect of cross-bridging fibers and the present Hele-Shaw approximation for the flow past a periodic array of cross-bridging fibers. For purposes of this comparison the junction strands have been removed and the resistance is due exclusively to the fibers and the confining boundaries in the case of Hele-Shaw approximation. The expression given in Curry (1986) is

$$L_p = \frac{2BL_j}{L\mu} \left(\frac{(1-S)^3 a^2}{S^2 \quad 20}\right) \tag{2.29}$$

The results have been plotted for the same three values of a as Figure 2.11. Since the spacing between posts at given value od S varies with post radius, symbols denoting constant spacing are also shown in Figure 2.12. For reasons, which we shall elaborate on in the discussion section, one believe that the results for the periodic Hele-Shaw model are accurate only when $\Delta > 2B$. It is clear from the results in this figure that equation (2.29) underestimate the hydraulic resistance of a cross-linking fiber matrix for a given value of S by several order of magnitude at the values of S in the range of physiological interest, $S < 0.1$.

2.4 Summary

(a) Predicted Pore Spacings for Various Tissues

A large body of experimental data exists for the measured hydraulic conductivity of both frog and mammalian capillaries and is summarized by Crone and Levitt (1984) and Michel (1984). The average values for frog mesentery and muscle when albumin is present in physiological concentrations are $L_p = 5.0$ and 0.75×10^{-7} cm/s/cm H_2O respectively. These experiments have received considerable attention since these are based on single perfused capillaries in which the osmotic reflection coefficient for sucrose has been simultaneously measured and shown to be nearly identical (Curry *et al.*, 1976; Curry and Frokjaer-Jensen, 1984). This is generally interpreted, as noted earlier, as indicating that the size sieving structure is the same in both capillaries and it is the length of open junction that varies between these two tissues. Also, as shown in Figure 2.3, the osmotic reflection coefficient varies only slightly between frog and mammalian tissues suggesting that basic structure, which we shall discuss in greater depth shortly, is common to most capillary endothelium. We

shall consider first the predictions of our basic model for L_p and then discuss in the next section how these results would be modified by a matrix of cross-bridging molecules in the wide portion of the cleft.

The result in Figure 2.8 predict that the measured value of L_p for frog mesentery can be achieved with one junctional strand and a pore with r_p=5.5 nm located approximately every 80 nm or two junction strands and a pore located every 40 nm. There are no freeze cleavage studies of frog mesentery junctions; however, the serial section transmission electron microscopic studies by Bundgaard and Frojaer-Jensen (1982) indicate between one and three punctate regions of close apposition, with virtually all sections in true capillaries showing one such region. Since multiple strands will offer little resistance in excess of that created by a single continuous strand unless they also form a close loop, it is likely that a highly permeable cleft, like frog mesentery, is best represented in our model by a single strand with one junctional protein in roughly eight missing from the strand. The equivalent predictions from Figure 2.8 for frog muscle capillaries indicate that for one strand the measured value of L_p will be achieve when 2D is 750 nm or when 2D is 400 nm if two full strands are present. This suggests that somewhere between 1 in 75 and 1 in 40 junctional proteins are missing from the particle strands in frog muscle.

The foregoing predictions of the pore interaction model for frog muscle and mesentery capillaries suggests a much tighter structure than the one dimensional simple constricted slit models analyzed by previous investigators (Crone and Levitt, 1984; Lassen and Trap-Jensen, 1970; Perl, 1972; Casley-Smith *et al.*, 1975; Perry, 1980). For example, the model by Crone and Levitt (1984) suggests, based on measurements of hydraulic conductivity and potassium ion permeability, that as much as 80 percent of the junction length L_j needs to be open

in frog mesentery and 10 percent of L_j open in frog muscle. Although junction freeze cleavage studies are not presently available for frog capillaries, hydraulic conductivity and solute permeability measurements for frog muscle and mammalian heart, lung and skeletal muscle differ by less than a factor of two, suggesting that the junctional protein structure for these tissue is probably quite similar. Freeze cleavage studies in all mammalian muscle tissues and guinea-pig placenta (Simionescu *et al.*, 1975; Wissig, 1979; Firth *et al.*, 1983) do not indicate large breaks occupying 10 or more percent of particle junction strands. The present model predictions of randomly spaced single missing proteins is much more consistent with the observations of these freeze cleavage studies. Measurements of L_p in mammalian muscle capillaries range from 0.7×10^{-7} cm/s/cm H_2O for rabbit heart capillaries to roughly half these values in lung and skeletal muscle. For a single protein strand this could be achieved with only on particle in 150 being missing for mammalian lung and skeletal muscle or one particle in 90 if two continuous strands are present.

The reasons that the present model predicts a significantly more complete junction structure and a significantly smaller hydraulic resistance for a given length of open junction that previous non-interacting pore theories are that (i) the hydraulic conductivity is not proportional to the open area as assumed in previous isolated pore models, see Figure 2.9, and (ii) there is redistribution of the pressure field in the cleft such that the flow does not obey the usual Poiseuille resistance laws (see Figure 2.6) which are the basis for all the simple one-dimensional slit models. The hydraulic conductivity with pore interaction obeys a power law which is less than the third power of the cleft height or the fourth power of the pore radius as the case may be. The deviation from the linear relationship between number or pores (or open pore length) and L_p is

particularly important when there is single effective tight junction strand. From Figure 2.9 significant differences are to be expected unless the missing proteins are spaced far apart.

(b) Possible Role of Fine Fibers and Linking Molecules

One believes that the results in Figure 2.11 for L_p provide a substantially more accurate description of the effect of cross linking molecules, fine fibers and other molecular structures in the wide portion of the cleft than the fiber matrix theory (Curry and Michel, 1980). The theoretical basis for the solute permeability aspects of the fiber matrix theory rests on a well developed stochastic analysis of the exclusion and diffusion of particles in a fibrous network that was developed for long chain polymer molecules (Ogston *et al.*, 1973). However, the hydrodynamic aspects of the fiber matrix theory which lead to equation (2.29) for L_p are based on a much less rigorous foundation that is either a largely empirical extension of the hydraulic radius concept (Curry, 1984; Curry and Michel, 1980) or a simple model for the drag on non-interacting cylinders aligned either parallel or perpendicular to the flow direction (Iberall, 1950). The hydrodynamic theory developed herein should be much more realistic, since it takes account of the resistance of the channel walls, the interaction between pores, the no-slip conditions on the surface of cross-linking molecules and the hydrodynamic interaction of these molecules.

The calculations presented by Curry (1984, 86) and Curry and Michel (1980) shows that for frog mesentery capillaries the measured permeability properties can be accounted for by a matrix consisting of fibers which are 0.6 nm in radius which occupy 5 percent of the matrix volume. Somewhat smaller fibers of 0.3 nm radius occupying 3 percent of the matrix volume were needed to describe the diffusion permeability of mammalian heart muscle capillaries, whose hydraulic conductivity, as mentioned above, was approximately 1/15 that of frog

mesentery. The results shown in Figure 2.11 are incongruous with these predictions. Using transverse fibers that are 0.6 nm with a matrix volume of 1.3 percent (curve 10, 1-S=0.987), one finds that the maximum possible value of L_p when no junction is present, 5.0×10^{-8} cm/s/cm-H_2O, is an order of magnitude less than the measured value for frog mesentery, 5.0×10^{-7} cm/s/cm-H_2O.

Results are not given for larger values of the solid fraction S because they are beyond the range where the simplified asymptotic approximation given by equation (2.27) would be accurate. For a looser matrix (curve 6, 1-S=0.995), where the fibers are 0.5 percent of the matrix volume, an L_p of 5.0×10^{-7} cm/s/cm-H_2O can be achieved if every other protein is missing. The essential point is that while the basic interacting pore model without linking molecules (uppermost curve in Figure 2.11) can satisfy the measured hydraulic conductivity for frog mesentery in what would appear to be a realistic fashion (one missing junction particle in eight) the presence of cross linking proteoglycan fibers in a volume fraction of less than one percent would so increase the resistance of the cleft that it would not be possible to satisfy the L_p measurements even if one junction particle in two were missing. For more slender fibers the situation is even worse. If a=0.3 nm, the size of the fibers indicated by the fiber matrix theory for mammalian heart capillaries, the present theory predicts that the volume fraction of the fibers would need to be less than 0.1 percent (curves omitted in Figure 2.11 to prevent crowding) to match the measured permeability for the smallest value of 2D shown.

For large cross-bridging molecules, a=5 nm, the results in Figure 2.11 show that the decrease in L_p is approximately the same as for the fine fiber matrix just described when the open gap Δ between posts is equal. The reason for this is that the detailed solutions for the velocity profiles near the fibers show that the region of influence of the viscosity and hence the increase in drag, is determined primarily

by the height of the cleft 2B and not the diameter of the fibers and typically extends about one channel height from the surface of the fibers. Large increases in drag due to cross-linking molecules occur when the viscous regions surrounding them overlap. Long slender bridging molecules therefore have almost as much influence on the hydraulic resistance as larger molecules when the open distance between the bridging molecules $\Delta = \sqrt{2}w - 2a$ is the same. This is evidence when one compares the results for a = 1 nm and 1-S = 0.972 (curve 9), a = 0.6 nm and 1-S = 0.987 (curve 10), and a = 5 nm and 1-S = 0.77 (curve 11) in Figure 2.11. These curves, for which Δ is roughly half the cleft height 17 nm, have nearly the same values of L_p although the volume fraction of the posts increases by nearly a factor of twenty when 1-S decreases from 0.987 to 0.77. For the reasons states earlier a more rigorous analysis than the two-term approximation by Lee (1969) needs to be developed for an ordered array when there is a viscous interaction between the boundary layers surrounding the matrix fibers or cross-linking molecules and this is particularly important when $B/2a > 5$. The present results in Figure 2.11 have therefore been limited to values of Δ which are roughly half the channel height or greater. A second important consideration which needs to be examined is the effect of the orientation of the fibers relative to the channel wall. For non-transverse fibers the flow in the inviscidly behaving outer regions will still be parallel sheet flow and thus this flow will see a fiber whose effective shape is a cross-section through the fiber in a plane parallel to the channel wall. Fiber orientation should therefore not change the qualitative nature of the flow behavior.

From equation (2.26) the spacing of the posts at the same value of the solidity ratio increases in proportion to the radius of the post. Thus a post array formed by large proteins of radius a = 5 nm will have a spacing which is 8.3 times that for a fine cross linking

fiber of radius a = 0.6 nm at the same value of S whereas the region of influence of the no-slip boundary conditions will be almost the same for the large molecule and the fine fiber. Thus, relatively small increases in hydraulic resistance are observed in Figure 2.11 for the addition of 5 nm radius posts at 1-S = 0.97 (curve 4), a fiber volume fraction of 3 percent (open gap between posts in this case is 41.2 nm and viscous regions around neighboring posting do not overlap). These modest changes in hydraulic resistance for large bridging proteins were previously predicted for the non-interacting pore model (Hsing, 1984). At present there is only very limited evidence for the presence of large bridging proteins. The tannic acid staining pattern first reported by Firth *et al.* (1983) which suggested the possible existence of these molecules in the wide regions of the clefts of guinea-pig placenta have not been observed in the more recent studies of rat cardiac capillaries by these same investigators (Ward *et al.*, 1988) or is there any evidence for their existence in freeze cleavage electron micrographs where the fracture plane is perpendicular to the plane of the cleft.

The results in Figure 2.12 illustrate a fundamental inadequacy of Carmen-Kozeny equation in estimating the hydraulic resistance of a fiber matrix in a channel whose width is comparable to the fiber length dimensions. Since the vortical layers near the channel sidewalls fill the entire channel height, the interaction of the vortical layer with the fibers produces a viscous boundary layer in the vicinity of the fiber which is of comparable dimensions. For slender fibers viscosity has a region of influence which is much larger than the fiber radius. The applicability of the fiber matrix theory for predicting the diffusive permeability in a channel with cross-linking fibers will be examined in chapter 3. Qualitatively, one would expect the influence of the channel sidewalls to be less important since the concentration gradient across the channel height

should be small. The results of the present Hele-Shaw model shown in Figure 2.12 are conservative in that the periodic array will have an hydraulic resistance which is roughly a factor of two larger than a random array with the same solid volume fraction.

The value of L_p of 5.0×10^{-7} cm/s/cm-H_2O is typical of frog mesentery capillaries in which there are small amounts of albumin in the perfusate. Values for L_p in pure Ringer solution are roughly four times this value (Curry, 1986). The results for a channel without posts or junctional strands in Figure 2.12 when S = 1 reveal that the maximum possible value of L_p is 11×10^{-7} cm/s/cm-H_2O when L_j= 2000 cm/cm^2, 2B = 17 nm. Electron microscopic studies by Cough and Michel (1988) reported this same value of L_j but a larger average value for 2B, 22 nm, and a smaller average value of L, 400 nm . Using these dimensions the maximum value of L_p for a channel without junctions or posts is 41×10^{-7} cm/s/cm-H_2O since the hydraulic resistance decreases as the third power of the channel height and is proportional to the length. If these dimensions are used in constructing the curves in Figure 2.11 one finds that in the basic model without bridging fibers one junction protein in approximately 30 (2D = 300 nm) needs to be missing to reduce L_p to 5.9×10^{-7} cm/s/cm-H_2O, the average value of L_p measured by Cough and Michel (1988), and one junctional protein in 10 (2D = 100 nm) missing to reduce L_p to 20×10^{-7} cm/s/cm-H_2O, the value typical for pure Ringer perfusate. The possible mechanisms for this decrease in L_p when serum albumin is present in the perfusate and the concomitant effect on the osmotic reflection coefficient will be discuss next.

(c) Osmotic Reflection Coefficient

The presence of concentration gradient in the wide portion of the cleft can alter the effective osmotic pressure across in the pores in the junctional strands since it alters the effective gradient across the latter. A simple one-dimensional series model can be

constructed to approximate this effect on σ. In this approximation the wide part of the cleft and the pore, which we denote by the subscripts 1 and 2 respectively, can be combined to define an overall diffusive permeability and osmotic reflection coefficient. These are given by

$$\frac{1}{\bar{\omega}} = \frac{1}{\omega_1} + \frac{1}{\omega_2} \tag{2.30}$$

$$\frac{\bar{\sigma}}{\bar{\omega}} = \frac{\sigma_1}{\omega_1} + \frac{\sigma_2}{\omega_2} \tag{2.31}$$

The expressions for the diffusive permeability using the dimensions in Figure 2.2 are

$$\omega_1 = \frac{A_1}{L_1}(1-\alpha_1)F_1(\alpha)D_\infty, \qquad \omega_2 = \frac{A_2}{L_2}(1-\alpha_2)^2F_2(\alpha)D_\infty \tag{2.32a,b}$$

where $A_1 = 4BD$, $A_2 = \pi r_p^2$ and $\alpha_{1,2}$ are the ratios of the diameter of the transported molecule to either the width $2B = 17$ nm of the cleft or diameter $2r_p = 11$ nm of the pore. The $F(\alpha)$ are hydrodynamic interaction functions describing the resistance of a sphere translating along the axis of a channel or a circular cylinder (Curry, 1984). The values of σ_1 and σ_2 are also functions of α and are determined for the channel geometry by Ganatos (1981) and the pore geometry by Curry (1984). For an albumin molecule with an effective diameter of 7 nm $\alpha_1 = 0.412$ and $\alpha_2 = 0.636$. The corresponding values of σ_1 and σ_2 are respectively 0.308 and 0.8. For frog mesentery, where we estimated $2D = 80$ nm, one finds using the above formulas that $\omega_2/\omega_1 = 0.112$, $\bar{\omega} = 0.90\omega_2$ and $\bar{\sigma} = 0.93\sigma_2$. For frog muscle, where we estimated $2D = 750$ nm, one finds using the above formulas that $\omega_2/\omega_1 = 0.012$, $\bar{\omega} = 0.988\omega_2$ and $\bar{\sigma} = 0.99\sigma_2$. One thus concludes that for frog mesentery the effect of the wide portion of the cleft on $\bar{\sigma}$ or $\bar{\omega}$ is

less than 10 percent and for frog muscle of the order of one percent. Both these estimates neglect the effects of cross-linking fibers in the wide portion.

The mechanism via which albumin in small concentrations affects L_p and σ has been studied extensively over the past decade. It has recently been shown that the effective osmotic pressure of myoglobin can be reduced as much as 60 percent when albumin is removed from the perfusate (Curry, 1987). The albumin could adhere to the negative surface charge on the plasmalemma membranes of the clefts, effectively narrowing the wide portion of the channel, on fibers throughout the wide portion of the channel or at the entrance region to the pores formed by the missing junctional particles as we propose herein. These equations are important in determining the nature of the molecular sieve. To determine the nature of the molecular sieve, one needs to develop more rigorous theories for water filtration, solute diffusion through a confined fibrous bed and a theory for the osmotic reflection coefficient for pores of noncircular cross-section. In a recent paper the authors have theoretically shown that for short membrane pores significant changes in osmotic pressure can result from changes in the solute concentration field confined to an entrance region whose dimensions are only a few times the pore entrance diameter (Yan *et al.*, 1986).

(d) Relative Importance of Small Gap and Larger Tortuous Pathways

Three alternative pathways have emerged from recent electron microscopic studies (Wissig, 1979; Firth *et al.*, 1983; Bundgaard and Frokjaer-Jensen, 1982; Bundgaard, 1984) for the junctional pathway via which water and small hydrophilic solutes cross the endothelium. (i) Wissig (1979) has proposed the existence of tortuous pathways caused be occasional wider breaks in the protein strands as schematically shown in Figure 2.1 based on his freeze cleavage studies. (ii) Bundgaard (1984) has observed the existence of much shorter 5-30 nm

gaps (10-20 nm depending on interpretation) of approximately 4 nm width in his ultrathin 12.5 nm sections, in addition to the much less frequent longer breaks of Wissig. (iii) Firth *et al.* (1983) have proposed that the junctional lines can be subdivided into uniformly spaced rectangular pores and junctional bars in which each occupy approximately 50 percent of the junctional lines, see sketch (b) of Figure 2.13. The serial reconstructions of the rat heart capillaries (Bundgaard, 1984) provide arguably the most complete three dimensional transmission electron microscopic picture presently available. Two types of serial reconstructions were undertaken. A long series of 190 sections, each of approximately 40 nm thickness, covering 8 μm of cleft length and a short series of 16 ultrathin 12.5 nm sections. The short 10-20 nm long 4-6 nm wide gaps are only visible in these ultrathin sections since the gap length must be at least half the section thickness to be visible. Seven longer breaks visible in one or two 40 nm adjacent sections were observed. These breaks could very well represent the tortuous pathways proposed by Wissig (1979). Their statistical frequency, however, was only 1/12 that of the short gaps.

The results in Figures 2.8, 2.9, 2.10 provide valuable information in interpreting the plausibility of each of the three alternative views for the small pore. The curves in Figures 2.8 or 2.9 predict that a single junctional strand with an alternating arrangement of junctional bars and spaces, each of 11 nm length, as suggested by Firth *et al.* (1983), will have an hydraulic conductivity $L_p = 8.5 \times 10^{-7}$ cm/s/cm-H_2O when 2D is 22 nm. This is nearly a factor of two larger than that for frog mesentery and a factor of twenty greater than for most muscle tissues. This junctional barrier is much too porous. A more likely interpretation of the spacing of the particles and their arrangement based on the observations by Firth *et al.* (1983) will be discussed in the next section. Using the results in Figure 2.10 we can estimate the relative importance of tortuous gaps of 40 to

80 nm length compared to the 12 times more numerous short gaps observed by Bundgaard (1984). If our hypothesis is correct, that these short gaps are holes formed by individual missing proteins in a continuous particle strand, these pores are of length 2d = 11 nm. Using an average length 2d = 60 nm for the tortuous gaps and an average spacing of 2D = 1100 nm between each tortuous pathway, one estimates that $d/D \approx 0.05$ for this pore. The average spacing 2D between the small gaps is approximately 90 nm, thus $d/D \approx 0.1$ for this pore. Referring to Figure 2.10, one concluded that the resistance of the tortuous path is roughly twice that of the small gaps. Since these pathways run in parallel about twice as much water should pass through the small gaps as the larger tortuous pathways.

In the earlier slit models (Curry, 1980; Gosselin and Stibitz, 1977) a long rectangular slit of length 2d = 500 nm was assumed to occur every 10 μm. The fractional length of open junction d/D for this model was 0.05. The results in Figure 2.10 show that the resistance of these long rectangular slits is approximately four times the short gaps observed in Bundgaard (1984) although the total open length of the short gaps is only twice that of the long slits. The long slits are too widely separated to interact with one another and thus their resistance on a unit open area basis is greater than for the interacting small gaps.

(e) Various Models for Junctional Protein Structure

In Figure 2.13 three alternative sketches are shown for the arrangements of the abutting strands and the intramembrane particle configuration that provides for the small pore. Configuration (a) gives rise to the long rectangular slit model that is the basis for the theoretical models by Lassen and Trap-Jensen (1970), Perl (1971), Casley-Smith *et al.* (1975), Perry (1980), and Gosselin and Stibitz (1977). Configuration (b) has been proposed by Firth *et al.* (1983) based on the interpretation of the arrangement of the tight junction

proteins initially suggested by Simionescu *et al.* (1978). In the latter paper it is hypothesized that the tight junction proteins appear as symmetric matching pairs in opposing plasmalemma. Thus if the proteins themselves are 11 nm wide (based on measurements of these particles perpendicular to the shadowing direction) and the average spacing seen on the outer leaflet in the freeze cleavage electronmicrographs of these placenta capillaries is 22 nm, an arrangement of nearly equal junctional bars and spaces as sketched in (b) is obtained. Configuration (c), an alternating zipper arrangement with occasional missing proteins, is our own interpretation of the observations by Firth *et al.* (1983). Important unanswered questions in pattern (b) are what provides for the regularity of the spaces and why are these spaces roughly of the same dimensions as the diameter of the junctional particles? Configuration (c) provides a simple rational geometrical explanation to both these questions. Furthermore, as discussed in the previous section, configuration (b) provides for far too large an hydraulic conductivity for most tissues, even when no tortuous pathways are present.

The choice between configuration (a) and (c) in Figure 2.13 can be based on several argument. First the long slits of 500 nm length proposed by Casely-Smith *et al.* (1975) have not been observed using the more recent three-dimensional serial sectioning techniques (Bundgaard and Frokjaer-Jensen, 1982; Bundgaard, 1984); the longest gaps observed are breaks of the type described for the tortuous pathway (one or two standard electron micrographic section thicknesses). Second, estimates of the fractional length of junction required to accommodate the measured hydraulic conductivity of capillaries in various tissues, see Figure 2.10, suggest that it is more efficient to have a large number of small pores corresponding to individual missing proteins than a few long slits. Third, there is no reason for the long breaks of the type shown in configuration (a) to

appear in thin section with constricted regions and these rectangular slits should be open to the full cleft width of 17nm. Slits with these dimensions do not satisfy the theoretical curves in Figure 2.3 for the osmotic reflection coefficient. Recent studies of rat cardiac capillaries using goniometric tilting techniques indicate that the average gap height at the point of closest apposition in the junction region is 5.4 nm (this estimate does not include tissue shrinkage) and that horseradish peroxidase (dia. 6 nm) could pass through these openings whereas haemoglobin (6.4 nm) could not (Ward *et al.*, 1988). This sharp cut off and the closeness of these three dimensions suggests that the maximum width of the pore could well be determined by a rather rigid structure as proposed in configuration (c). Finally, as mentioned in section (c) of the discussion, the 6 by 11 nm rectangular pores in configuration (c) come very close to providing the equivalent cylindrical pore dimensions for the osmotic reflection indicated by the data in Figure 2.3.

(e) Implications for Solute Permeability

An important conclusion from this study is that the fractional length of open junction required to accommodate the measured water fluxes in frog mesentery and muscle tissue is much less than previously though possible. The diffusional resistance for a cleft with this junctional strand opening has two important features. First, the solute permeability coefficient should be significantly lower than for existing slit models because of the interaction between the pores and hopefully account for the factor of five difference between the theoretically predicted and measured values for molecules between 1.5 to 3.5 nm radius. Second, the junctional strand in a model for diffusion through interacting pores should offer relatively little resistance to small solutes and yet a high resistance to larger molecules that approach the pore dimensions. This feature should help the model bringing down the diffusive permeability for solutes with

size close to albumin. The parallel studies for solute diffusion will be carried out later in this thesis.

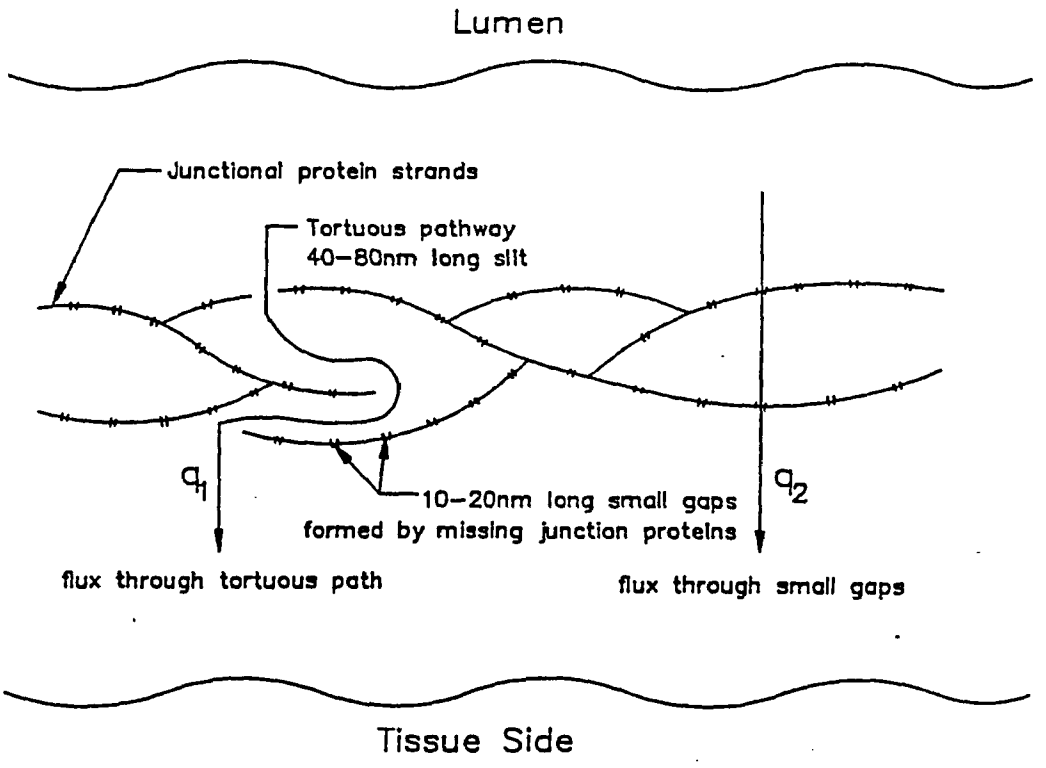

Fig.2.1: Diagrammatic sketch of interwoven array of junctional protein strands showing filtration flux q_1 through tortuous pathway (40-80 nm slit length, Wissig (1979)) and flux q_2 through small gaps (10-20 nm, Bundgaard (1984)) hypothesized in present study to be formed by occasional missing proteins.

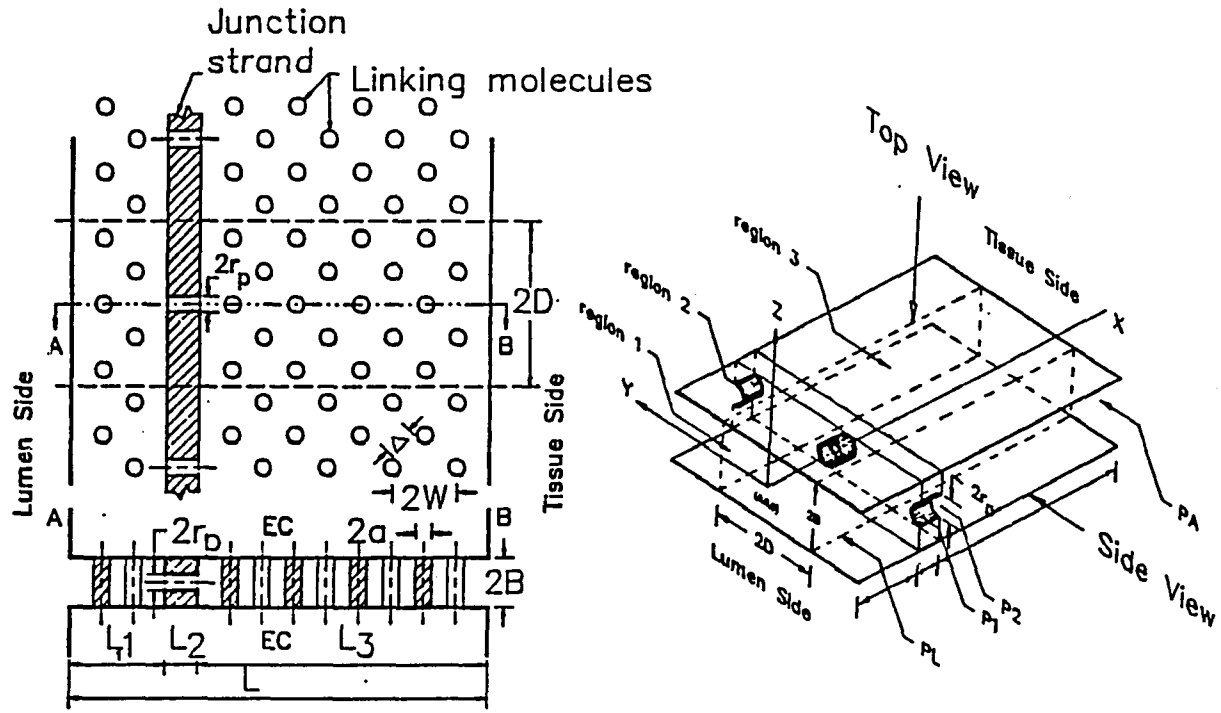

Fig.2.2: Sketch of simplified mathematical model of intracellular channel. (a) Three dimensional diagram. (b) Top view and Side view. Protein strand with periodic holes lies parallel to luminal front. L is total cleft depth. L_1, L_3 are depths between protein strand and lumen and albuminal margins of cleft. L_2 is total depth of holes in protein strand, and r_p is effective radius of pores formed by missing protein holes. Within wide portion of cleft cross-linking molecules or fibers are represented by a periodic diagonal array of cylindrical post (which are omitted in three dimensional diagram). The diameter of these posts is 2a and the distance between two adjacent posts is 2W. These posts are perpendicular to the plasmalemma forming the interendothelial channel. The mathematical model is for one periodic unit of width 2D.

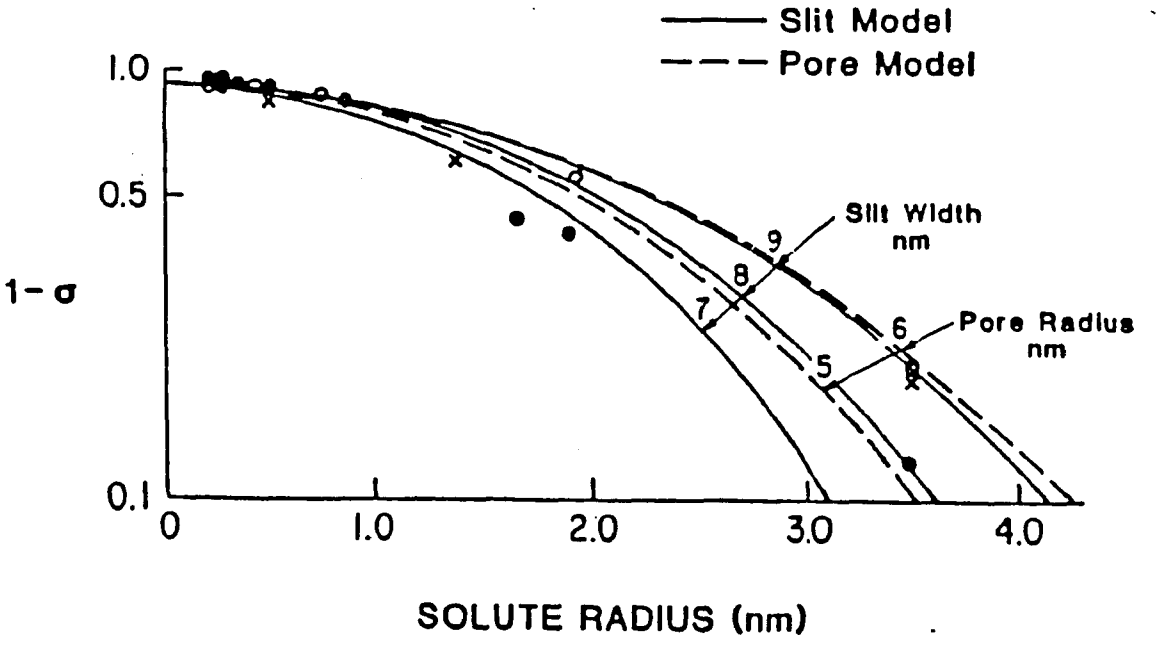

Fig.2.3: Analysis of the selectivity properties of the capillary wall based on measured values of the osmotic reflection coefficient. Values are shown for rabbit heart (0), rat hindquarters (×), and frog mesentery (o). The intercept of 0.9 on the ordinate indicates that 90 % of the capillary hydraulic conductivity can be accounted for the junctional pathway (see Curry *et al.* (1976) and Curry (1984) for further details of this analysis). Measured reflection coefficients are described in terms of exclusion from a rectangular slit 7-9 nm wide or a cylindrical pore 5-6 nm in radius. The solid lines are based on the hydrodynamic slit theory of Ganatos *et al.* (1981) and the broken lines on hydrodynamic cylindrical pore theory of Anderson and Malone (1974). (with permission of F. E. Curry (1986))

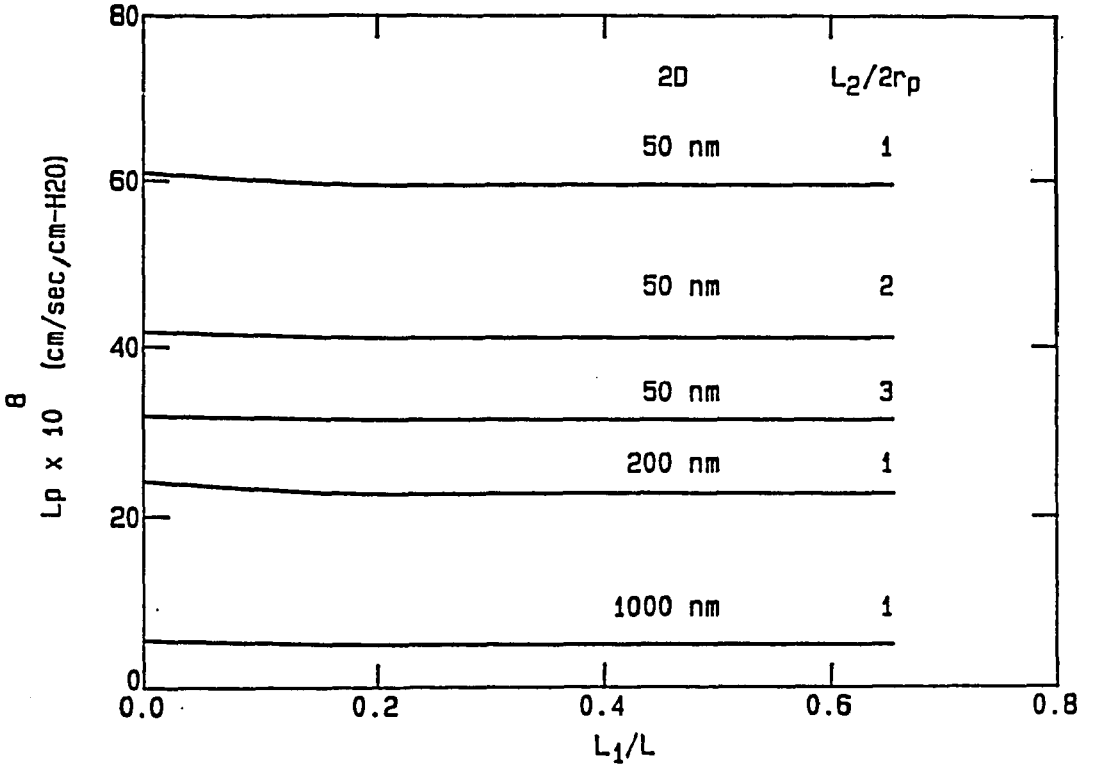

Fig.2.4: Effect of the position of protein strands. L_1 is the depth between protein strand and luminal front. Three representative values of the pore spacing, 2D equal 50, 200, and 1000 nm are shown. These values correspond to approximately one missing protein in 5, 20 and 100 junctional proteins. Pore radius r_p = 5.5 nm, total cleft depth L is 700nm, and results are shown for $L_2/2r_p$ equal 1, 2, and 3.

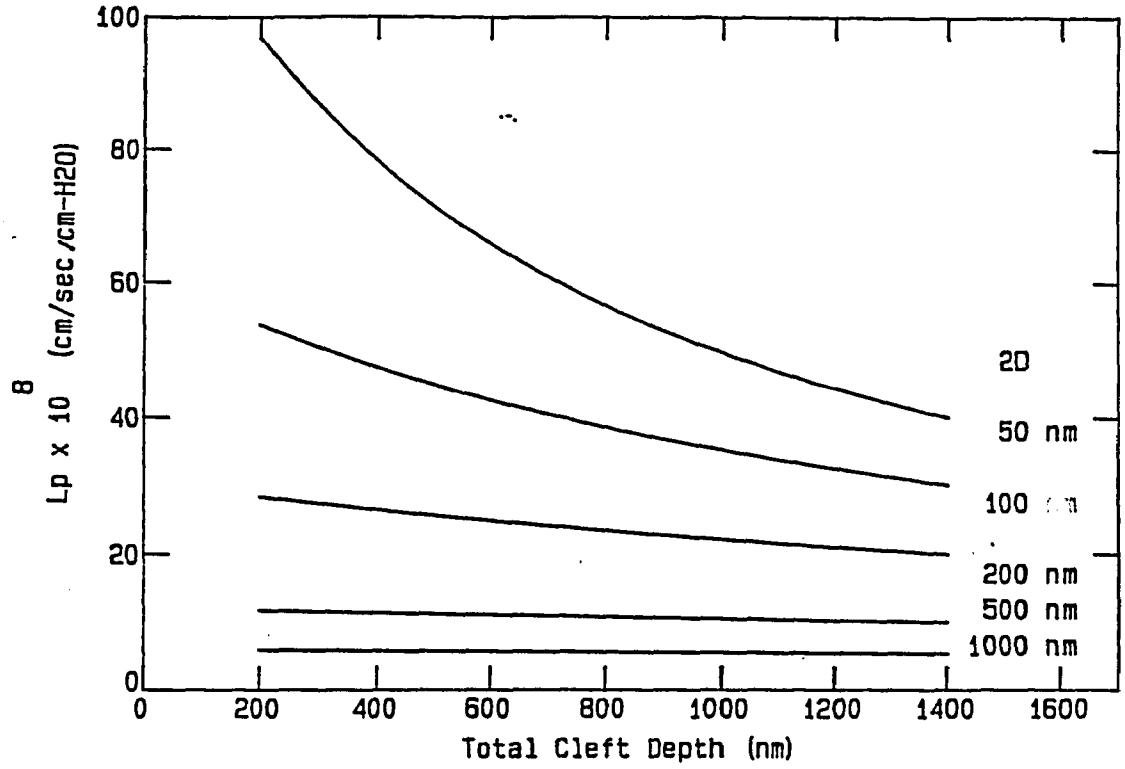

Fig.2.5: Effect of cleft depth. The variation of L_p with cleft depth L is examined for pore spacing 2D of 50, 100, 200, 500 and 1000 nm. The most common capillary cleft depths for different tissues range from 700 nm for frog mesentery to 1400 nm for mammalial adult lung. Pore radius is 5.5 nm and $L_2 = 2r_p = 11$ nm (single strand).

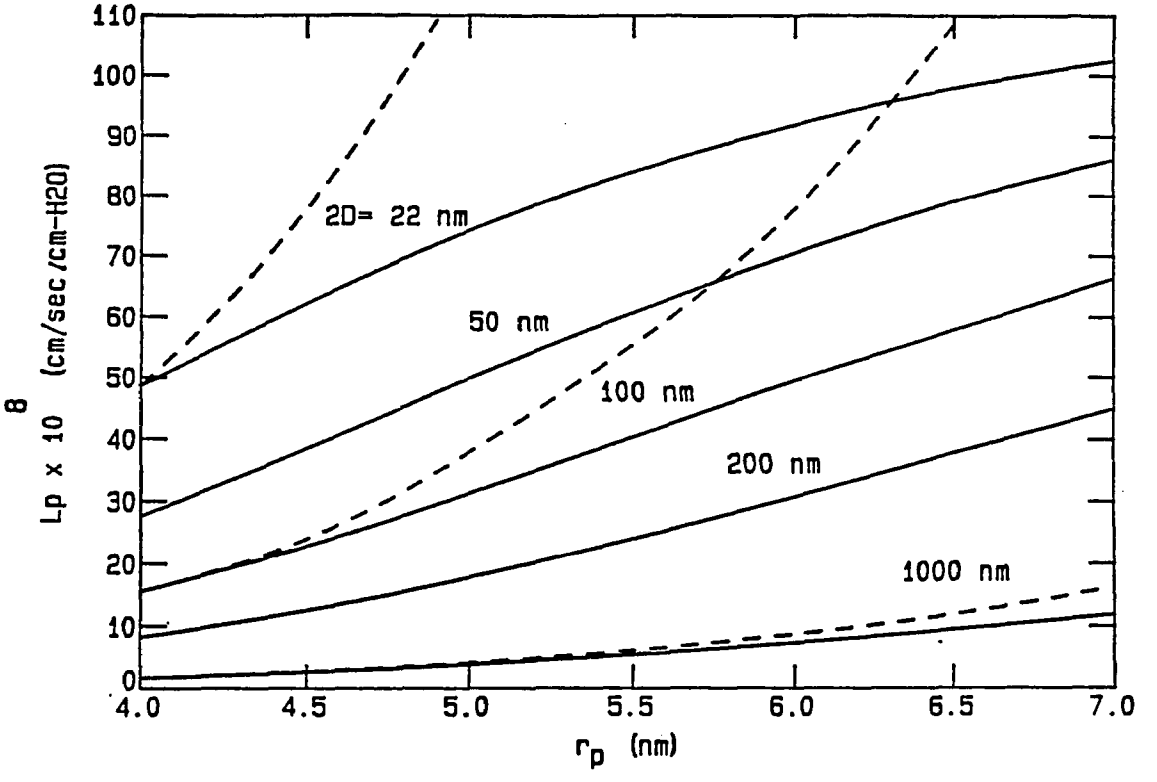

Fig.2.6: Effect of pore diameter. The variation of L_p with pore radius r_p is examined for 2D of 22, 50, 100, 200 and 1000 nm. Dashed lines show the results of traditional cylindrical pore theory in which L_p increases in proportion to r_p^4. The total cleft depth L is 700 nm $L_2 = 2r_p = 11$ nm (single strand).

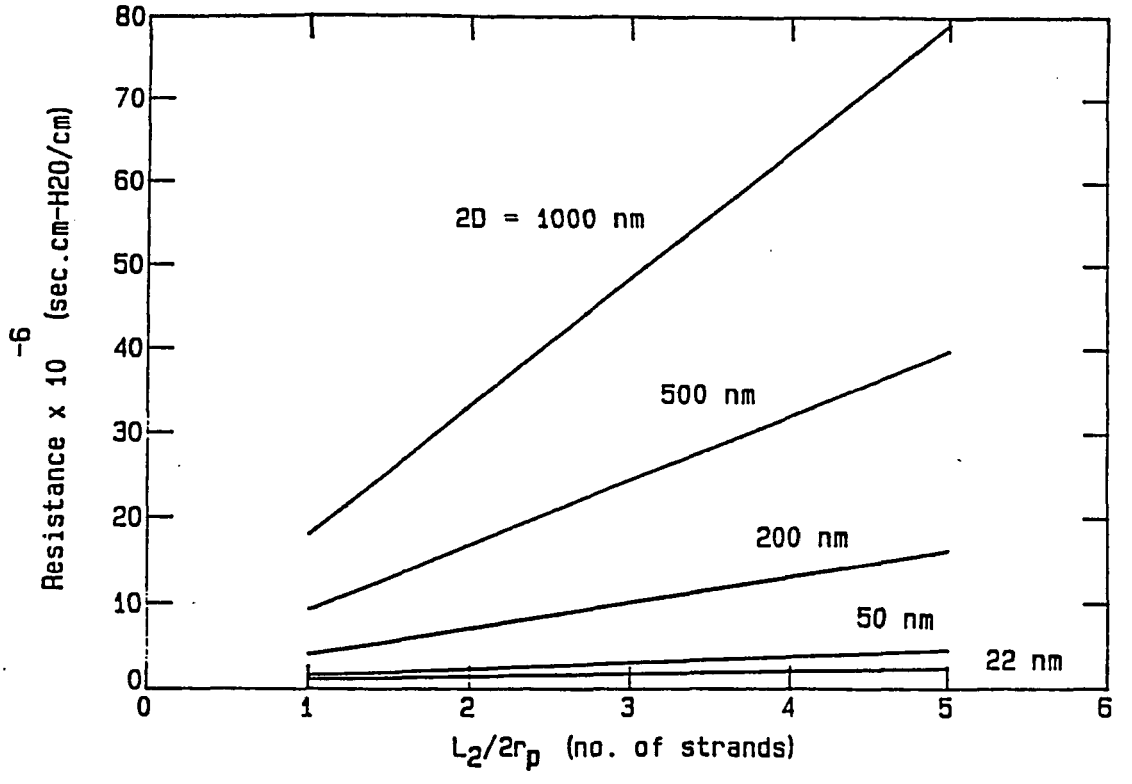

Fig.2.7: Effect of pore length (number of protein strands in series). The figure shows the linear relation between the total hydraulic resistance and number of protein strands ($L_2/2r_p$) for five different values of pore spacing (2D). Pore radius r_p is 5.5 nm and total cleft depth L is 700 nm.

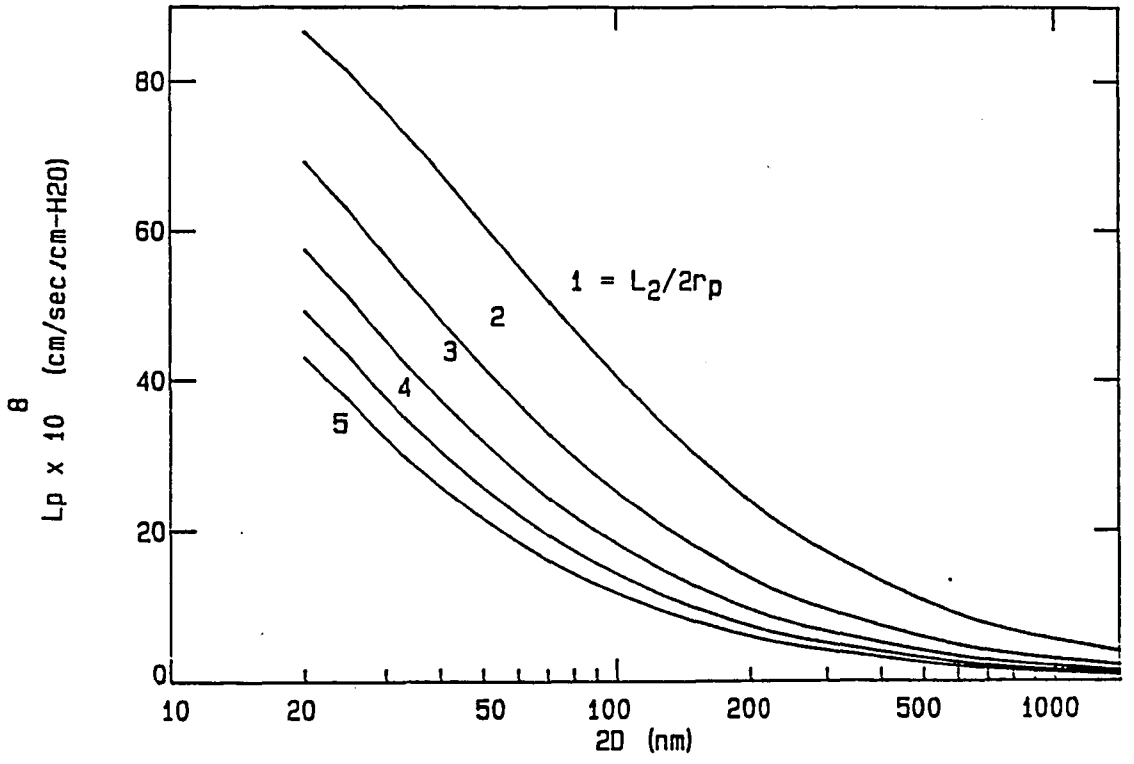

Fig.2.8: Effect of pore spacing. Hydraulic conductivity Lp for clefts with one to five protein strands ($L_2/2r_p$) and pore spacing (2D) between 22 and 1400 nm are shown, where 2D is plotted on the abscissa using a logarithmic scale. Pore radius r_p is 5.5 nm, cleft depth L is 700 nm.

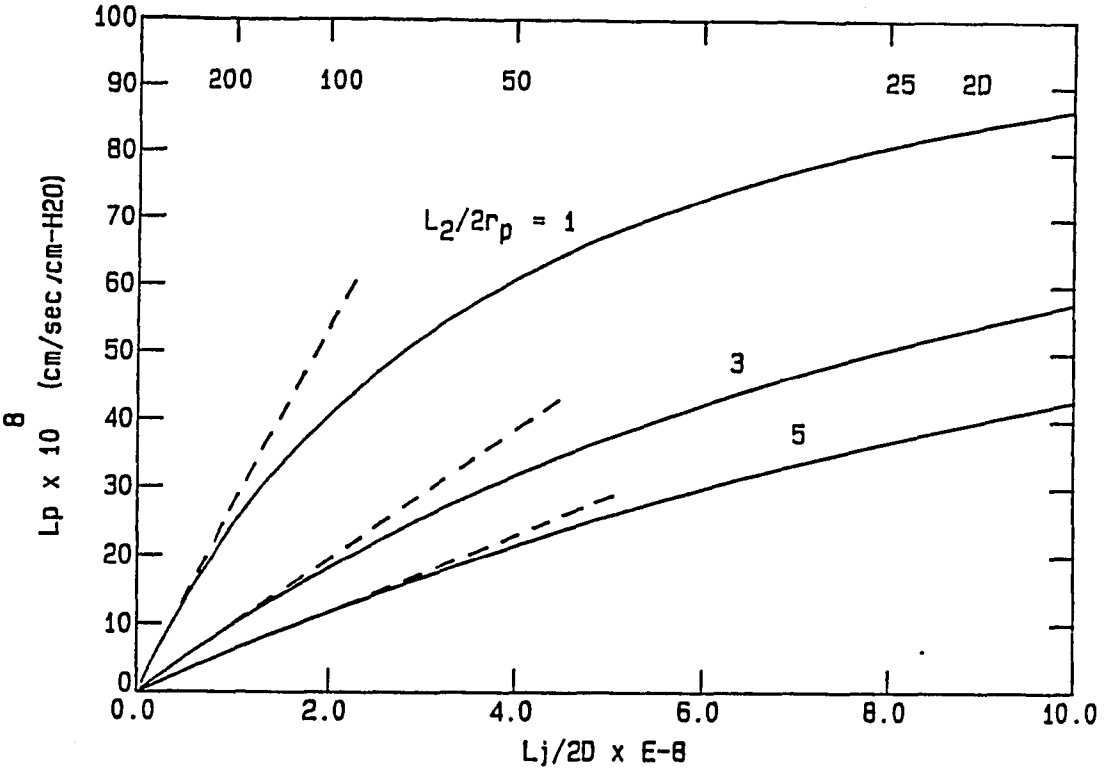

Fig.2.9: Effect of pore frequency. Hydraulic conductivity L_p is plotted as a function of pore frequency ($L_j/2D$) for clefts with one to five protein strands. $L_j/2D$ represents number of holes per cm^2 capillary surface area. $L_j/2D = 1.0 \times 10^8$ corresponds to one missing protein in 20 when $L_j = 2000$ cm/cm^2 of capillary surface area. Dashed line shows the linear relation that is valid only for small pore frequencies.

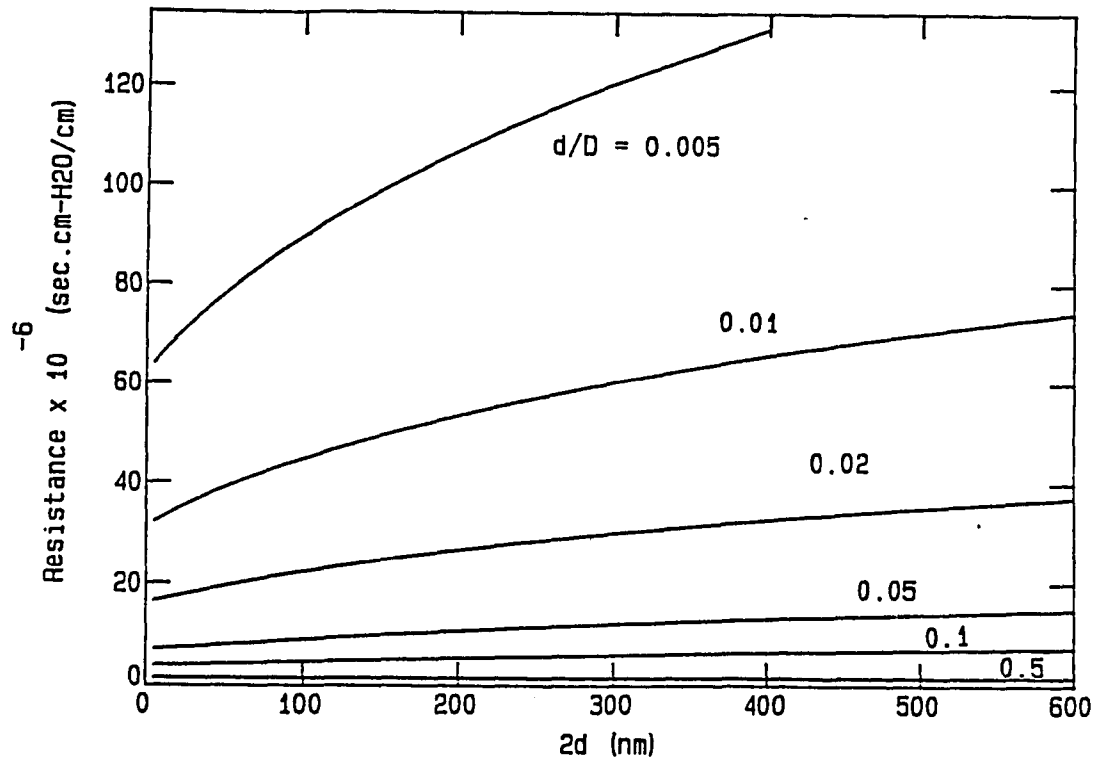

Fig.2.10: Effect of junction slit length. The variation of the hydraulic resistance $1/L_p$ with slit length 2d is shown for different fractional lengths of open junction, d/D = 0.005, 0.01, 0.02, 0.05, 0.1 and 0.5. The width of the tight portion of the slit is 6 nm and depth is 11 nm. The width of the wide portion is 17 nm and total cleft depth is 700 nm. The slit length ranges from 5.6 to 600 nm, which covers small gaps formed by individual missing proteins in present model and long slits of 500 nm length as suggested by Casley-Smith *et al.* (1975).

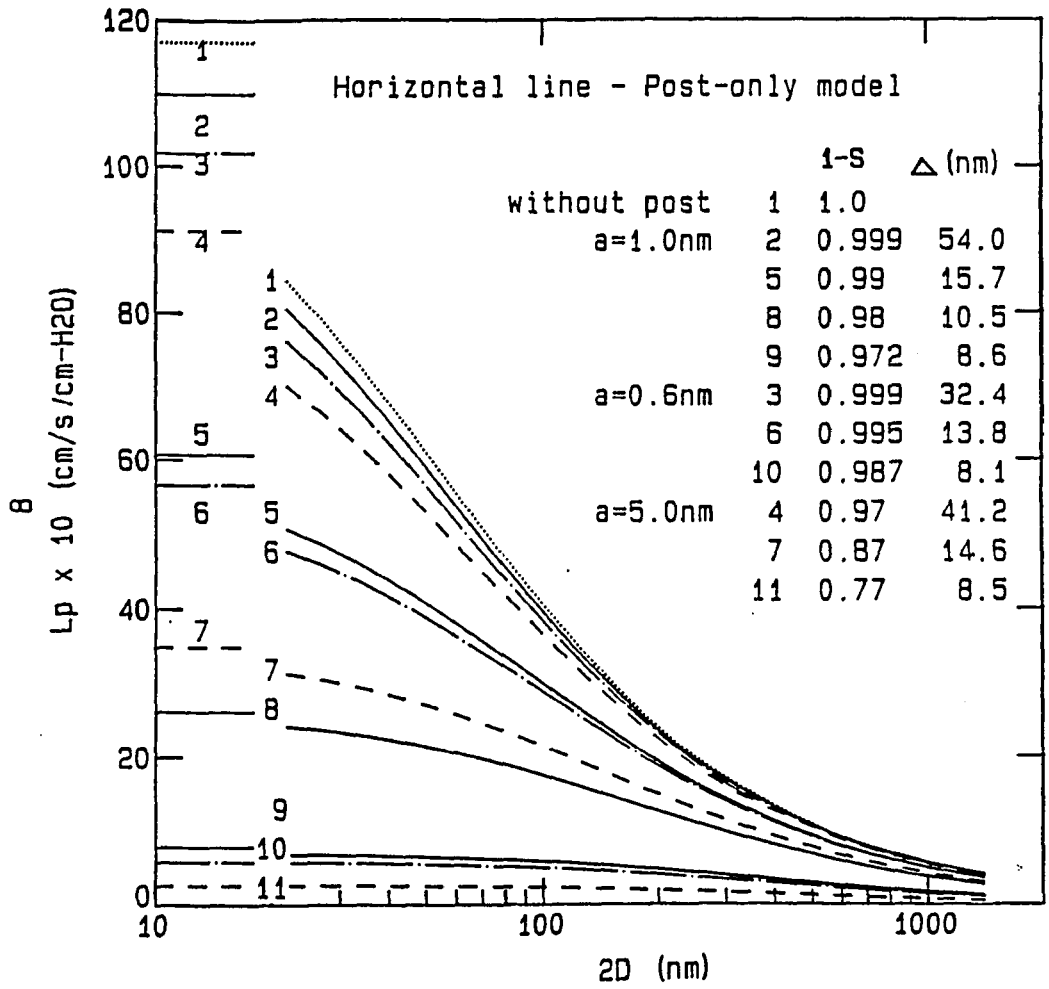

Fig.2.11: Effect of cross-linking molecules. Hydraulic conductivity L_p for clefts with cross-linking molecules (posts) only (horizontal lines) and for clefts with tight junction strands and linking molecules within the wide portion are shown for three different post radii, a=0.6, 1 and 5 nm, and different void fractions 1-S. $\Delta = \sqrt{2}w - 2a$ is the open space between two posts. Results show that the hydraulic conductivity depends primarily on the open space Δ and not the post radius.

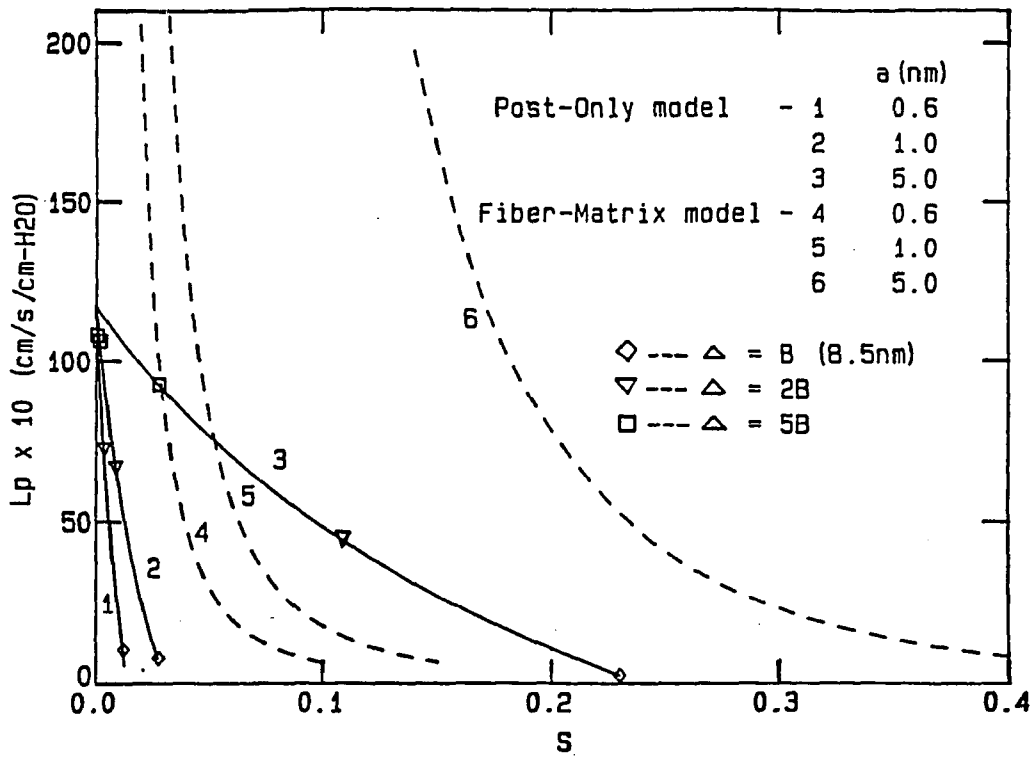

Fig.2.12: Effect of solidity ratio S of cross-linking molecules. Hydraulic conductivity L_p for clefts without tight junction strands are shown for three different post radii. Solid lines show the results of the hydrodynamic theory developed herein and dashed lines show the results of Carmen-Kozeny approximation used by Curry (1986) in his fiber-matrix model.

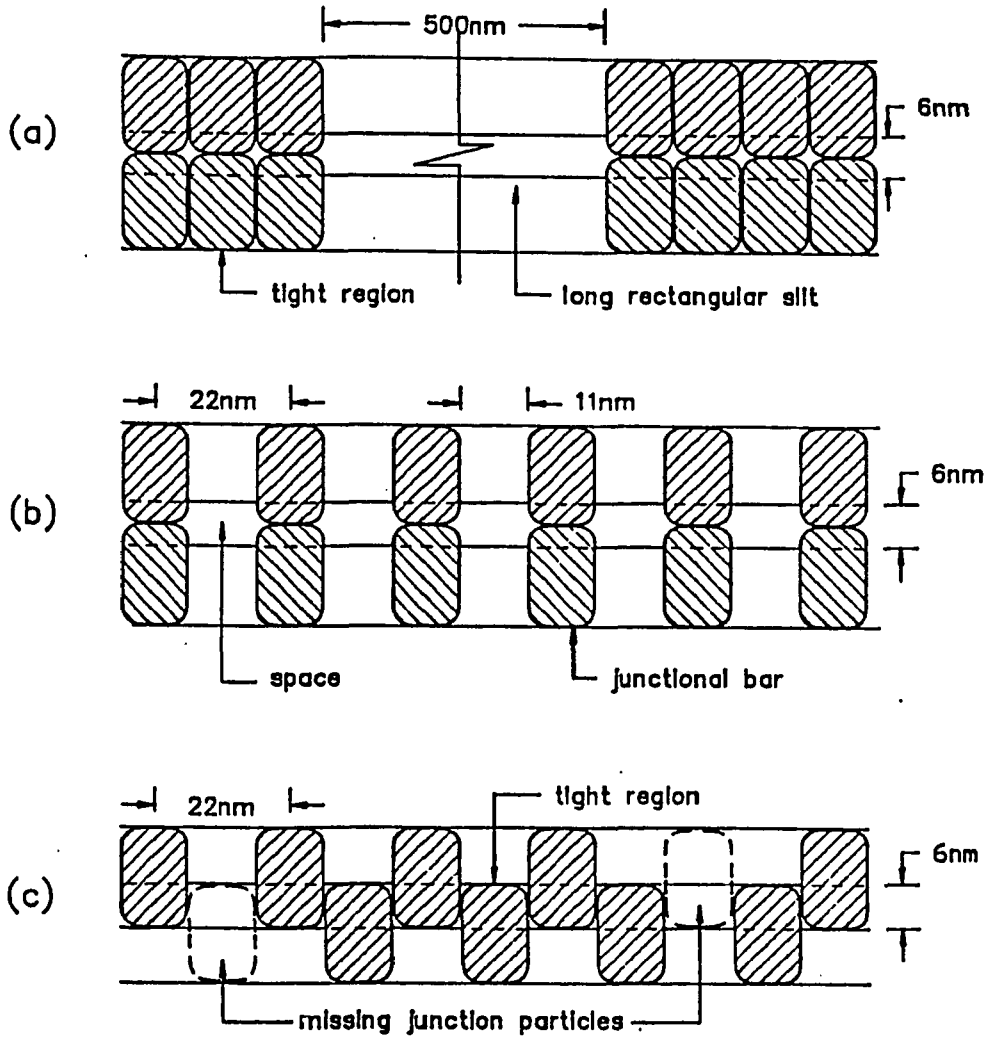

Fig.2.13:Three alternative views of pores in junctional protein strands. (a) Long rectangular slit model, Casley-Smith *et al.* (1975). (b) Alternating space and junctional bar model, Firth *et al.* (1983). (c) Interacting pore-missing junction particle model, this study.

CHAPTER III

A NEW ANALYSIS of FIBER-MATRIX THEORY for CAPILLARY TRANSPORT

3.1 Introduction

The endothelial clefts are believed to be the principal pathway for the transcapillary movement of water and small solutes (Curry 1984,1986; Michel 1985). The intercellular clefts between adjacent membranes of vascular endothelial cells are narrow channels of typically 17-25 nm gap height, whose depth (length along channel midplane) can vary from 400 nm for capillaries to 2000 nm for arterial endothelium. Except for localized constrictions associated with intramembranous junction protein arrays, the gap height between membranes is of remarkable uniformity. The inability of a simple parallel or constricted channel geometry to explain the large body of existing data on capillary permeability has led Curry & Michel (1980) to propose that a fiber matrix in the wide part of the cleft, as opposed to the junctional constrictions, serves as the primary molecular sieve for larger solute molecules. Experiments (Luft 1966) indicate that glycocalyx fibers exist on the luminal surface of the endothelial cell surface which might extend into the wide portion of the cleft. The proteoglycan fiber is approximately 0.6nm in radius. The fiber matrix model, because of its greater flexibility, seems to be able to account for the major discrepancies in the predicted results for various membrane coefficients. However, rough estimates of the filtration resistance of an ordered fiber array (Tsay *et al.*, 1989) based on the two term asymptotic solution in Lee (1969) have

suggested that the Carmen-Kozeny equation, used in the fiber matrix model to describe the flow through the cross-bridging matrix, may be totally inappropriate since it describes an infinite matrix and neglects the hydrodynamic interaction between the fibers and the channel walls, which is the dominant effect in the dilute fiber limit.

The aspect ratio B based on the dimensions cited is about 18 (B'=22nm, a=0.6nm). Estimates of the typical spacing Δ' between fibers for them to serve as the molecular filter lie in the range, 6 to 10 nm. Thus both the value of B and Δ/B lie considerably outside the range of validity of the approximate theory in Lee (1969) for a cross-bridging periodic fiber array. The periodic fiber structure is also of interest in another context. Silberberg (1987) and Firth (1983) have proposed that the uniformity of spacing may be due to a small volume fraction of cross-bridging proteins that span the channel. The aspect ratio of these larger cross-bridging molecules is 2 to 3 and thus similar to the septal posts in lung alveoli. Results will be presented herein to examine the feasibility of both these cross-bridging molecular networks.

In the fiber matrix model, the solute diffusivity is described by a stochastic model for an unbounded random fibrous network (Ogston *et al.* 1973). Using a statistical model for a random fiber density distribution, this theory takes account of the steric exclusion of the particles and introduces a collision mean free path to take account of the interaction of the solute with the matrix fibers. However, the theory does not consider the hydrodynamic interaction of the solute molecule with the disturbance velocity field of the matrix. In the present study, new analyses for the hydraulic and diffusive resistance of a cross-bridging fiber matrix will be developed for both periodic and random arrays.

The hydrodynamic interaction of the cross-bridging fibers in the wide portion of the cleft can be treated by solving the boundary value

problem for the viscous flow in a parallel walled channel with perpendicular cylindrical fibers. This problem has attracted considerable attention since Hele-Shaw in 1898 first observed that the streamlines for this flow accurately reproduces the lines of force around a metal cylinder in a dielectric medium in a magnetic field. This behavior was then explained by Stokes who mathematically showed that if the spacing between the walls 2B' was small compared to the diameter 2a of the cylinder, the vertical component of the velocity could be neglected and the governing equation for the viscous flow in planes parallel to the boundaries was a potential flow equation. This equation could be satisfied everywhere except in a thin boundary layer region near the cylinder surface where the no slip conditions could not be satisfied. Using perturbation theory and matched asymptotic expansions Thompson (1968) was able to show for $B=B'/a \ll 1$ there was a small layer near the cylinder of thickness $O(B')$ where the vertical velocity did not vanish and the neglected viscous terms were required to satisfy the boundary conditions.

A major advance in the analysis of the above problem was then developed by Lee and Fung (1969), who wished to treat the more complicated problem where the aspect ratio of the cylinders B was of O(1). The motivation for this study was the flow of blood around the septal posts in pulmonary alveoli where the aspect ratio of the posts was typically two. An accurate infinite series solution to the three-dimensional Stokes equation for the flow past a single circular cylinder was developed and numerical results based on a truncated series were calculated for aspect ratios $B \leq 5$. An approximate two term solution was also presented which neglected the vertical velocity component and approximately satisfied the no slip conditions on the cylinder provided $B \leq 1$. However, for B=5 the error in the no slip condition on the cylinder surface at the midplane for the two term approximation was nearly 50 percent. This two term approximation was

then applied by Lee (1969) for a two-dimensional periodic array of circular cylinders as a model for the septal posts in alveolar sheet flow. The two term approximate theory in Lee (1969) also broke down if the spacing between the cylinder surfaces Δ' was comparable with or smaller than the channel height $2B'$.

In the present study a more general analysis of the channel flow problem for the doubly periodic array of cylinders is undertaken which expands the solution approach developed in Lee and Fung (1969) and Lee (1969). In particular, we are interested in the flow in a parallel walled channel in which the aspect ratio of the cylinders covers the entire range from $B \leq 1$ to $B \gg 1$ and solidity ratios where $\Delta/2B \leq O(1)$. In the limit where $\Delta/2B \ll 1$ this theory should approach the large body of solutions for the two-dimensional viscous flow past a doubly periodic array of infinite cylinders (Kuwabara 1959, Happel 1959, Spielman & Goren 1969, Sangani & Acrivos 1982 and Drummond & Tahir 1984). The principal simplification in Lee and Fung (1969) for the flow past a single cylinder is that the outer potential flow is a uniform Poiseuille flow at infinity. In this limit the upstream flow for the velocity potential in planes parallel to the boundaries has a simple $\sin\theta$ dependence in cylindrical coordinates. For an array of cylinders, an infinite series of higher order harmonic functions in θ are required and solutions which accurately satisfy the no slip conditions for all three velocity components on the surface of the cylinders are sought. The new solutions describe the transition in behavior from the irrotational Hele-Shaw potential flow limit to the two-dimensional limiting behavior for $B \gg 1$ described above. This change in behavior arises strictly from the geometric length scales in the problem and should not be confused with the more common viscous-inviscid interaction associated with traditional boundary layers that scale with the Reynolds number.

Low Reynolds number flows in pores or channels filled with a porous matrix of fibrous material have frequently been approximated using a Brinkman equation (Brinkman, 1947; Bird *et al.* 1960; Neale & Nader, 1974). A summary of these applications is given in Ethier and Kamm (1989), who have used this Brinkman approach to model flow through gel filled channels. In the Brinkman equation the effect of the fiber matrix is represented by a distributed body force based on Darcy's law for an infinite medium. It is well recognized that the applicability of the equation requires that the microscopic internal length scale of the medium (spacing between fibers) be small compared to the characteristic distance over which the macroscopic average velocity and pressure varies. Larson and Higdon (1986) using detailed numerical calculations have shown that the Brinkman approach is a good approximation for shear flow over an isotropic fiber matrix. There is to our knowledge no previous model for examining the validity and limitations of the Brinkman equation for approximating bounded porous media flows. In particular, one wishes to study the behavior of the Brinkman equation as the fiber spacing is varied relative to the characteristic macroscopic length, the channel height.

Because the solutions obtained from Lee (1969) and Sangani & Acrivos (1982) provide good approximations for the two limiting cases, the irrotational Hele-Shaw potential flow and the two-dimensional flow, an accurate interpolation formula for the drag coefficient is also developed. This formula is superior to the Brinkman approximation for a periodic fiber array in which $B \leq O(1)$.

The fundamental solution for the hydrodynamic drag on a finite sphere in a channel without fibers is given in Ganatos *et al.* (1980). A rigorous treatment of the additional resistance due to the presence of the fibers would required a solution that satisfies no slip conditions on the surface of the sphere and all the surrounding fibers. A reasonable approximation to this shielding behavior for the

high aspect ratio fibers of current interest is suggested by the excellent approximation provided by the Brinkman equation when $B'/a \geq 5$. An exact solution of the Brinkman equation which satisfies the no slip conditions of the channel walls and the solute is beyond the scope of the present investigation. However, a very good approximation can be obtained by combining the solution in Ganatos *et al.* (1980) for a bounded sphere and the known solution for a sphere in an unbounded Brinkman medium. The solution for an unbounded Brinkman sphere is given in the original theory of Brinkman (1947). The Brinkman correction to the Stokes drag on a sphere examines the solute-fiber interaction only. The steric exclusion will be also be taken into account by solving the pure conduction problem for the periodic array or applying the statistical theory for the random array. Several studies have been performed to examine the effective conductivity of two dimensional periodic arrays. Keller & Sachs (1964) solved the effective thermal conductivity for a square array of perfectly conducting cylinders by using finite difference method. Perrins et al. (1979) studied the pure diffusion problem using Rayleigh's method for aligned cylinders in square and hexagonal arrays. In the present study, a linear combination of Weierstrass zeta function and its derivatives is used to express the solution of this problem.

This chapter is presented in four sections. The rigorous hydrodynamic theory for the periodic array, the Brinkman approximation for the random fiber array, and the new approximate solutions for the solute diffusivity in a periodic or random fiber array are developed in section 2. Section 3 presents and discusses the numerical results. A summary is given in section 4.

3.2 Hydrodynamic Theories

3.2.1 Hydraulic Resistance Across Periodic Fiber Array

For flow through a fiber matrix confined between two parallel plates, Fung & Sobin (1968) have defined the following "macroscopic" relationship between the pressure gradient and the fluid velocity :

$$\nabla' \bar{P}' = -(3 \mu_{eff}/B'^2) \bar{U} \qquad (3.1)$$

where the prime indicates dimensional co-ordinates, the overbar denotes an average value over a region which is small compared with the macroscopic length scale, yet is large enough to level off the microscopic heterogeneity. For a periodic fiber arrangement, the average is taken over one periodic unit. The effective viscosity μ_{eff} equals μf, where f represents the influence of the fibers. In general f is a function of the configuration of the fiber array, the fiber volume fraction S and the aspect ratio B. To determine f one must first obtain a solution for the local flow field in the periodic unit. The contribution to f arises from two sources, the resistance of the fibers and the increased resistance of the wall due to the velocity disturbance generated by the fiber-wall interaction.

(a) Formulation

It is convenient to formulate the problem in terms of dimensionless co-ordinates. In the following, all the lengths are scaled relative to the fiber radius a. The fluid velocity $\vec{V}$ is made dimensionless with respect to the superficial velocity $\bar{U}$ and the fluid pressure P with respect to a characteristic viscous stress $\mu\bar{U}/a$. An idealized configuration of the intercellular cross-bridging fiber array is shown in Figure 3.1. This structure is similar to the internal geometry of the pulmonary alveolar septa proposed by Lee (1969). Let (x,y,z) be a set of Cartesian coordinates and (r,θ,z) be a set of cylindrical coordinates. These two sets of coordinates have the same origin. Let (α,β) designate a particular fiber in the periodic array. The center of the $\alpha\beta$th fiber is located at $Z_{\alpha\beta}$, where

Z is a complex plane with $Z=x+iy=re^{i\theta}$ and $Z_{\alpha\beta}=2\alpha\bar{\omega}_1+2\beta\bar{\omega}_2=R_{\alpha\beta}\exp(i\psi_{\alpha\beta})$. Here $2\bar{\omega}_1=\omega_1-i\omega_2$, $\bar{\omega}_2=\omega_1+i\omega_2$, and $\omega_1=\omega_2=W/2$ for a square array. $(r_{\alpha\beta},\theta_{\alpha\beta},z)$ are the local coordinates corresponding to the $\alpha\beta$th fiber.

For an incompressible creeping flow, the non-dimensionalized continuity equation and Stokes equation are

$$\nabla.\vec{V}=0 \tag{3.2}$$

$$\nabla^2\vec{V}=\nabla P \tag{3.3}$$

The fluid velocity $\vec{V}$ must satisfy the no-slip conditions on the surfaces of the fibers and the channel walls

$$\vec{V}=0 \qquad \text{at} \quad r_{\alpha\beta}=1 \tag{3.4}$$

$$\vec{V}=0 \qquad \text{at} \quad z=\pm B \tag{3.5}$$

and the total flux Q is given by

$$\frac{Q}{2B'W'\bar{U}}=1-\frac{1}{2BW}\int_{-B}^{+B}\int_{1}^{W-1} v_\theta(\theta=\tfrac{\pi}{2})\,dr\,dz \tag{3.6}$$

Using equations (3.2) and (3.3), one can show that P is a harmonic function and the components of $\vec{V}$ are biharmonic functions.

(b) General Solution for Stokes Flow Confined Between Two Flat Plates

A general solution of equation (3.2) and (3.3) in cylindrical coordinates which satisfies the no-slip conditions on the two channel walls is given by Lee & Fung (1969) as

$$P = -\frac{2}{B}\left\{\frac{\phi_0}{B} + \mathrm{Re}\left[\sum_{n=1}^{\infty}\phi_n \frac{\cos\alpha_n z}{\cos\alpha_n B}\right]\right\} \tag{3.7}$$

$$v_r = -\left(\frac{1}{r}\frac{\partial\psi_0}{\partial\theta}\right)\left(1 - \frac{z^2}{B^2}\right) - \mathrm{Re}\left[\sum_{n=1}^{\infty}\frac{1}{\alpha_n^2}\left(\frac{\partial\phi_n}{\partial r}\right)\left(\frac{dq_n}{dz}\right)\right] - \sum_{n=0}^{\infty}\left(\frac{1}{r}\frac{\partial\bar{\psi}_n}{\partial\theta}\right)\cos\lambda_n z \tag{3.8}$$

$$v_\theta = -\left(\frac{\partial\psi_0}{\partial r}\right)\left(1 - \frac{z^2}{B^2}\right) - \mathrm{Re}\left[\sum_{n=1}^{\infty}\frac{1}{\alpha_n^2}\left(\frac{1}{r}\frac{\partial\phi_n}{\partial\theta}\right)\left(\frac{dq_n}{dz}\right)\right] + \sum_{n=0}^{\infty}\left(\frac{\partial\bar{\psi}_n}{\partial r}\right)\cos\lambda_n z \tag{3.9}$$

$$v_z = \mathrm{Re}\left[\sum_{n=1}^{\infty}\phi_n q_n\right] \tag{3.10}$$

where

$$q_n(z) = \left(\frac{\sin\alpha_n z}{\sin\alpha_n B}\right) - \left(\frac{z\cos\alpha_n z}{B\cos\alpha_n B}\right). \tag{3.11}$$

α_n and λ_n are eigenvalues which satisfy the following equations:

$$\sin 2\alpha_n B = 2\alpha_n B \tag{3.12}$$

$$\lambda_n = (2n+1)\frac{\pi}{2B} \qquad n = 0,1,2,\ldots\ldots \tag{3.13}$$

Here all the eigenvalues α_n are complex except $\alpha_0=0$. Approximate values for α_n are given by the equation $2\alpha_n B = (2n+\frac{1}{2})\pi \pm i\ \ln[(4n+1)\pi]$, $n=1,2,3,\ldots$. The eigenfunctions ϕ_0, ψ_0, ϕ_n, and $\bar{\psi}_n$ satisfy the following differential equations:

$$E^2\psi_0 = 0, \qquad E^2\phi_0 = 0, \tag{3.14}$$

$$E^2\phi_n - \alpha_n^2\phi_n = 0, \quad n=1,2,\ldots\ldots \tag{3.15}$$

$$E^2\bar{\psi}_n - \lambda_n^2\bar{\psi}_n = 0, \quad n=0,1,2,\ldots\ldots \tag{3.16}$$

where

$$E^2 = \frac{\partial^2}{\partial r^2} + \frac{1}{r}\frac{\partial}{\partial r} + \frac{1}{r^2}\frac{\partial^2}{\partial \theta^2} .$$

The fundamental solutions given by equation (3.7) through (3.10) are a superposition of three contributions: the terms containing ϕ_0 and ψ_0 are the zero eigenvalue biharmonic solutions for α_0=0, which correspond to the irrotational Hele-Shaw flow; the terms containing ϕ_n with n≥1 are biharmonic solutions, which describe the vertical component of the velocity in the z-direction induced by the motion of vorticity layer past the fibers inside the channel; the terms containing $\tilde{\psi}_n$ are the rotational harmonic solutions, which are required to satisfy the no slip boundary condition on the surface of each fiber. The $\tilde{\psi}_n$ harmonic solutions do not contribute to the pressure field, whereas the ϕ_n solutions do not contribute to the z component of the vorticity.

The solution of equations (3.14) - (3.16) can be obtained by separation of variables. These separable solutions are:

$$\begin{aligned}
&\phi_0,\ \psi_0: \quad r^{-m}\cos m\theta,\ r^{-m}\sin m\theta,\ r^{m}\cos m\theta,\ r^{m}\sin m\theta \\
&\phi_n: \quad K_m(\alpha_n r)\cos m\theta,\ K_m(\alpha_n r)\sin m\theta,\ I_m(\alpha_n r)\cos m\theta,\ I_m(\alpha_n r)\sin m\theta, \\
&\tilde{\psi}_n: \quad K_m(\lambda_n r)\cos m\theta,\ K_m(\lambda_n r)\sin m\theta,\ I_m(\lambda_n r)\cos m\theta,\ I_m(\lambda_n r)\sin m\theta,
\end{aligned} \tag{3.17}$$

where I_m and K_m are modified Bessel functions of the first and second kind of order m. The functions ϕ_0, ψ_0, ϕ_n, and $\tilde{\psi}_n$ are linear combinations of these separable solutions. For flow around a single fiber, Lee & Fung (1969) showed that the m=1 terms are sufficient to provide a complete solution. However, for flow through a fiber array, the problem is considerably more complicated since an infinite series of terms with m>1 are required in the solutions for ϕ_0, ψ_0, ϕ_n and $\tilde{\psi}_n$ to describe the interaction between the fibers.

(c) Stokes Flow Past A Square Array of Cylindrical Fibers Inside A

Channel

Some of the separable solutions in equation (3.17) can be eliminated by applying the boundary condition at $r \to \infty$. Since the flow field is bounded everywhere, the terms including r^m $(m>1)$, $I_m(\alpha_n r)$, and $I_m(\lambda_n r)$ for $(m\geq 0)$ must be excluded. The fundamental solutions for ϕ_n and $\bar{\psi}_n$ thus reduce to the more limited set

$$\phi_n: \quad K_m(\alpha_n r_{\alpha\beta})\cos m\theta_{\alpha\beta},\ K_m(\alpha_n r_{\alpha\beta})\sin m\theta_{\alpha\beta} \tag{3.18}$$

$$\bar{\psi}_n: \quad K_m(\lambda_n r_{\alpha\beta})\cos m\theta_{\alpha\beta},\ K_m(\lambda_n r_{\alpha\beta})\sin m\theta_{\alpha\beta}. \tag{3.19}$$

The doubly periodic functions for ϕ_n and ψ_n can be obtained by summing the functions in (3.18) and (3.19) over all possible α,β. Similarly, one could construct the quasi-doubly periodic functions for ϕ_0 and ψ_0 by summing terms involving r^{-m} $(m\geq -1)$ over α,β. However, since ϕ_0 and ψ_0 are harmonic functions corresponding to the irrotational Hele-Shaw flow, a simpler alternative is to take advantage of the periodicity properties of the Weierstrass zeta function $\zeta(Z)$ as proposed earlier in Lee (1969).

According to the Cauchy-Reiman theorem, one knows that there is a function Φ of the complex variable Z which satisfies

$$\Phi(Z) = \phi_0 + i\psi_0. \tag{3.20}$$

The function $\Phi(Z)$, which is an integral of an elliptic function for a doubly periodic fiber array, can be expressed as a linear combination of Weierstrass zeta function $\zeta(Z)$ and its derivatives (Whittaker 1944, Lee 1969).

$$\Phi(Z) = b_0 Z + \sum_{m=1}^{\infty} b_n \zeta^{(m)}(Z)\ , \tag{3.21}$$

where

$$\zeta(Z) = \frac{1}{Z} + {}_{\alpha,\beta}\Sigma'\left\{\frac{1}{(Z-Z_{\alpha\beta})} + \frac{1}{Z_{\alpha\beta}} + \frac{Z}{Z_{\alpha\beta}^2}\right\} \tag{3.22}$$

$$\zeta(Z)^{(m)} = \frac{(-1)^m}{m!}\left(\frac{d^m\zeta}{dZ^m}\right) \tag{3.23}$$

The symbol ${}_{\alpha,\beta}\Sigma'$ is used to denote the summation over all α,β with the exception of the origin $\alpha=\beta=0$. The function $\zeta(Z)$ is a quasi-periodic function:

$$\zeta(Z+2\alpha\tilde{\omega}_1+2\beta\tilde{\omega}_2) = \zeta(Z) + 2\alpha\eta_1 + 2\beta\eta_2. \tag{3.24}$$

The derivatives of $\zeta(z)$ are doubly periodic functions with periods $2\tilde{\omega}_1$ and $2\tilde{\omega}_2$, where and $\eta_1\tilde{\omega}_2 - \eta_2\tilde{\omega}_1 = \frac{\pi}{2}i$. Using symmetry conditions at the x and y axes, terms involving $\zeta^{(2m-1)}$, $K_{2m}(\alpha_n r_{\alpha\beta})\cos 2m\theta_{\alpha\beta}$, $K_m(\alpha_n r_{\alpha\beta})\sin m\theta_{\alpha\beta}$, $K_m(\lambda_n r_{\alpha\beta})\cos m\theta_{\alpha\beta}$, $K_{2m}(\lambda_n r_{\alpha\beta})\sin 2m\theta_{\alpha\beta}$ in equations (3.18), (3.19), and (3.21) must vanish. This leads to the following expressions for $\Phi(Z)$, ϕ_n and ψ_n,

$$\Phi(Z) = b_0 Z + \sum_{m=1}^{\infty} b_n \zeta^{(2m-2)}(Z) \ ,$$

$$\phi_n = \sum_{m=1}^{\infty} d_{nm}\left[K_{2m-1}(\alpha_n r)\cos(2m-1)\theta + {}_{\alpha,\beta}\Sigma' K_{2m-1}(\alpha_n r_{\alpha\beta})\cos(2m-1)\theta_{\alpha\beta}\right] \tag{3.25}$$

$$\psi_n = \sum_{m=1}^{\infty} c_{nm}\left[K_{2m-1}(\lambda_n r)\sin(2m-1)\theta + {}_{\alpha,\beta}\Sigma' K_{2m-1}(\lambda_n r_{\alpha\beta})\sin(2m-1)\theta_{\alpha\beta}\right]$$

Substituting equation (3.25) into equations (3.7) to (3.10), one has a general solution for a doubly periodic flow field.

In order to apply the no-slip conditions on the surfaces of the fibers, we need to transform the $(r_{\alpha\beta}, \theta_{\alpha\beta}, z)$ coordinates in equation (3.25) into a common coordinate system (r,θ,z). The Weierstrass zeta

function and its derivatives are transformed according to the binomial theorem

$$\frac{1}{(Z-Z_{\alpha\beta})^m} = \sum_{p=0}^{\infty} \frac{(m+p-1)!}{p!(m-1)!} \frac{(-1)^m Z^p}{Z_{\alpha\beta}^{(m+p)}} . \tag{3.26}$$

The transformation of the modified Bessel functions can be performed using Graf's generalization of Neumann's addition theorem (Watson 1980).

$$K_m(\alpha r_{\alpha\beta}) \begin{matrix} \sin(m\theta_{\alpha\beta}) \\ \cos(m\theta_{\alpha\beta}) \end{matrix} = \sum_{p=-\infty}^{\infty} K_{m+p}(\alpha R_{\alpha\beta}) I_p(\alpha r) \begin{matrix} \sin(p\theta-(m+p)\psi_{\alpha\beta}) \\ \cos(p\theta-(m+p)\psi_{\alpha\beta}) \end{matrix} \tag{3.27}$$

Both of these transformations converge when $|Z|<|Z_{\alpha\beta}|$. After the transformation, equation (3.25) becomes

$$\psi_0 = -b_0[r\sin\theta + \sum_{m=1}^{\infty} \frac{\sin(2m-1)\theta}{2m-1}(b_m r^{-(2m-1)} + \sum_{p=1}^{\infty} A_{mp} b_p r^{(2m-1)})]$$

$$\psi_n = -\frac{b_0}{\lambda_n} \sum_{m=1}^{\infty} \sin(2m-1)\theta \left[c_{nm} \frac{K_{2m-1}(\lambda_n r)}{K_{2m-1}(\lambda_n)} + \sum_{p=1}^{\infty} B_{nmp} c_{np} \frac{I_{2m-1}(\lambda_n r)}{I_{2m-1}(\lambda_n)}\right] \tag{3.28}$$

$$\phi_n = -\frac{b_0}{\alpha_n} \sum_{m=1}^{\infty} \cos(2m-1)\theta \left[d_{nm} \frac{K_{2m-1}(\alpha_n r)}{K_{2m-1}(\alpha_n)} - \sum_{p=1}^{\infty} D_{nmp} d_{np} \frac{I_{2m-1}(\alpha_n r)}{I_{2m-1}(\alpha_n)}\right]$$

where

$$A_{11} = 0,$$

$$A_{mp} = \frac{(2m+2p-3)!}{(2m-2)!\ (2p-1)!} \sum_{\alpha,\beta}'' G_{\alpha\beta} \frac{\cos(2m+2p-2)\psi_{\alpha\beta}}{R_{\alpha\beta}^{(2m+2p-2)}}$$

$$B_{nmp} = \frac{I_{2m-1}(\lambda_n)}{K_{2p-1}(\lambda_n)} \sum_{\alpha,\beta}'' G_{\alpha\beta} [K_{2m+2p-2}(\lambda_n R_{\alpha\beta})\cos(2m+2p-2)\psi_{\alpha\beta} - K_{2m-2p}(\lambda_n R_{\alpha\beta})\cos(2m-2p)\psi_{\alpha\beta}]$$

$$D_{nmp} = \frac{I_{2m-1}(\alpha_n)}{K_{2p-1}(\alpha_n)} \; {}_{\alpha,\beta}\Sigma'' \; G_{\alpha\beta} \left[K_{2m+2p-2}(\alpha_n R_{\alpha\beta})\cos(2m+2p-2)\psi_{\alpha\beta} + K_{2m-2p}(\alpha_n R_{\alpha\beta})\cos(2m-2p)\psi_{\alpha\beta}\right].$$

and

$$G_{\alpha\beta} = 4 \quad \text{for fibers not located on the x or y-axis}$$
$$= 2 \quad \text{for fibers located on the x or y-axis}$$

The notation ${}_{\alpha,\beta}\Sigma''$ denotes a summation over all possible fiber positions in the first quadrant, except the one at the origin. Notice that according to the formula for A_{mp}, $A_{11} = {}_{\alpha,\beta}\Sigma'' \frac{\cos\psi_{\alpha\beta}}{R_{\alpha\beta}^2} = \frac{S}{\pi}\,\mathrm{Re}[e^{i\pi/2}S_2]$, where S_2 is the nonabsolutely convergent term evaluated by Rayleigh (1892) and Perrins *et al.* (1979). Since the terms involving A_{11} cancel out when ϕ_0 is transformed from equation (3.25) into equation (3.28), we have set $A_{11}=0$. Rayleigh's convergence difficulties arose from an incorrect assessment of the macroscopic boundary integral, which has been discussed in O'Brien (1979).

By substituting equation (3.28) back into (3.7) to (3.10) and applying boundary conditions (3.4) and (3.6), one should be able to obtain the unknown coefficients in equation (3.28). However, because the set of solutions in equations (3.7) to (3.10) involves three different sets of independent functions of z, the no slip condition on fiber surface can not be applied in a straight forward manner. One could attempt to satisfy the no slip conditions using numerical boundary collocation methods as described in Weinbaum *et al.* (1990). However, since this problem is three-dimensional, this would require many grid points and there is no guarantee for the convergence. One alternative way which does guarantee convergence is to expand the z dependence in each velocity component in terms of a complete set of orthogonal functions. For the v_r and v_θ velocity components, the $\cos(\lambda_n z)$ form a complete set of orthogonal functions. For the v_z

velocity component, we follow the procedure of Lee & Fung (1969) for the single fiber case and introduce the function Y_n,

$$Y_n(z) = \frac{1}{\sqrt{2}} \left[\frac{\sin\nu_n z}{\sin\nu_n B} - \frac{\sinh\nu_n z}{\sinh\nu_n B}\right] \tag{3.29}$$

where ν_n are the positive eigenvalues obtained from the following equation.

$$\tan \nu_n B = \tanh \nu_n B \tag{3.30}$$

Approximate values of ν_n are given by $(n+1/4)(\pi/B)$, $n=1,2,3,\ldots$ The function Y_n has the proper orthogonality because $Y_n(\pm B)=dY_n(\pm B)/dz=0$ and it is an odd function. The various functions of z appearing in equation (3.7)-(3.10) can now be expressed as infinite series in $\cos\lambda_n z$ or $Y_n(z)$, see Appendix.

Using the foregoing results, one can express each velocity component in equations (3.8)-(3.10) in the form of a doubly infinite series.

$$\begin{aligned} u &= \sum_{n=0}^{\infty} \sum_{m=1}^{\infty} \bar{U}_{mn}(r)\cos(2m-1)\theta \cos\lambda_n z \\ v &= \sum_{n=0}^{\infty} \sum_{m=1}^{\infty} \bar{V}_{mn}(r)\sin(2m-1)\theta \cos\lambda_n z \\ w &= \mathrm{Re}\left[\sum_{n=1}^{\infty} \sum_{m=1}^{\infty} \bar{W}_{mn}(r)\cos(2m-1)\theta \; Y_n\right] \end{aligned} \tag{3.31}$$

The expressions for $\bar{U}_{mn}$, $\bar{V}_{mn}$ and $\bar{W}_{mn}$ are given in the Appendix.

(d) Numerical Solution for Unknown Coefficients

In order to solve for the unknown coefficients in the expressions for $\bar{U}_{mn}$, $\bar{V}_{mn}$ and $\bar{W}_{mn}$ in equation (3.31), we first truncate the doubly infinite series at n=N and m=M. The truncated series is then required

to satisfy the no slip conditions on the surface of the fiber at the origin. Owing to the periodicity, this automatically satisfies the no-slip condition on all the other fibers. By applying the orthogonality of the functions Y_n, $\sin m\theta$, and $\cos m\theta$, we obtain

$$\sum_{p=1}^{M}(A_{mp}+\delta_{mp})b_p + \frac{(2m-1)}{\lambda_n l_n}\sum_{p=1}^{M}(B_{nmp}+\delta_{mp})c_{np}$$
$$- \mathrm{Re}\left[\sum_{j=1}^{N}\frac{e_{jn}}{\alpha_j^2 l_n}\sum_{p=1}^{M}(DK\alpha_{jp}\delta_{mp} - DI\alpha_{jm}D_{jmp})d_{jp}\right] = -\delta_{m1} \qquad m=1,M, \quad n=0,N$$

$$\sum_{p=1}^{M}(A_{mp}-\delta_{mp})b_p + \frac{1}{\lambda_n l_n}\sum_{p=1}^{M}(DK\lambda_{np}\delta_{mp} + DI\lambda_{nm}B_{nmp})c_{np}$$
$$- \mathrm{Re}\left[\frac{(2m-1)}{l_n}\sum_{j=1}^{N}\frac{e_{jn}}{\alpha_j^2}\sum_{p=1}^{M}(\delta_{mp} - D_{jmp})d_{jp}\right] = -\delta_{m1} \qquad m=1,M, \quad n=0,N \qquad (3.32)$$

$$\mathrm{Re}\left[\sum_{j=1}^{N}\frac{f_{jn}}{\alpha_j}\sum_{p=1}^{M}(\delta_{mp} - D_{jmp})d_{jp}\right] = 0 \qquad m=1,M, \quad n=1,N$$

Here l_n, e_{jn} and f_{jn} are given in equation (A.2) and $DK\alpha_{jm}$, $DI\alpha_{jm}$, $DK\lambda_{nm}$ and $DI\lambda_{nm}$ are defined following equation (A.5). The coefficients A_{mp}, B_{nmp} and D_{jmp} are given in equations (3.28) where the summation $\sum_{\alpha,\beta}$" is performed for a truncated prescribed value of $R_{\alpha\beta}$. The eigenvalues λ_n are obtained from equation (3.13), whereas the eigenvalues α_n and ν_n are evaluated numerically from equations (3.12) and (3.30) using Muller's method (Conte & Boor, 1980).

Equation (3.32) constitutes (3N+2)M equations, which can be solved for the (3N+2)M unknowns: b_m, c_{nm} and d_{jm} (m=1,M, n=0,N, j=1,N). The d_{jm} are complex so each d_{jm} represents two unknowns, a real and an imaginary part. Once equation (3.32) is solved by matrix algebra, all the unknowns except b_0 in equation (3.28) are known. b_0 is determined by applying the total flux condition in (3.6). This yields

$$b_0 = \frac{-3}{2(1+b_1 S\ \mathrm{Re}[g_1])} \tag{3.33}$$

where $S=2\pi/W^2$ and $g_1=i2\omega_1(\eta_2-\eta_1)/\pi$.

(e) Drag coefficient and Darcy permeability

From equation (3.1), the drag coefficient f is given by

$$f = \frac{\mu_{eff}}{\mu} = -\frac{B^2}{3}\left(\frac{\partial \bar{P}}{\partial x}\right) \tag{3.34}$$

Here the average pressure gradient $\partial\bar{P}/\partial x$ can be calculated from equation (3.7). Since the ϕ_n for $n>0$ are doubly periodic functions, only the term involving ϕ_0 will contribute to the average pressure gradient. From the definition of $\partial\bar{P}/\partial x$,

$$\begin{aligned} f &= -\frac{B^2}{3}\left(\frac{\partial \bar{P}}{\partial x}\right) = -\frac{B^2}{3}\,\frac{\langle P(Z+2\tilde{\omega}_1+2\tilde{\omega}_2)\rangle - \langle P(Z)\rangle}{W} \\ &= -\frac{2}{3}\,(1-b_1 S\ \mathrm{Re}[g_2])\ b_0 \end{aligned} \tag{3.35}$$

where $\langle\ \rangle$ denotes an average over the z-direction and $g_2=2\omega_2(\eta_1+\eta_2)/\pi$. For a square array, $g_1=g_2=1$ (Southard, 1964). Substituting equation (3.33) into equation (3.35), we have

$$f = (1-b_1 S)/(1+b_1 S) \tag{3.36}$$

where it is seen that f depends only on the lowest order coefficient b_1. The value of b_1, however, depends on the solution for all the coefficients in the truncated series.

The definition of the effective viscosity μ_{eff} given in equation (3.1) is based on a channel flow. This definition for μ_{eff} is not useful in describing the resistance of an infinitely long two-dimensional fiber array. In order to compare the transport properties

obtained from two and three dimensional theories, we apply the definition for the Darcy permeability K_p as follows:

$$K_p = -\mu \bar{U}/\nabla'\bar{P}' \tag{3.37}$$

For a channel flow, $K_p = B'^2/3f$, whereas for two-dimensional flow through a fiber array of infinite length, $K_p = W'^2/2f'_{2D}$ where $f'_{2D} = F/\mu \bar{U}$ and F is the drag force exerted by the fluid on a single fiber per unit fiber length. Therefore, an equivalent drag coefficient f_{2D} for a two dimensional flow is defined as the following:

$$f_{2D} = \frac{2}{3}\left(\frac{B'}{\bar{W}'}\right)^2 f'_{2D} \tag{3.38}$$

Here f_{2D} is a function of S and B while f'_{2D} is a function of S only.

3.2.2 The Brinkman Approximation and An Asymptotic Interpolation

(a) The Brinkman Approximation

The periodic fiber array in Figure 3.1 can also be viewed as a porous medium bounded by two parallel channel walls. The effect of the channel walls on the Darcy flow can be approximately taken into account using a Brinkman equation (Bird *et al.*, 1960 and Ethier & Kamm, 1989)

$$\nabla P = -\frac{\mu}{k_p} V + \mu \nabla^2 V \tag{3.39}$$

which satisfies no slip conditions at the top and bottom boundaries:

$$V = 0 \qquad Z = \pm B \tag{3.40}$$

If K_p, the Darcy permeability coefficient, is defined by its value for an infinite medium, equation (3.39) will reduce to Darcy's law in the dense fiber limit when K_p is small and to the standard stokes equation in the opposite limit when K_p is large. In the present case K_p is given by $K_p = \frac{\pi a^2}{S f'_{2D}}$ where f'_{2d} is obtained from the infinite 2D solution in Sangani & Acrivos (1982). This solution for f'_{2D} is a complicated function of S. However, as shown in the log-log plot in Figure 3.2, Sf'_{2D} is nearly a linear function of Δ and thus f'_{2D} is closely approximated by

$$f'_{2D} \approx \frac{54.95}{S\Delta^{2.377}} \tag{3.41}$$

This formula is accurate to within 10 % for $0.001<S<0.7$. Using equation (3.41), we obtain the following approximation for K_p:

$$K_p = 0.0572\ a^2\ \Delta^{2.377} \tag{3.42}$$

If equation (3.39) is cast in dimensionless form, one can readily show that the magnitude of the viscous layer thickness adjacent to the channel walls is of the order $\sqrt{K_p}$. Therefore, For high fiber density, i.e. $\frac{\sqrt{K_p}}{B'} << O(1)$, the channel wall effect is small and the results of the Brinkman equation approach the 2D limiting solution except for the thin viscous layers in which the flow adjusts to satisfy the no slip condition (3.40). On the other hand, when S is small, i.e. $\frac{\sqrt{K_p}}{B'} >> O(1)$, the porous material has little influence on the flow and the Brinkman equation will correctly predict the pure Poiseuille flow behavior. Using the approximate expression for K_p in (3.42) one finds that $\sqrt{K_p}/B' \sim \Delta^{1.1885}/B$. This relation confirms the results in Figure 3.6, which show that there is a transition from Hele-Shaw potential

regime to viscous behavior as Δ/B passes through unity. It is in the intermediate regime where $\frac{\sqrt{K_p}}{B}$ or Δ/B is of O(1) that the Brinkman equation is of questionable validity.

The solution to equations (3.39) and (3.40) for the velocity profile in the channel is

$$V = -\frac{K_p}{\mu}\frac{dP}{dx}\left(1 - \frac{\cosh(z/\sqrt{K_p})}{\cosh(B'/\sqrt{K_p})}\right) \tag{3.43}$$

By averaging the velocity across the channel height, we can obtain an expression for the effective permeability.

$$K_{p,eff} = -\mu\frac{V_{av}}{dP/dx} = K_p\left(1 - \frac{\tanh(B'/\sqrt{K_p})}{B'/\sqrt{K_p}}\right) \tag{3.44}$$

The drag coefficient f_B derived from this Brinkman equation is given by

$$f_B = \frac{\eta^3}{3(\eta - \tanh\eta)} \tag{3.45}$$

where $\eta = \sqrt{(3f_{2D})} = B'/\sqrt{K_p}$.

(b) Random Fiber Array

The excellent approximation provided by the Brinkman approximation when $B/a > 5$, which will be shown in Figure 3.7, suggests a simple approximation for a random matrix of cross-bridging fibers in a channel. Instead of using the Sangani and Acrivos solution for K_p for a square periodic array, we introduce instead in the Brinkman equation a random cell Carmen-Kozeny approximation for the fiber array. The Carmen-Kozeny equation is given by

$$K_p = \frac{(1-S)^3}{S^2}\left(\frac{a^2}{4C}\right) \tag{3.46}$$

where C is a fiber density correction factor. The expressions for C for parallel, transverse or randomly oriented flow through circular cylinders are given in Happel & Brenner (1973). These solutions are based on a uniform cell model with vanishing shear at the edge of each cell. The randomness in the distribution of fibers can now be taken into account using a stochastic model developed by Yu and Soong (1975). In this model N fibers are randomly inserted into M subregions and a nonuniform fiber density distribution is generated. Each subregion has a different value of S given as

$$S_i^{(k)} = S\ (M/N)\ n_i^{(k)} \quad . \tag{3.47}$$

where $n_i^{(k)}$ is the number of fibers in subregion i. By assuming that there is at least one fiber in each subregion, a different value of K_p is obtained for each region. The average value of K_p, denoted by K_{pr}, is calculated as

$$K_{pr} = \sum_{n_1=1}^{N} \sum_{n_2=1}^{N} \cdots \sum_{n_M=1}^{N} K_p^{(k)} \frac{1}{\prod_{i=1}^{M}(n_i^{(k)}-1)!} \frac{(N-M)!}{M^{(N-M)}} \quad , \quad \sum_{i=1}^{M} n_i = N \tag{3.48}$$

The mean K_{pr} is used to replace K_p in equation (3.39). In the results presented herein we have chosen N and M as 25 and 10 respectively.

(c) The Asymptotic Interpolation

The results in Figure 3.7 indicate that f derived from Lee's (1969) two-term asymptotic solution and the two dimensional solution provide good approximations for both $\Delta/B \gg 1$ and $\Delta/B \ll 1$ respectively. This allows us to develop a new highly accurate interpolation formula for the effective viscosity using a curve fit which asymptotically approaches the limiting expressions of Lee and Sangani & Acrivos. In Lee's two term asymptotic solution the constant b_1 in equation (3.36) is given by

$$b_1 = \frac{K_2(\frac{\pi}{2B})}{K_0(\frac{\pi}{2B})} \tag{3.49}$$

where K_n are modified Bessel functions of order n. The two dimensional asymptotic expression is given by equation (3.38), where f'_{2D} is approximated by equation (3.41). These two asymptotic solutions provide the basis for developing a convenient interpolation formula for f which is valid for all values of S and B. Because there is no intersection between these two asymptotic solutions, the common interpolation formula

$$f = (f_{2D}^n + f_{3D}^n)^{1/n} \tag{3.50}$$

can not be applied directly. Here f_{3D} represents Lee's asymptotic solution for $\Delta/B \gg 1$ and n is a free parameter that will be determined shortly. Since the solution given by equations (3.36) and (3.49) for f_{3D} breaks down rapidly when $\Delta < 2B$, f_{3D} is approximated by the tangent line at $S=S_\Delta$ for $S>S_\Delta$, where S_Δ is the solidity ratio when $\Delta=2B$. This modified expression for f_{3D} for $S>S_\Delta$ is given by

$$f_{3D} = (\frac{1-b_1 S_\Delta}{1+b_1 S_\Delta}) - 2b_1 \frac{(S-S_\Delta)}{(1+b_1 S_\Delta)^2} \tag{3.51}$$

Substituting equation (3.38) and equation (3.36) for $S < S_\Delta$ or equation (3.51) for $S > S_\Delta$ into equation (3.50) and requiring that the value of f at the intersection point of f_{2D} and f_{3D} match the numerical solution exactly, we can obtain a formula for n for different aspect ratios B.

$$n = B/(.1918 + .3308\ B) \tag{3.52}$$

Some results of this interpolation approximation are plotted in Figure 3.7. The formula is accurate to 20% for all values of S when B>0.5.

3.2.3 Diffusive Resistance

The solution of the boundary value problem for the diffusion of a finite size solute through a bounded periodic fiber array is much more difficult than the hydrodynamic problem in subsection 2, since the restricted diffusion coefficient in the fiber array is spatially varying and depends on the solution to a complicated hydrodynamic boundary value problem in which the no slip conditions are satisfied on both the solute and channel-fiber surfaces. However, a simplified approximate expression for the effective diffusion coefficient $D_{iw,eff}$ based on the Brinkman approximation will be proposed which should provide reasonable accuracy provided the solute diameter does not approach the fiber gap spacing Δ'. A very good approximation to the problem of flow through a sphere in a channel filled with a Brinkman medium can be obtained by combining the restricted diffusion coefficient D_{iw} for a particle in a channel without fibers (Ganatos *et al.* 1981) with the known solution for a sphere in an unbounded Brinkman medium. The solution to the Brinkman equation for an unbounded sphere is given in the original theory of Brinkman (1947). This solution leads to the following expression for the drag F_D on the sphere,

$$F_D = 6\pi\mu U r_s \left(1+\frac{r_s}{\sqrt{K_p}}+\frac{r_s^2}{3\,K_p}\right) \tag{3.53}$$

where r_s is the sphere radius and the term in parenthesis is the Brinkman correction to the Stokes drag on the sphere. K_p for a periodic fiber array is given by equation (3.42) and K_p for a random

array is given by equation (3.48). The above result neglects the walls of the channel; however, in Figure 3.8 it is shown that for $\Delta<B$ the walls of the channel provide only a modest correction to the unbounded solution of Sangani and Acrivos (1982), whereas for $\Delta>>B$ one should approach the exact limiting solution of Ganatos *et al.* (1980) in the same way that the Brinkman approximation (3.45) approached the solution for Poiseuille flow in a channel when the sphere was not present in the dilute fiber limit. Therefore, using the Stokes-Einstein relation, we propose the following approximate relation for the solute diffusion coefficient D_{im} in the available space between fibers

$$D_{im} = D_{iw} \left(1+\frac{r_s}{\sqrt{K_p}}+\frac{r_s^2}{3 K_p}\right) \tag{3.54}$$

where D_{iw} is the average diffusion coefficient across the channel height in the absence of fibers described in Ganatos *et al.* (1980, 81).

The above expression for D_{im} still does not include the steric exclusion of the solute by the fibers and the channel walls and the spatial variation of the solute concentration in the available space of the matrix. The latter effects can be treated by solving the solute diffusion equation for the periodic fiber array in Figure 3.1 in which a zero flux boundary condition is applied at the exclusion radius, $r_e=a+r_s$ of the fibers. This last boundary value problem is analogous to the boundary value problem for the pressure field for the Hele-Show flow past a periodic fiber array. The solution to the problem in section 3.2.1 can be readily applied to derive the following expression for $D_{iw,eff}$

$$D_{iw,eff} = D_{im} \left(\frac{1-b_1 S_e}{1+b_1 S_e}\right) \tag{3.55}$$

where b_1, the coefficient of the leading term of the pseudo doubly periodic Weierstrass expansion series, depends only on the effective fiber solid fraction $S_e = S(1+r_s/a)^2$. The coefficient of D_{im} is, therefore, only a function of S_e and is plotted in Figure 3.3.

3.3 Results and Discussion

(a) The Velocity Field for Flow Through A Confined Periodic Fiber Array

The comparisons between the velocity profiles obtained by the present solution and the profiles predicted by Lee's (1969) two-term approximation are shown in Figures 3.4a and 3.4b. In Figure 3.4a the velocity profiles along the radial coordinate at $z=B/2$, $\theta=\pi/4$ are plotted for $S=0.02$ and $B=5$. This figure shows clearly that Lee's approximation (the dotted curves) provides good results for v_r and v_θ for the far field but is a poor approximation for the boundary layer ($r/a<B$) surrounding the fiber surface.

The v_r, v_θ and v_z velocity profiles in the z direction at four different radial positions, $r/a-1=0$, $\Delta/8$, $\Delta/4$, $\Delta/2$, along the $\theta=\pi/4$ coordinate are plotted in Figure 3.4b. The values of S and B are the same as in Figure 3.4a. The solid lines in Figure 3.4b represent the velocity profiles predicted by the present truncated series solution with M=2, N=15 and NPOST=1000. The velocity on the fiber surface is smaller than $0.0005\bar{U}$ everywhere and therefore, would not be visible using velocity scale in this figure. The results show that the velocity profiles for v_r and v_θ in the z-direction are nearly parabolic. The profile for v_z is determined by a linear combination of $Y_n(z)$ functions in equation (29). These functions require that v_z satisfy both the no-slip condition, $v_z(\pm B)=0$, and the zero gradient condition, $\partial v_z(\pm B)/\partial z=0$. Since v_r and v_θ vanish on the channel walls, one can show from the continuity equation that $\partial v_z(\pm B)/\partial z=0$. The dashed curves are the v_r and v_θ profiles obtained from Lee's (1969)

two term solution. The v_z velocity component is zero in Lee's approximation. The results indicate a maximum error at $z \simeq 0.74B$. The two term approximation introduced in Lee & Fung (1969) and used in Lee (1969) assumes that $1-z^2/B^2 \simeq 32\cos(\pi z/2B)/\pi^3$ in satisfying the no-slip conditions on the fiber surface. As noted in Lee & Fung (1969), this is a reasonable approximation only for $B<1$. For larger values of B the no-slip condition is severely violated locally; however, as the results for the dashed curves labelled 1 indicate, the average value of v_r and v_θ is very roughly satisfied at the fiber surface. Since f is a global property, this explains why Lee's two term approximation provides reasonable results for f for values of B for which the no-slip condition is very poorly satisfied pointwise.

The change in the v_r, v_θ and v_z velocity profiles surrounding the fibers in the plane $z=B/2$ along $\theta=\pi/4$ as B is increased, is shown in Figure 3.5. Similar to the velocity profiles in Lee & Fung (1969) for a single fiber, the results reveal that v_z is significant only within a distance of the order of B from the fiber surface and its amplitude is one order of magnitude smaller than v_r and v_θ. The region, where V_z is significant, coincides with the viscous layer where the v_r and v_θ velocity components adjust to the no slip conditions at the fiber surface. Outside this layer, the vertical velocity component is negligible and the fluid behaves like a two dimensional Hele-Shaw flow. Later in this paper we shall show that the dimensionless thickness of this viscous layer δ, which is of O(B), compared to the width of the open gap Δ between adjacent fibers is the critical condition for determining when the drag force due to the fibers will cause the channel resistance to sharply increase. Figure 3.5 also shows that the magnitude of v_z decreases as the aspect ratio B decreases. This suggests that when S is fixed, Lee's (1969) two-term approximation will be approached provided B is small enough. Furthermore, in the limit $S \to 0$, i.e. $\Delta \gg 2B$, the flow will approach the

solution in Lee & Fung (1969) for a single fiber. Similar to the behavior exhibited by the v_z profiles in Figure 3.4b where $\partial v_z/\partial z=0$ on the two channel walls, one can show that v_r not only satisfies $v_r=0$, but $\partial v_r/\partial r$ must also vanish on the fiber surfaces. The profiles in Figure 3.5 exhibit this behavior as $r/a \to 1$.

(b) The Drag Coefficient f and Darcy Permeability K_p

A clearer insight into the mechanism which causes f to increase as B and S are increased is shown in Figure 3.6. In this figure the drag coefficient f is plotted as a function of the ratio of the dimensionless gap spacing Δ to the dimensionless channel half height B for four different aspect ratios, i.e. B=0.5, 1, 5 and 20. This figure reveals that regardless of the value of B, the value of f starts to increase dramatically when the open gap between adjacent fibers becomes smaller than the scale of B. As shown in Figure 3.5, the thickness of the viscous layer around the fiber surface is of order B. This strongly suggests that the sudden increase of f when $\Delta/B < O(1)$ is caused by the overlapping of the viscous layers.

The solutions for f_B obtained from equation (3.45) are shown by the dotted curves in Figure 3.7. These results indicate that the Brinkman approximation does approach the 2D limit when $\Delta/B \ll 1$ and that curves with larger values of B will deviate from the 2D solution at larger values of Δ, or smaller values of S. The results in Figure 3.7 show that when B is larger than 5, the Brinkman approximation is a good approximation for all values of S, whereas when $B \leq O(1)$ the approximation deteriorates rapidly for S in the intermediate range. At these values of B the microstructure between the fibers can no longer be adequately represented by a Brinkman type continuum equation.

In Figure 3.8, the Darcy permeability K_p is plotted against solid fraction S (bottom) and open gap Δ (top) for fibers of increasing aspect ratio B. The upper solid line ($B=\infty$) is taken from Sangani &

Acrivos (1982) for the two-dimensional limiting case. The results show that all the curves for different B merge with the two-dimensional limiting case if S is sufficiently high. This is because Δ decreases as S increases and B/Δ must eventually become >>1. In this limit, the viscous effects coming from channel wall are negligible compared to the viscous interaction between the fibers. In general, the larger the value of B the smaller the value of S at which K_p approaches the two-dimensional result.

(c) The Hydraulic Conductivity and the Diffusive Permeability

The hydraulic conductivity L_p and the diffusive permeability ω are the two major parameters determining capillary transport properties. L_p and ω are related to $K_{p,eff}$ and $D_{iw,eff}$ by

$$L_p = K_{p,eff}\left(\frac{2BL_{jt}}{\mu L}\right) \tag{3.56}$$

$$\omega = D_{iw.eff}\left(\frac{2BL_{jt}}{L}\right) \tag{3.57}$$

where L is the depth of the channel with matrix components and L_{jt} is the total junction length per unit capillary surface area. In Figure 3.9, the various solution for L_p for a cross-bridging proteoglycan matrix in a uniform cleft with cross-bridging fibers of aspect ratio B/a=18.3 are plotted. The junction depth L=400nm, L_{jt}=2000cm/cm^2 and 2B=22nm. All these values correspond to the measurements of frog mesentery interendothelial clefts in Clough & Michel (1988). Starting from the left the curves in this figure represent the two term asymptotic approximation in Tsay *et al.* (1989), the square periodic array solution developed herein, the Brinkman approximation for the statistically random perpendicular array based on the value of K_{pr} described by equation (3.48) and the original random array solution

for an infinite medium used by Curry & Michel (1980) where the Carmen-Kozeny parameter, C=5.

One notes in Figure 3.9 that there is a relatively small difference between the solution for the square array and random array at the fiber densities interest, $S < 0.02$ or $\Delta' > 6.3$nm, and that the two term solution used in Tsay *et al.* (1989) deteriorates rapidly for $S > 0.005$. The Carmen-Kozeny theory underestimates the hydraulic resistance substantially for low fiber density. One also observes that the measured L_p of 5.9×10^{-7} cm/s/cm-H_2O can be achieved by a fiber matrix in a cleft with a fiber density that lies between 0.017 and 0.025 for the square and random arrays respectively. A square matrix of 0.6nm fibers has an open spacing between fibers of 7nm when S=0.017. This is close to the spacing required if the fiber matrix is to serve as the primary molecular sieve. Results not showed here also indicated that the measured L_p can be accounted for by fibers with a radius of 2nm (S=0.08) and 5nm (S=0.19). However, the open spacing between fibers for these matrices are 8.5 and 10.3 nm respectively. Therefore, these fiber matrices would appear to be too sparse to serve as the molecular filter.

The solutions for the solute permeability ω as a function of the solute radius for a cleft with either periodic or random cross-bridging fibers are shown in Figure 3.10. For the ordered square array, the calculations are based on equations (3.53) - (3.56). For the random array, the statistical theory in Ogston (1974) has been used to calculate the steric exclusion of the fibers while the hydrodynamic effect is based on equation (3.48) for K_{pr}. Curves for three fiber radii are presented and for each curve the fiber solid fraction S has been selected to satisfy the measured value of L_p, 5.9×10^{-7}cm/s/cm-H_2O, for frog mesentery. The results show that ω is nearly independent of the fiber radius and while the ordered square array provides some improvement in the comparison with the measured

values, particularly for albumin, the predicted values of ω are much too high for all the smaller solutes.

3.4 Summary

In summary, we have developed in this chapter a highly accurate doubly infinite series solution for flow through a square array of cylindrical fibers confined between two parallel walls. The solution successfully describes the interaction for the fiber array wherein the flow ranges from the irrotational Hele-Shaw limit ($B \ll 1$) to the viscous two-dimensional limiting case ($B \gg 1$). A viscous layer with scale of order B is found on the fiber surface. The vertical velocity component is only significant within the viscous layer. When the viscous layers surrounding the fibers overlap, the drag coefficient of the fibrous bed increases dramatically. Our results show that instead of S and B, Δ/B is the best parameter to judge whether the fiber array can be described by a two-dimensional approximation. When $\Delta/B \gg 1$, the fluid streamlines exhibit a potential flow behavior except in a thin region of O(B) around the fiber surfaces. In contrast to classic Hele-Shaw flow it is not necessary for $B \ll 1$ for this potential outer flow to exist. The excellent approximation provided by the Brinkman approximation when $B/a > 5$ justifies the usage of Brinkman equation in developing $K_{p,eff}$ and $D_{iw,eff}$ for the random fiber array. Also, an approximate hydrodynamic expression for the solute diffusion coefficient, which includes the far field hydrodynamic interaction of the surrounding fibers, has been proposed. For the random fiber array the results are close to those obtained using the stochastic approach of Ogston (1973).

Based on the new analyses developed in this investigation, one finds that the fiber density S=0.017 predicted by the present model to achieve the measured value of L_p for frog mesentery, 5.9×10^{-7} cm/s/cm-H_2O, is significantly less than the value of S=0.05 obtained

in the original calculation of Curry and Michel (1980). The results in Curry & Michel are based on a Carmen-Kozeny equation in which the density correction factor c in equation (3.46) is assigned a constant value of 5 for the dense limit. Compared to the present rigorous results, the hydraulic resistance estimated by the Carmen-Kozeny equation is substantially lower.

The transport properties predicted here are obtained for uniform clefts that are filled throughout with cross-bridging fibers and no junctional strands are present. Fibers of 0.6, 2, and 5 nm radius, corresponding to two types of proteoglycans and the cross-bridging fibers observed in Firth *et al.* (1983) respectively, are examined. In order to account for the measured L_p for frog mesentery, the open spacing between fibers for these matrices are 7, 8.5 and 10.3nm. The open spacing Δ'=7nm is close to the spacing required if the fiber matrix is to serve as the primary molecular sieve. Therefore, for a matrix which fills the entire cleft length, only the matrix with a=0.6 nm corresponds closely to the required dimensions of the molecular sieve. For fibers of radius a=2 and 5nm, to serve as the primary molecular filter and also to account for L_p, the fibers would need to be more closely spaced and appear only in a portion of the cleft length.

Although an ordered fiber matrix which fills the entire cleft can account for L_p and the larger solute selectivity, it fails to account for the measured permeability for the small and intermediate size solutes. According to the present one-dimensional calculation, which neglects the lateral spreading and restriction effects of the junctional pores, an open cleft filled with fiber matrix of a=0.6nm and S=0.017 would have a permeability to NaCl of 190 $\times 10^{-5}$ cm/sec, compared with the measured value of 44-60 $\times 10^{-5}$ cm/sec. Because the fiber matrix imposes very little diffusive resistance to small solutes, one would think that it is reasonable that the junctional

strand is responsible for the additional diffusive resistance. If this is the case, then there must be additional resistance to water movement from the junctional strand. Therefore, the resistance to water movement from the matrix must be reduced. For the cleft with fiber matrix of a=0.6nm, if one require that the matrix continue to be the primary filter, the fiber density must be kept the same therefore the matrix must occupy less than the total cleft depth.

In conclusion, one find that a cleft filled with a fiber matrix and without junctional strand can not explain all the existing transport properties for frog mesentery. Two questions have been raised by the present study: (i) are there junction strand-pore geometries which can effectively reduce diffusive permeability and still be compatible with a fiber matrix model in the wide part of the cleft and (ii) if the junction strand is present is it necessary for the fiber matrix to be present in all of the wide portion of the cleft. These questions will be addressed in the next chapter where a fourth region at the entrance of the cleft has been added to study the effects of a localized distributed fiber layer.

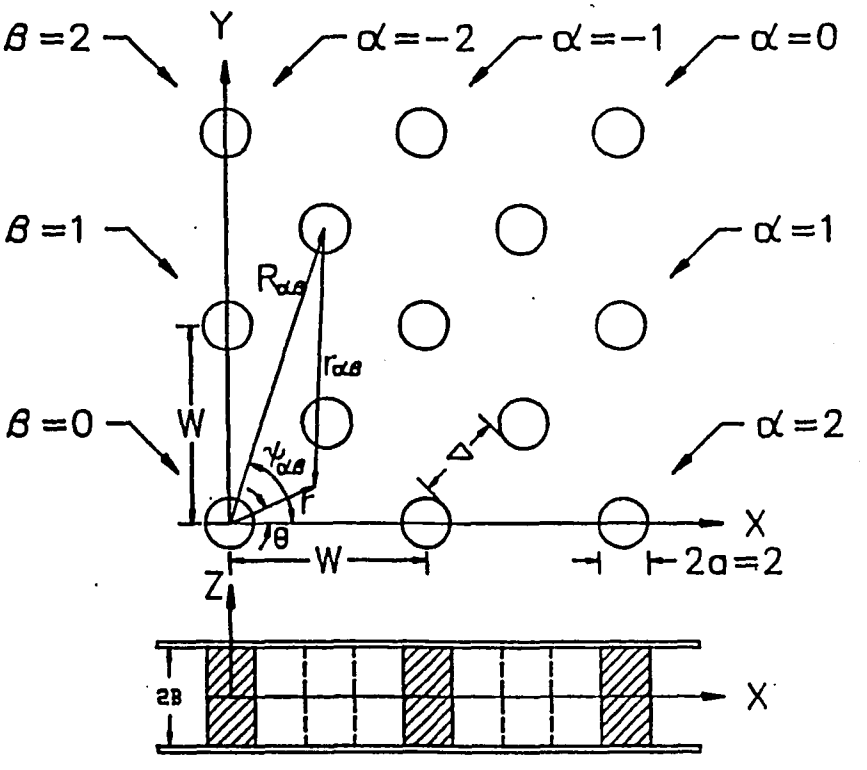

Fig.3.1: A top view and a side view of the idealized periodic configuration channel. All the lengths are scaled relative to the fiber radius a.

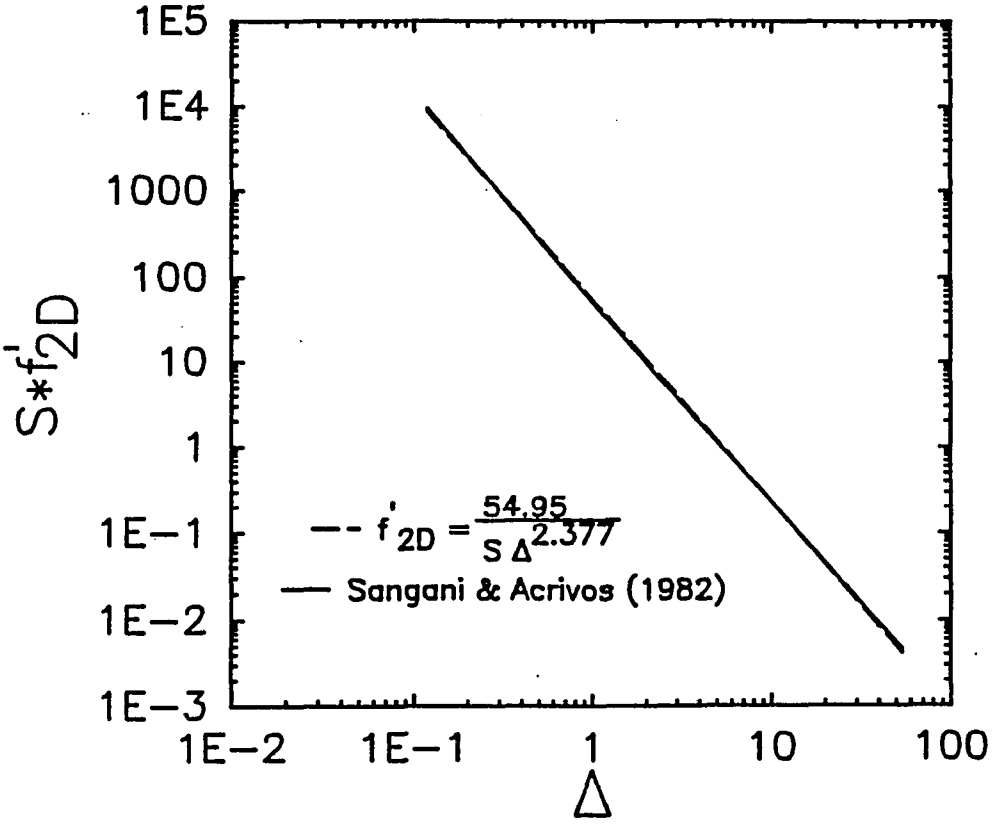

Fig.3.2: A comparison between the rigorous solution (solid line, Sangani & Acrivos, 1982) and the curve fitting results using Equation (3.41).

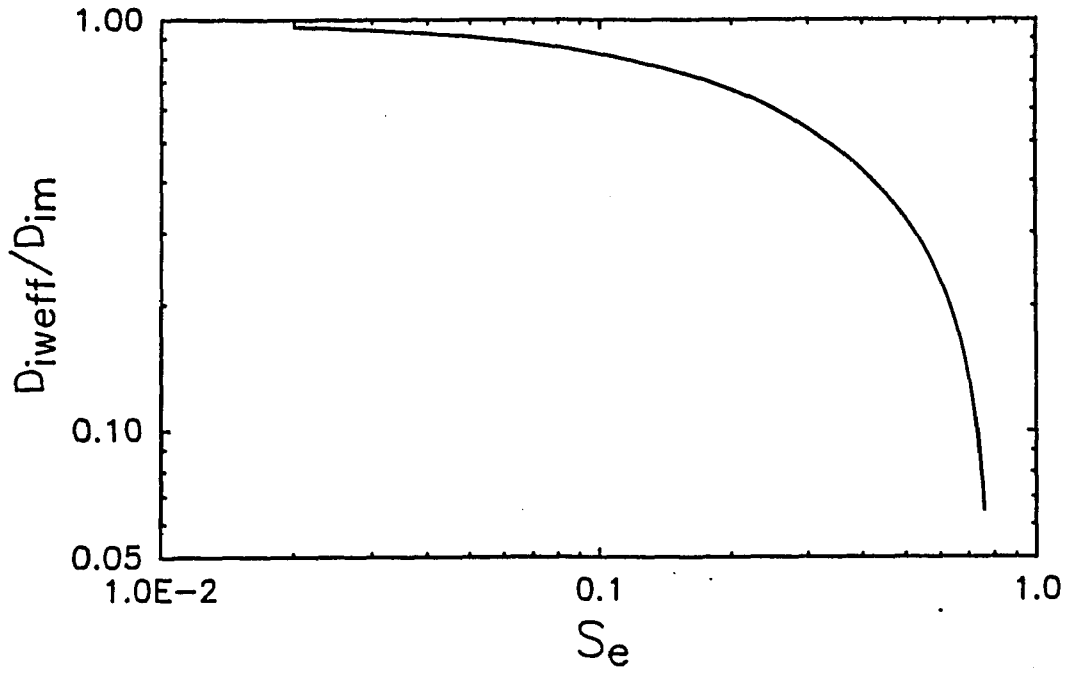

Fig.3.3: The ratio of $D_{iw,eff}/D_{im}$ for square array of cross-bridging vs. the effective fiber solid fraction S_e.

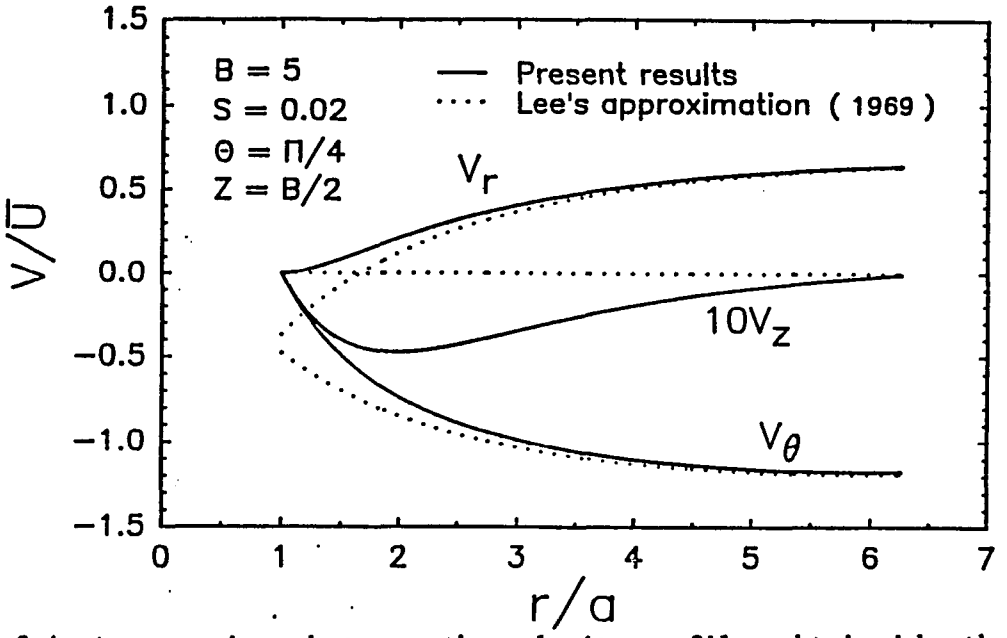

Fig.3.4a:A comparison between the velocity profiles obtained by the present solution and the profiles predicted by Lee's (1969) two-term approximation. Profiles are shown in the z-B/2 plane along a $\theta=\pi/4$ coordinate for a fiber volume fraction S=0.02 and an aspect ratio B=5.

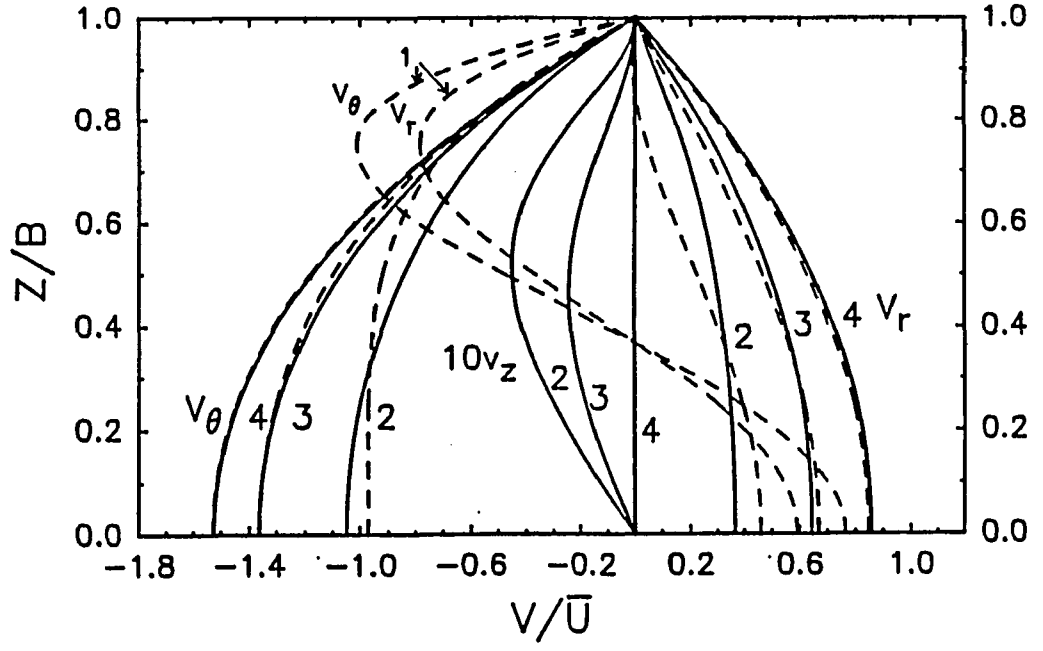

Fig.3.4b:v_r, v_θ and v_z velocity profiles in the z-direction at four different radial positions, $\frac{(r-a)}{a}$ = 0 (1), $\frac{\Delta}{8}$ (2), $\frac{\Delta}{4}$ (3) and $\frac{\Delta}{2}$ (4) on line $\theta=\pi/4$ joining fiber centers. Δ is the non-dimensional gap spacing between fibers. The dashed curves are the v_r and v_θ profiles obtained from Lee's (1969) two-term solution in which v_z=0. The solid curves are predicted by the present solution. S=0.02 and B=5.

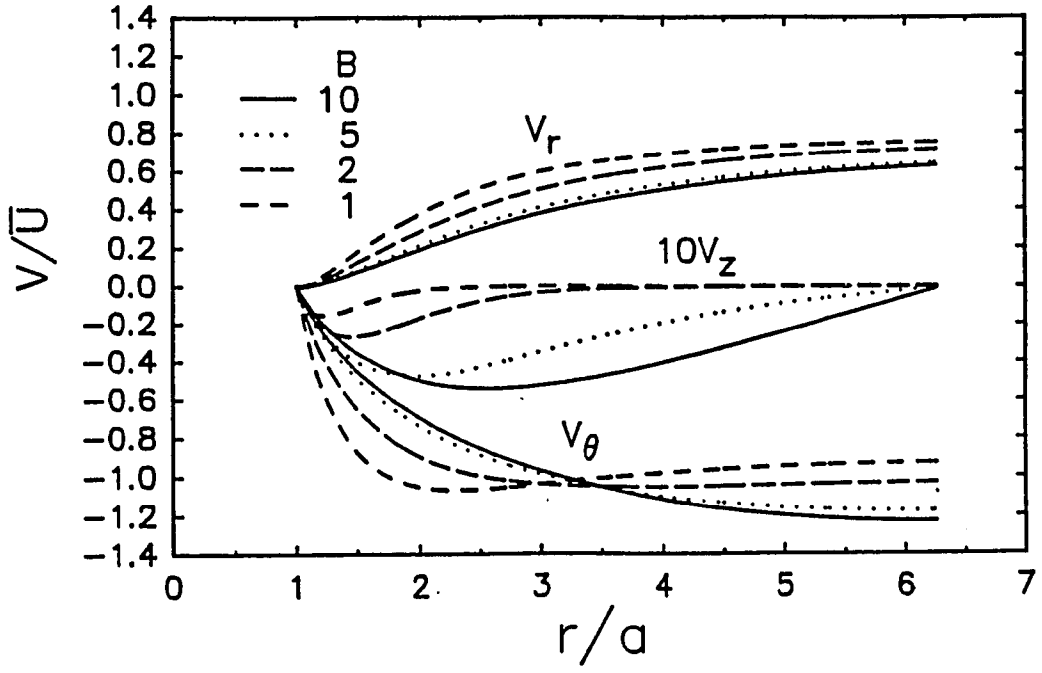

Fig.3.5: Solutions for v_r, v_θ, v_z velocity profiles along the $\theta=\pi/4$ coordinate at $z=B/2$ for fibers with varying aspect ratio B. The fiber volume fraction S=0.02. Note that the magnitude of v_z is enlarged by a factor of 10.

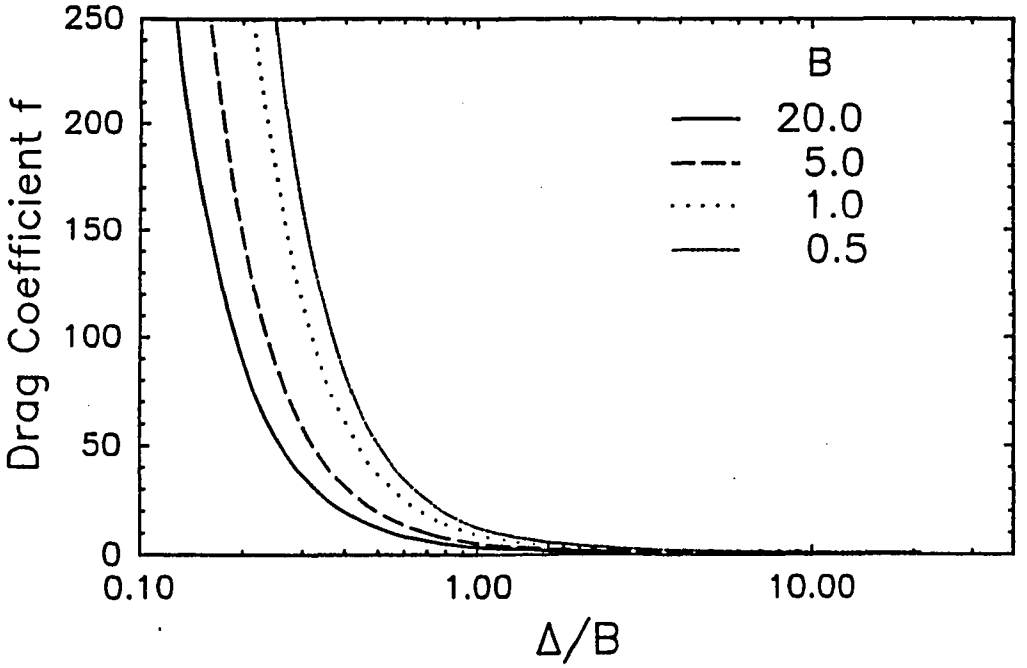

Fig.3.6: The drag coefficient f vs. the ratio of gap spacing to channel half height Δ/B for four different aspect ratios B.

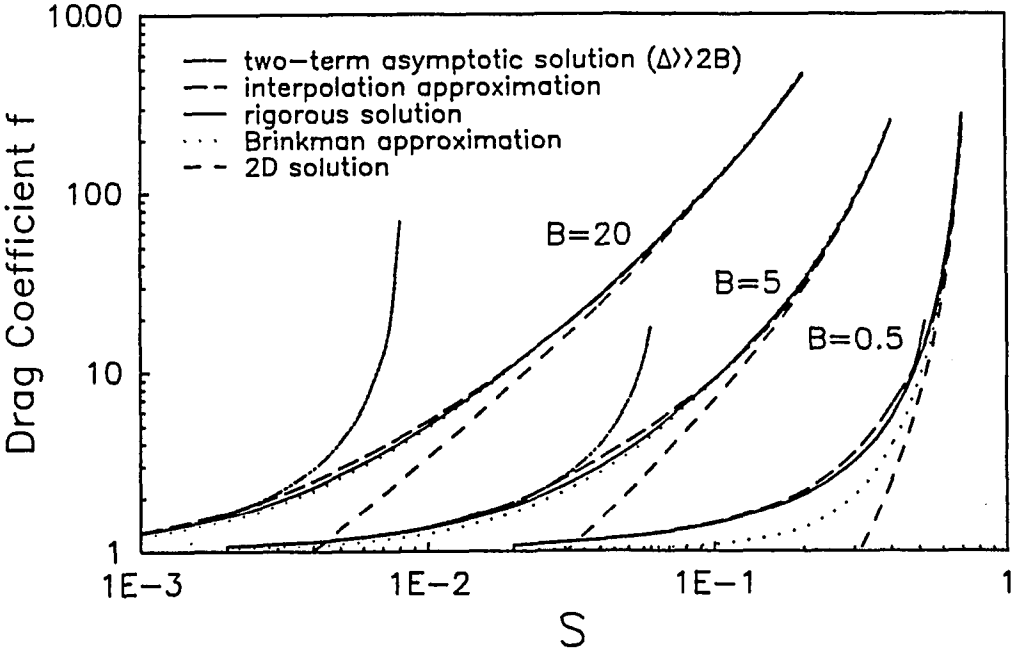

Fig.3.7: A comparison between the drag coefficients obtained by the present solution (——), the interpolation approximation (– – –) and the Brinkman approximation (.....; eq. (45)). The two-term asymptotic solution of Lee (1969) (-..-), and the 2D solution of Sangani & Acrivos (1982) (- - -), are also shown in the figure.

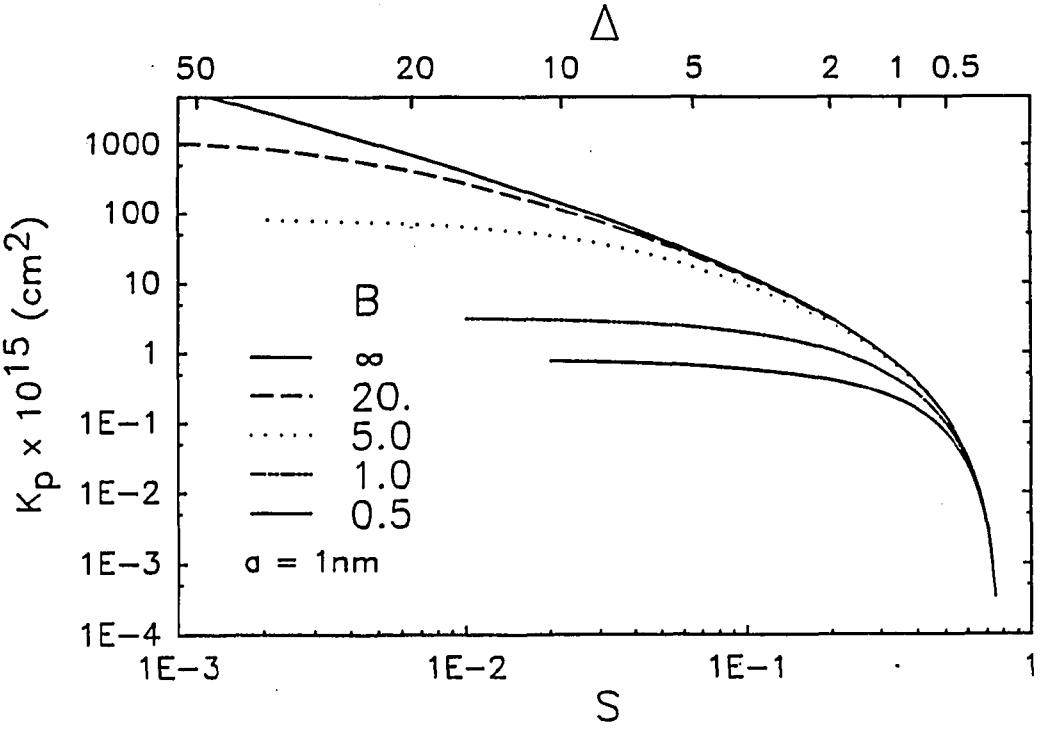

Fig.3.8: The Darcy permeability K_p plotted as a function of the fiber volume fraction S (bottom) and the dimensionless gap spacing Δ (top) for various aspect ratio fibers B.

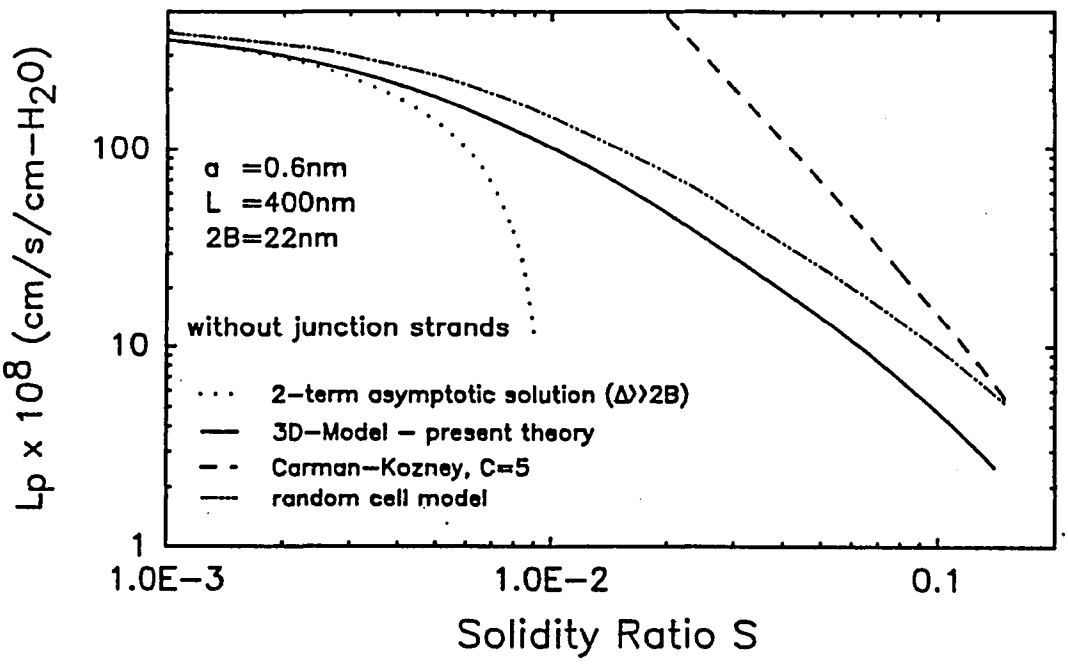

Fig.3.9: Various solutions for the hydraulic conductivity L_p for a cross-bridging fibers with B=18.3. The junction depth L is 400 nm. L_{jt}=2000 cm/cm^2. Solutions are obtained by the 2-term asymptotic approximation (Tsay et al.,1989)(.....), square array solution (_____), the Brinkman approximation for two dimensional random array (-..-..-), and the Carmen-Kozeny solution with C=5 used by Curry & Michel (1980)(- - -).

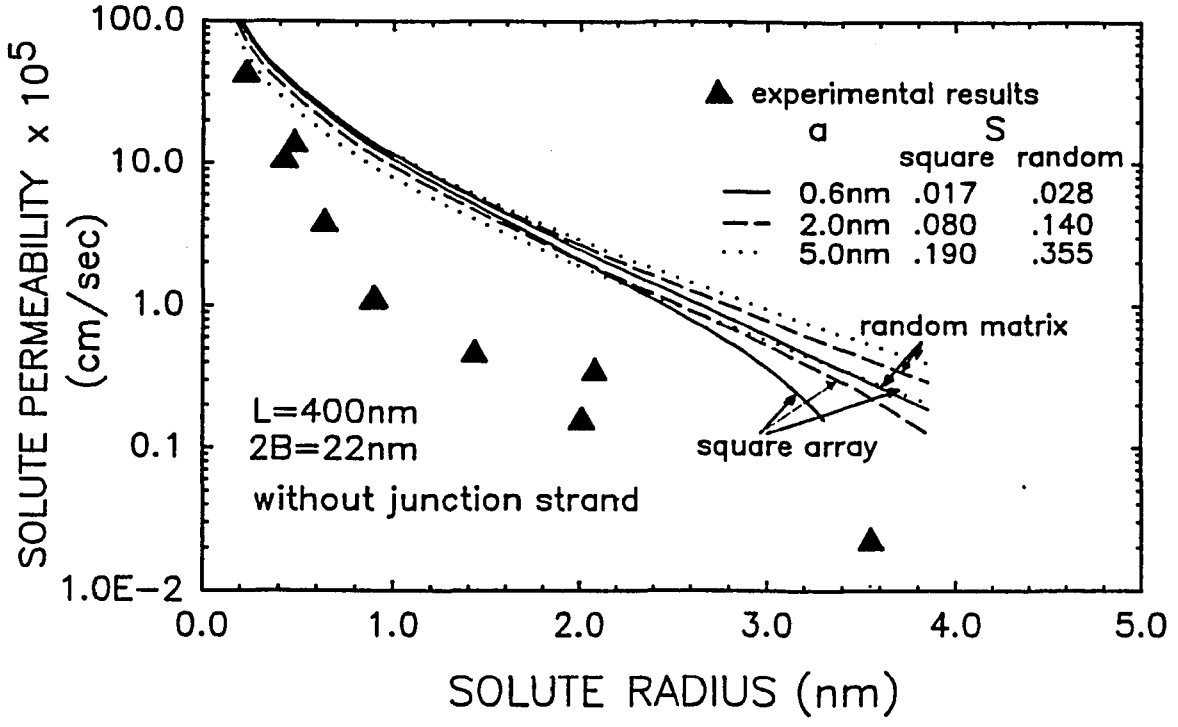

Fig.3.10: Solutions for the solute permeability ω as a function of the solute radius r_s. The triangular symbols are measured values (Curry, 1986). The continuous theoretical curves use the Stokes-Einstein relation to determine the free solute diffusion coefficient. The solid curves with a=0.6 nm, dashed curves with a=2 nm and dotted curves with a=5. The top three curves are for a cleft with random cross-bridging fibers and the bottom ones are for periodic fibers. In both cases, the fiber densities are selected to satisfy L_p=5.9x10^{-7} cm/s/cm-H_2O.

CHAPTER IV

JUNCTION-PORE-MATRIX MODEL

4.1 Introduction

In this chapter we shall attempt to combine both the junction strand and fiber matrix elements that have been considered in the two previous chapters into an integrated junction-pore-matrix model for the cleft. In addition we shall also examine the possibility that a fiber matrix fills only a small fraction of the cleft depth. This more sophisticated model is part of an evolving effort to develop a theoretical model which is able to reconcile permeability data and morphological observations of capillary endothelia with the ultimate objective of obtaining a better understanding of the detailed junction structures which regulate capillary permeability.

As already discussed, there are two major hypotheses describing the molecular filter at the capillary membrane, the pore theory and the fiber matrix theory. In pore theory the small discontinuities in the junctional strand arrays are assumed to be the primary molecular filter. In fiber matrix theory, a fibrous network associated with the cell surface and the wide part of the junctional cleft is assumed to be the major molecular sieve. Based on a simple one-dimensional model, both theories assume that the capillary permeability is proportional to the length of the open junction.

In the two previous chapters, feasibility studies of the pore and fiber matrix theories have been performed. The new three-dimensional model, proposed in chapter 2 for the junction strand with its

pores (Tsay *et al.* 1989), indicates that the previously accepted one-dimensional pore or slit models must be seriously challenged. It was shown that due to the lateral spreading of water and solute at the entrances/exits of the junctional pores and the hydrodynamic interaction between them, capillary permeability is not proportional to the length of the open junction. Also, the new analysis of a cross-bridging fiber matrix (chapter 3) which is based on a more rigorous hydrodynamic theory for water filtration and approximate theories for solute diffusion, indicates that a fiber matrix, which fills the entire cleft, can not by itself account for the diffusive permeability for small solutes. Because the fiber matrix imposes very little additional diffusive resistance to small molecules, one is strongly led to believe that the junctional strands must make a significant contribution to this required additional resistance. In this chapter, we thus wish to examine the relative contributions of junction strands and a fiber matrix to capillary transport using a combined model with both structural components.

Two fundamental questions will be explored in this chapter: (i) are there junction strand-pore geometries which can effectively reduce diffusive permeability and still be compatible with a fiber matrix model in the wide part of the cleft, and (ii) if the junction strand is present, is it necessary for the fiber matrix to be present in all or part of the wide portion of the cleft? To answer these questions, one needs to obtain a more precise molecular model of the junctional strand with its pores. In addition, we shall need to construct a modified model to examine the effects of a fiber layer which fills only a portion of the wide part of the cleft.

Numerous morphological studies have been performed in attempt to delineate the precise pore structure of the junctional protein strands. However, due to the limitations of the techniques used, many of the results are still controversial. For example, Bundgaard (1984)

first attempted to examine the three-dimensional junction ultrastructure using the serial sectioning technique. In this study, rat heart capillaries were reconstructed using conventional 40-60 nm thin or 10-15 nm ultrathin serial section electron microscopy (EM). Bundgaard observed that most of the junction strands appear to be closed, except for some small gaps 4-5 nm high and 5-30 nm long and some very infrequent larger gaps 10-20 nm high and 20-80 nm long formed by the discrete breaks in the junction protein strands. These larger gaps may correspond to the tortuous pathway proposed by Wissig (1979). In contrast to Bundgaard's work, Ward *et al.* (1988) examined the three dimensional features of the junctions of rat cardiac capillaries by using a goniometric tilting technique. After considering the tilting effects, they claimed that more than 70 percent of the random thin sections of junctional clefts were actually open. They concluded that the pathways for small and intermediate solutes were not formed by interruptions in continuous lines of membrane fusion but by a continuous junctional region with a narrowed opening. The size of the pores or openings has been examined using electron-dense tracers experiments. Palade *et al.* (1979) and Simionescu (1983) showed that the endothelial junctions of skeletal muscle capillaries were impermeable to tracer similar or larger than microperoxidase (MP, d≈2nm) and concluded that junctional pores could only allow the passage of hydrophilic solutes smaller than 2nm. However, this observation hasn't been confirmed by many other researchers. Karnovsky (1967, 68), Wissig (1979), and Ward *et al.* (1988) found that molecules as large as horse-radish peroxidase (HRP; d≈5-6nm) can pass through the junctional pores.

Based on these observation of the pore structure of the junction strand, three schematic diagrams of junction protein arrangements in the opposing plasmalemma membranes are shown in Figure 4.1. The protein arrangement in Figure 4.1a gives rise to the long rectangular

slit opening proposed in the one-dimensional constricted channel models. This type of slit opening is suggested by goniometric tilting of random EM sections (Ward *et al.* 1988). The alternating zipper arrangement of junction proteins shown in Figure 4.1b was suggested in (Tsay *et al.* 1989) based on the observation of Firth *et al.* (1983) that the average spacing between junctional proteins in each membrane of pig placental capillary was just twice the diameter of the individual proteins (11nm). This structure represents the small gaps suggested by Bundgaard's ultrathin sections. Arguments favoring the selection of the configuration in Figure 4.1b instead of that in Figure 4.1a have been discussed in chapter 2. One important reason was that if junction proteins were absent in these longer discontinuities, the membrane forces which determine the equilibrium spacing in the wide part of the cleft would also be operative in the region where the break appears. Thus, if the membrane bending resistance over these longer breaks was small, it is anticipated that their gap height should be nearly the same as the background channel height. The larger breaks, observed in Bundgaard (1984), support this conjecture concerning the gap height of the larger breaks. The possibility that the discontinuities in the junction strand are longer than a single missing protein and widely spaced in the junction strand is described in Figure 4.1c.

In this chapter, three different junctional pore models, i.e.: circular pores of 4.5-5.5 nm radius, rectangular slits of 8 nm height, and large breaks of 22 nm height, will be used to examine the relative importance of the constricted region and the open junctional discontinuities in determining capillary permeability. Here, the large pores, 22 nm in height, can not be the primary molecular filter and a fiber matrix in some part of the cleft is required to provide the proper sieving properties.

There is evidence indicating that the components of the endothelial cell glycocalyx may correspond to the fiber matrix proposed in the fiber matrix theory (Curry and Michel 1980). Using ruthenium red staining, Luft (1966) first showed that there was a 'fluffy' endothelial coat. Recent studies indicate that this glycocalyx carries a negative charge and is able to bind the cationized ferritin in a thin layer of 20 to 30 nm thickness near the endothelial wall (Turner *et al.*, 1983). Adamson (1990) studied the fiber matrix hypothesis by comparing normal capillary hydraulic conductivity L_p with L_p measured after partial degradation of the endothelial cell glycocalyx. He observed a two to three fold increase in capillary L_p in frog mesentery capillary. Other evidence for the presence of a fiber matrix structure include: Firth *et al.* (1983), in his studies on pig placental capillaries, suggested that there were linking molecules with radii 5 to 10 nm with a spacing as large as 19 nm in the wide portion of the clefts. Silberberg (1987) also proposed that the linking molecules might be necessary to provide the nearly uniform cleft width in the wide portion of the clefts.

Although there is evidence showing the presence of the fiber matrix, the detailed structure and distribution of the endothelial fibers are still unknown. In this chapter, a model for a fiber matrix which fills all or part of the wide portion of the cleft will be developed. Fiber matrices of 0.6 nm, 2 nm and 5nm fiber radii, corresponding to proteoglycan side chains (Curry 1986), proteoglycan fibers in basement membrane and the cross-bridging molecules observed in Firth (1983), in that order, will be examined.

The present theoretical model is an extension of the three-dimensional model proposed in Tsay *et al.* (1989). Compared to the previous model, there are four major advances in this work. First, by adding a fourth layer at the cleft entrance and using boundary matching techniques, a theory is developed for examining the possible

effect of a fiber matrix which fills only a portion of the wide part of the cleft. This allows us to examine the effect of a thin fiber layer at the cleft entrance. Second, the new hydrodynamic theories developed in chapter 3 for water filtration and molecular diffusion through a confined fibrous bed are applied to the junction-pore-matrix model. The new theory for water filtration, which includes both the effects of the channel walls and the fiber matrix, is a rigorous solution for a periodic fiber array. It was also shown that the Brinkman equation provides a very good approximation for a random fiber array. Third, in determining the capillary permeability, the relative importance of small junctional constrictions and larger breaks, which correspond to the infrequent tortuous pathways,is examined. Finally, the previous model for the junction strand in chapter 2 considered only water filtration. In the present chapter, a parallel theory for the junction-pore-matrix model has been developed for molecular diffusion.

4.2 Mathematical Modelling

4.2.1 Simplified Model of Junctional Cleft

A top view of the idealized structure for the intercellular cleft based on the electron microscopic studies by Wissig (1979), Firth et al (1983), and Bundgaard (1984) is shown in Figure 4.2. The model for filtration and diffusion through this three-dimensional structure is an extension of the one proposed in Tsay *et al.* (1989). This new junction-pore-matrix model combines the hydrodynamic interactions between junctional pores and the additional drag imposed by a fiber layer which fills part or all the wide part of the cleft. The three-dimensional sketch of the model was shown in Figure 2.2a. In the model the tight junction strands have been converted into a barrier that is impermeable except for the junctional pores. The junctional

pores connect the two wide portions of the cleft and a fiber layer is assumed to appear at the lumen front of the cleft.

Three different type of junction pores are examined in the model. The circular pores of radius r_p=5.5 nm and the small rectangular pores of height 2b=8nm represent the small pores suggested by Bundgaard (1984) and Firth et al (1983). The large rectangular pores of width 2b=2B represent the infrequent larger breaks proposed by Bundgaard. Here 2B is the width of the wide portion of the cleft. The sizes of the small pores are chosen to fit the reflection data of solutes of 0.5 to 3.5 nm radius (Curry 1986) and the width of large tortuous pore is set based on the assumption of the force balance between the plasma membranes. The depth of the junctional pores L_2 is chosen to be the same as the approximate size of a single junction protein molecule, 11nm (Firth *et al.* 1983). L_1 and L_3 are the depths of the cleft on each side of the junction strand. The value of L_1 determines the position of the junctional strand. Results in the previous study (Tsay *et al.*, 1989) indicate that the position of junction strand has very little effect on the total hydraulic resistance across the junctional cleft; therefore, one chooses $L_1 = L_3$ in the following calculation. L is the total cleft depth and L_f is the depth of the fiber layer at the lumen front. The distance between two adjacent pores, $2D$, is one of the most important parameters determining the membrane permeability.

In the model, periodic and random fiber arrays are examined. For the periodic array, the fibers are represented by a periodic square array of circular cylindrical elements. These fibers are assumed to be oriented perpendicular to the plasmalemma membranes forming the interendothelial channel. The fiber diameter is $2a$ and the distance between adjacent fibers is $2W$. The open spacing between fibers is Δ. The volume fraction of the fiber matrix is S. Three different fiber radii 0.6, 2.0, and 5.0 nm are examined.

4.2.2 Formulation

In order to solve the water filtration and solutes diffusion problems in the present three-dimensional model, the intercellular cleft is divided into three regions. Regions 1 and 3 are the wide portions of the cleft at the lumen and tissue fronts of the endothelial cell respectively. Region 1 is divided into two subregions. The subregion at the cleft entrance is the region with fibers present. Region 2 represents the pores in junctional protein strands. Following the approach in chapter 2, the flow in each region is examined separately. Two major simplifications are introduced in the model. First, the shape of the pore at the entrance and exit boundary of the junction strand is approximated by a rectangular hole of dimensions 2dx2B. Second, the water flow in the wide portion of the cleft is analyzed using two-dimensional Hele-Shaw theory. The detailed reasons justifying these simplifications have been discussed in previous chapters.

In regions 1 and 3 an (x,y,z) coordinate system is chosen parallel to the walls of the two adjacent endothelial cells and the origin of the z coordinate taken as the midplane of the cleft. Since the width of the cleft 2B is small compared to both the average distance between the pores, 2D, and the depth L_1 and L_3, the water flow in the wide part of the cleft can be approximated by a Hele-Shaw flow. The continuity and momentum equations for this flow are:

$$\frac{\partial u}{\partial x} + \frac{\partial v}{\partial y} = 0 \qquad (4.1)$$

$$\nabla p = \mu \frac{\partial^2 \vec{u}}{\partial z^2}, \qquad \vec{u} = ui + vj \qquad (4.2)$$

Here u,v are the x,y components of the fluid velocity and w = 0. The boundary conditions at the boundary plasmalemma membranes of the cleft are no slip

$$u = v = 0 \quad z = \pm B \tag{4. 3}$$

The solution of equation (4.2) which satisfies equation (4.3) is

$$\vec{u} = \vec{u}_o(1 - \frac{z^2}{B^2}) \tag{4. 4}$$

where

$$\vec{u}_o = - \frac{B^2}{2\mu} \nabla P \tag{4. 5}$$

is the velocity at the center plane z=0 of the cleft.

From equation (4.5) one can show that the x,y components of the centerline velocity satisfy

$$\frac{\partial u_o}{\partial y} - \frac{\partial v_o}{\partial x} = 0 \tag{4. 6}$$

Combining equations (4.4) and (4.5) and substituting in equation (4.1), one obtains

$$\frac{\partial^2 P}{\partial x^2} + \frac{\partial^2 P}{\partial y^2} = 0 \tag{4. 7}$$

Equation (4.6) shows that the z component of the vorticity vanishes and the motion in the x,y plane is irrotational. The velocity components in this plane thus satisfy a potential flow equation and it is therefore not possible to satisfy no slip boundary conditions in the x, y plane when equation (4.2) is used as the approximate momentum equation. Equation (4.7) shows that the pressure field also satisfies Laplace's equation in the x, y plane. The viscous resistance in Hele-Shaw flow originates from the shearing stress at the boundary plasmalemma membranes at $z = \pm B$ rather than the vertical boundaries or obstacles in the x, y plane, where, as just noted, no slip boundary conditions cannot be satisfied.

The effect of the hydrodynamic interaction with the cross-bridging fibers in the wide portion of channel can be treated by replacing the actual fluid viscosity μ by an effective viscosity μ_{eff} in the region where fibers are present. The effective viscosity μ_{eff} is defined by $\nabla\langle P\rangle=-3\mu_{eff}\langle U\rangle/B^2$ where $\langle\rangle$ denotes an average value over a region which is small compared to the depth of the fiber layer L_f. The effective viscosity can be written as μf where f is an hydrodynamic interaction function which depends on the fiber configuration, the fiber volume fraction S, and the aspect ratio B/a of the fibers. It is shown in Tsay *et al.* (1991) that the following solution of the Brinkman equation gives very good approximation for f.

$$f = \frac{\beta^3}{3(\beta-\tanh\beta)}, \tag{4. 8}$$

where $\beta=B/\sqrt{K_p}$. K_p is the Darcy permeability which describes the flow through an infinite matrix which has the same fiber geometry as the interior of the bounded flow under consideration. For a two-dimensional square fiber array, K_p is given by

$$K_p= 0.0572\ a^2(\Delta/a)^{2.377} \tag{4. 9}$$

The expression for K_p for a random fiber array is obtained using a stochastic model described in Weinbaum *et al.* (1991).

As shown in Figure 4.2 the hydrodynamic interaction with the cross-bridging fibers at the cleft entrance and the interaction between junction pores can be represented by a periodic boundary value problem which satisfies the following boundary conditions on the velocity field in region 1. In order to distinguish the fiber layer at the cleft entrance, region 1 is divided into two subregions. Subscripts *'1f'* and *'1w'* represent the regions with and without fiber present, respectively.

Region *1w*:

$$\frac{\partial P_{1w}}{\partial y} = 0 \qquad y=0,\ D \tag{4.10}$$

$$\frac{\partial P_{1w}}{\partial x} = 0 \qquad d<|y|<D\ ,\ x=0$$

$$\frac{\partial P_{1w}}{\partial x} = -\left(\frac{2\mu}{B^2}\right)u_{00} \qquad |y|<d,\quad x=0 \tag{4.11}$$

Region *1f*:

$$\frac{\partial P_{1f}}{\partial y} = 0 \qquad y=0,\ D \tag{4.12}$$

$$P_{1f} = P_L \qquad x=L_1 \tag{4.13}$$

Matching Boundary Conditions

$$P_{1w} = P_{1f} \qquad x=L_1-L_f \tag{4.14}$$

$$f\,\frac{\partial P_{1w}}{\partial x} = \frac{\partial P_{1f}}{\partial x} \qquad x=L_1-L_f \tag{4.15}$$

Equation (4.11) describes the impenetrability of the junctional strand except for the region -d<y<d of the missing protein or proteins, whereas equations (4.10) and (4.12) are symmetry or periodicity conditions. u_{00} in equation (4.11) is the centerline velocity at the pore entrance. For the reasons already discussed, one can not satisfy no slip boundary conditions on the v component of the velocity along either surface of the junctional strand. This approximation will have only a very minor effect on the results, since the numerical solutions indicate that the velocities induced along the wall of the junctional

strand by the fluid jets through the pores are very small even when there is slip along this boundary. In addition to boundary conditions (4.10) through (4.12) we require that the total pressures on the lumen and tissue sides of the cleft P_L and P_A be constants determined by local difference in hydrostatic pressures across the endothelial layer. The matching boundary conditions at the interface of the two subregions are shown in equations (4.14) and (4.15). Equation (4.14) requires that the pressure be continuous and equation (4.15) requires that the u component of the velocity be continuous. Because the problem is treated as a Darcy's potential flow in the xy plane, the v component of the velocity can not be matched.

Equivalent boundary conditions can be written for region 3 except that there is no fiber layer present at the tissue front and therefore $L_f = 0$.

4.2.3 Solution for Hydraulic Conductivity

The solutions to equation (4.9) subject to boundary conditions (4.10) to (4.13) for subregions 1w and 1f are

$$P_{1w}(x,y) = a_0 x + b_0 + \sum_{n=1}^{\infty} [a_n \sinh(\lambda_n x) + b_n \cosh(\lambda_n x)] \cos(\lambda_n y) \quad (4.16)$$

$$P_{1f}(x,y) = A_0 x + B_0 + \sum_{n=1}^{\infty} [A_n \sinh(\lambda_n x) + B_n \cosh(\lambda_n x)] \cos(\lambda_n y) \quad (4.17)$$

where

$$a_0 = -2\mu u_{00} d/(B^2 D)$$

$$a_n = -4\mu u_{00} \sin(\lambda_n d)/(B^2 \lambda_n^2 D)$$

$$B_0 = P_L - A_0 L_1$$

$$B_n = -A_n \tanh(\lambda_n L_1), \qquad \lambda_n = n\Pi/D, \qquad n=1,2,3,.... \tag{4.18}$$

By applying boundary and matching conditions (4.14) (4.15), one obtains the following expressions for the other unknown coefficients in (4.16) (4.17):

$$\begin{aligned} b_0 &= -(L_w + fL_f)a_0, \qquad L_w = L_1 - L_f \\ b_n &= a_n F_n \\ A_0 &= f\, a_0 \\ A_n &= f H_n a_n \end{aligned} \tag{4.19}$$

where $$H_n = \frac{1-\tanh^2(\lambda_n L_w)}{[1+(f-1)\tanh(\lambda_n L_1)\tanh(\lambda_n L_w) - f\tanh^2(\lambda_n L_w)]}$$

$$F_n = -\left[\frac{f + \coth(\lambda_n L_f)\ \tanh(\lambda_n L_w)}{f\ \tanh(\lambda_n L_w) + \coth(\lambda_n L_f)}\right]$$

The average pressure at the exit of the pore is

$$\bar{P}_1 = \int_{-d}^{d} P_{1w}(0,y)dy/2d \tag{4.20}$$

The pressure drop across region 1 is

$$P_L - \bar{P}_1 = \frac{2\mu u_{00}}{B^2 D}\left[\, d(L_{w,1} + fL_{f,1}) - \frac{2}{d}\sum_{n=1}^{\infty} \frac{F_n \sin^2(\lambda_n d)}{\lambda_n^3}\,\right] \tag{4.21}$$

For region 3, the solution procedure is the same as region 1. The pressure drop across the region is

$$\bar{P}_2 - P_A = \frac{2\mu u_{00}}{B^2 D}\left[\, dL_3 + \frac{2}{d}\sum_{n=1}^{\infty}\frac{\tanh(\lambda_n L_3)\sin^2(\lambda_n d)}{\lambda_n^3}\,\right] \tag{4.22}$$

In region 2, the entrance and exit effects which have been shown to be small in Dagan *et al.* (1982) are neglected. The flow is assumed to follow a simple Poiseuille relation between flow rate and pressure drop. The relations for a circular and a rectangular pores in that order are:

$$(\bar{P}_1 - \bar{P}_2) = J_v\left(\frac{2D}{L_j}\right)\left(\frac{8\mu L_2}{\pi r_p^4}\right) \tag{4.23}$$

$$(\bar{P}_1 - \bar{P}_2) = J_v\left(\frac{2D}{L_j}\right)\left(\frac{\mu L_2}{16b^3 d}\right)\left[\sum_{m=0}^{\infty}\sum_{n=0}^{\infty}\frac{1}{(\alpha_n\beta_m)^2(\alpha_n^2+k^2\beta_m^2)}\right] \tag{4.24}$$

where $\alpha_n=\beta_n=(n+0.5)\pi$ and $k=b/d$. At the entrance/exit of the Hele-Shaw regions, the junction pore is approximated by a slit of width 2d and height 2B. By matching the volumetric flow rates J_v with the parabolic flow at the pore entrance and exit, one obtains the following relation between J_v and the centerline velocity u_{00}

$$u_{00} = \frac{3D}{4BdL_j} J_v \tag{4.25}$$

where L_j is the total junction length per unit capillary surface area.

According to the Kedem-Katchalsky relations, the hydraulic conductivity L_p is defined by $(J_v/\Delta P)_{\Delta\pi=0}$. By substituting equation (4.25) into equations (4.21) and (4.22) and adding the results for the pressure drop across regions 1, 2 and 3, one obtains

$$P_L - P_A = J_v(R_1 + R_2 + R_3) \tag{4.26}$$

where

$$R_i = \frac{3\mu}{2B^3L_j}\left[L_{w,i} + fL_{f,i} - \frac{2}{d^2}\sum_{n=1}^{\infty} \frac{F_{n,i}\sin^2(\lambda_n d)}{\lambda_n^3}\right],\ i=1,3 \qquad (4.27)$$

One notices that in region 3, $L_f=0$, so $F_{n,3}$ approaches $-\tanh(\lambda_n L_3)$ which is the same as solution in Tsay *et al.* (1989) for a channel without fibers present. In region 2, the hydraulic resistances for circular pores or rectangular slits, as the case maybe, are as follows:

$$R_2 = \frac{8\mu L_2}{\pi r_p^4}\left(\frac{2D}{L_j}\right) \qquad (4.28)$$

$$R_2 = \left(\frac{2D}{L_j}\right)\left(\frac{\mu L_2}{16b^3d}\right)\left[\sum_{m=0}^{\infty}\sum_{n=0}^{\infty} \frac{1}{(\alpha_n\beta_m)^2(\alpha_n^2+k^2\beta_m^2)}\right] \qquad (4.29)$$

The expression for hydraulic conductivity L_p for the entire cleft can thus be written as

$$L_p = [R_1 + R_2 + R_3]^{-1} \qquad (4.30)$$

4.2.4 Diffusive Permeability

An equivalent theory for solute diffusion through the junction-pore-matrix model proposed herein can be developed in a similar manner. Like the theory for water filtration just described, the theory for diffusion also includes: (i) the added resistance of a fiber layer at the cleft entrance and (ii) the diffusive resistance of the cleft with its junction strand. To solve the first problem, an approximate expression for the effective solute diffusivity $D_{i,eff}$ developed in Weinbaum *et al.* (1991) is applied in the region where the fibers are present. The second problem, the diffusive spreading of solute from the junction pores, closely parallels to the Hele-Shaw problem for water filtration just solved.

The approximate expression for $D_{i,eff}$ takes into account both the effect of the plasmalemma membranes and the fiber matrix. The restricted diffusivity D_{iw} derived in Ganatos *et al.* (1980, 81) for a sphere in a channel is used to describe the effect of the plasmalemma boundaries. For solutes moving in a confined fiber array, the effective diffusivity $D_{i,eff}$ is given by

$$D_{i,eff} = D_{iw} \frac{(1-b_1 S_e)/(1+b_1 S_e)}{(1+r_s/\sqrt{K_p}+r_s^2/3K_p)} \tag{4.31}$$

where the denominator describes the added resistance of the fiber matrix and the numerator describes the steric hindrance for a periodic fiber array. Here b_1 is the coefficient of the leading term of the pseudo doubly periodic Weierstrasse expansion series that is used to describe the disturbance produced by each fiber for the diffusion problem; $S_e=S(1+r_s/a)^2$ represents the effective fiber solid fraction; r_s is the solute radius; K_p is the Darcy permeability for the unbounded fiber array.

The boundary value problem for the diffusion of the solute through a cleft with a junction strand with periodic pores is similar to the equivalent Hele-Shaw problem for filtration. In the diffusion problem, instead of solving Laplace's equation for the pressure field, one solves equation (4.9) by satisfying boundary conditions similar to (4.10) through (4.15) for the concentration field. The drag coefficient $f = \mu_{eff}/\mu$ in the filtration problem is now equal to $D_{iw}/D_{i,eff}$. By following the same procedure as that summarized for the filtration problem, one obtains the following expression for diffusive permeability ω

$$\omega = (R_1 + R_2 + R_3)^{-1} \tag{4.32}$$

where

$$R_i = \frac{1}{2BL_jD_{iw}}\left[L_{w,i} + fL_{f,i} - \frac{2}{d^2}\sum_{n=1}^{\infty}\frac{F_{n,i}\sin^2(\lambda_n d)}{\lambda_n^3}\right],\ i=1,3 \quad (4.33)$$

In region 2, the diffusive resistances for circular pores and rectangular slits are given by,

$$R_2 = \frac{L_2}{\pi r_p^2}\left(\frac{2D}{L_j}\right)\frac{1}{D_2} \quad (4.34)$$

$$R_2 = \frac{L_2}{4bd}\left(\frac{2D}{L_j}\right)\frac{1}{D_2} \quad (4.35)$$

where D_2 is the restricted diffusion coefficient in the junction pore region. Approximate solutions for D_2 for circular pores and rectangular slits are given in Curry (1984).

4.3 Results and Discussion

The results shown in chapter 3 lead to the important conclusion that a simple one-dimensional model for a cleft that is filled entirely with a fiber matrix can not explain all the measured data for capillary transport. In order to reconcile the cleft structure with the measured transport properties, one also needs to consider the junction strand with its several different possible geometries. In particular, three types of junctional pores are examined: (i) a small circular pore representing individual missing proteins in an otherwise impermeable junction strand, (ii) a narrow rectangular slit of 8 nm width and 11, 44 or 88 nm length. These slit lengths correspond to 1, 4 and 8 missing proteins. (iii) a wider rectangular pore with 2, 4 or 8 missing proteins and a 22 nm slit height. The results will be presented for clefts: (i) with only a junction strand with pores, (ii) with fiber matrix components filling in the entire wide portion of the cleft and (iii) with a thin fiber layer at the entrance of the cleft. The cleft dimensions applied in the model are mainly based on the

measurements of Clough and Michel (1988) for frog mesentery capillary. The total cleft depth L is 400 nm, the channel height 2B=22 nm, and the total cleft length per unit capillary surface area is 2000 cm/cm^2. This data was selected since it was the first series of experiments in which morphometric electron microscopic measurement and capillary hydraulic permeability data were obtained for the same vessels. The measured value of L_p for frog mesentery in this study is 5.9 x 10^{-7} $cm/s/cm\text{-}H_2O$. There is still no experiment on an isolated vessel in which the diffusive permeability is measured in the same specimen for which the cleft dimensions are examined.

4.3.1 Cleft with Junction Strand Only

The results for the hydraulic conductivity L_p and the diffusive permeability ω for a cleft with junction strand only are presented in Figures 4.3(a,b), 4.4(a,b) and 4.5(a,b). The solid triangular symbols in Figures 4.3b, 4.4b and 4.5b are the measured values for the solute permeability given in Curry (1986) that have been obtained for a large spectrum of solutes up to the size of albumin, 3.5 nm in radius. The continuous theoretical curves for solute permeability ω use the Stokes-Einstein relation to determine the solute diffusion coefficient in an unbounded free solution. The open triangles are calculations of solute permeability coefficients based on the measured values of the free diffusion coefficients of the respective ions or solutes.

In Figure 4.3(a,b), solutions are presented for circular pores of three different radii. From Figure 4.3a, one notes that to achieve the measured value of L_p for frog mesentery, the spacings between junction pores, 2D, will be 42, 62 and 90 nm for the pores of 4.5, 5.0 and 5.5 nm in radius. These values of 2D are then applied in Figure 4.3b to obtain the predicted curves for solute diffusive permeability. A pore radius of 5.5 nm is about the size required for a circular cylindrical to be the primary molecular sieve in frog mesentery

capillary. Therefore, a cleft with pores of r_p=5.5nm and 2D=90 mm closely satisfies the measured values of L_p and reflection coefficient σ. However, the results shown in Figure 4.3b indicate that such a circular pore structure can not describe the full range of permeability data. The solution slightly overpredicts the measured values of ω for small and large solutes but substantially overestimates the measured values for intermediate size molecules (r_s = 0.5 - 2.5 nm).

In Figure 4.4(a,b), results are showed for slits of 8 nm height and 11, 44, and 88 nm length. These values correspond to periodic junction discontinuities of 1, 4, and 8 missing proteins. The 44nm wide break is typical of a single standard section thickness and thus might correspond to the larger gaps observed by Bundgaard (1984). For the 8 nm high slit, the model predicts that the spacing 2D of the 11, 44, and 88 nm breaks are approximately 68, 370, and 680 nm respectively. These values of 2D correspond to approximately 10 to 16 percent of the cleft being open. The theoretical curves shown in Figure 4.4b indicate that the rectangular slit model with 8 nm gap height only fits the measured data for ω for small solutes up to the size of sucrose (0.48 nm in radius). Then, the predictions start to deteriorate for larger solutes. One also observes in Figure 4.4b that the pores with smaller 2d appear to be more 'selective'. This follows from the fact that the contribution of the constricted pore region to the diffusive resistance for smaller pores is larger than that for a larger pore.

Results for the 22 nm high rectangular pore are showed in Figure 4.5(a,b). For the reasons mentioned in the introduction, this gap height is a more reasonable approximation for longer breaks of 44 and 88 nm than the 8 nm high slit. For this larger gap height, the junction pores will offer little resistance to water and solutes transport unless they are far apart. Results in Figure 4.5a indicate

that the 2D needed to achieve the measured value of L_p for strand breaks that are 22, 44, and 88 nm in length are 800, 1220, and 1650 nm respectively. The 2D needed for this type of pores is much larger than the 2D predicted by the small circular pores. Bundgaard did not systematically examine the frequency of the large breaks observed in his conventional thin sectioning experiments. However, he reported finding only six such large breaks in a total cleft length of about 8 μm in his rat heart capillary preparations. This gives 2D≈1300. The L_p for skeletal muscle capillaries is about one seventh of the L_p for frog mesentery capillaries. A junction pore model for a cleft with 22 x 44 nm slit pores predict 2D≈8000nm for muscle capillaries. This value of 2D is much larger than the value observed by Bundgaard. Therefore, to explain the discrepancy, one would think that part of the hydraulic resistance must be due to the presence of the fiber matrix. Also, because a pore of this size can not be the primary molecular sieve, a fiber matrix would need to be present somewhere in the junctional pathway. The results shown in Figure 4.5b indicate, not surprisingly, that a junction strand with large pores does not offer enough resistance for larger solutes and gives too much resistance for small ions. Also, because the gap width is the same as the background channel height, changing 2d will not alter the selective properties of the channel. One also observes that the theoretical curves for ω almost overlap for different 2d for the 22 nm gap height pores.

The fundamental difference between the present three-dimensional Hele-Shaw model and the traditional one-dimensional model for the hydrodynamic interaction with the junction strand is that the present model takes account of the lateral spreading of the water and solute in the wide part of the pore. The results in table 4.1(a,b) show this effect by comparing L_p and ω predicted by these two models for three different types of pores. Both tables show that for the larger 22 nm

high pore, the lateral spreading effect is very substantial. As shown in table 1a, the one-dimensional model overestimates $_pL$ by a factor of 3.5 for a rectangular pore of dimensions 22x44 nm and by a factor of 1.2 for a rectangular pore of dimensions 8x44 nm. The error for small ion permeability is even larger. This result strongly indicates the importance of lateral spreading in large pores that are infrequently spaced.

The results in Figure 4.3, 4.4 and 4.5 clearly indicate that even if one varies the pore cross-sectional shape, one can not explain all the measured transport coefficients. One can fit L_p and σ but not ω for all size solutes. In the pore model, the pores which are able to function as the molecular sieve, the 5.5 nm circular pores and the 8 nm slit pores, do not provide enough resistance for the intermediate size solutes. The pore of which provides the best agreement for the intermediate size molecules between 0.5-2.0 nm radius, the large 22 nm high pore,, does not provide the proper sieving properties. In contrast, in the fiber matrix model, a fiber matrix which fits L_p and σ does not offer enough resistance for small ion diffusion. Therefore, from the vantage point of either pore model or the fiber matrix model, one is led to a combined model for the cleft in which both junction strand and fiber matrix are present.

4.3.2 Cleft with Fiber Matrix Filling the Entire Wide Portion

In Figure 4.6(a,b), the solutions for the junction pore interaction are combined with the solution for μ_{eff} for the fibers in the wide part of the channel. Three sets of curves are shown, a junction strand with a circular cylindrical pore of 5.5 nm radius and two rectangular slit pores of 44 nm length, one with a gap height of 8 nm and the other an unconstricted height of 22 nm. Each set of curves shows the results for a combined junction-pore-matrix model with a=0.6 nm radius fibers of three different solid fractions filling the entire wide part of the cleft. The three fiber densities of S=0.001, 0.006,

and 0.017 correspond to an open spacing between fibers of Δ=32.4, 12.5, and 7 nm. The curves for S=0.001 (Δ=32.4nm) are nearly indistinguishable from the results shown in Figures 4.3 to 4.5 for a junction barrier with pores but no fibers. This is because a fiber matrix with $\Delta > 2B$ would offer very little resistance to both water and solute transport. For a fiber matrix to be able to serve as the primary molecular sieve, Δ would be about the size of the effective radius of an albumin molecule (d≈7nm). For 0.6 nm radius fibers this corresponds to a fiber solid fraction of 0.017. From Figure 4.6a, one observes that only the strand with unconstricted 22nm high pores can satisfy the measured value of L_p if a fiber matrix with S=0.017 is present in the wide part of the cleft. For S=0.017, the clefts with small pores of r_p= 5.5 nm or 2b=8nm fails to satisfy the measured L_p even when one half of the cleft is open. One also observes in Figure 4.6a that for 2D>200nm, all the L_p curves are parallel. This is due to the fact that when 2D becomes large, the junction pore interaction decreases. Therefore, the permeability becomes directly proportional to the junction pore frequency.

Solutions for P are shown in Figure 4.6b for those cases where the measure value of L_p can be achieved and either the pore size or the fiber spacing Δ is of the dimensions required to provide an adequate molecular sieve for albumin. Again, one finds that a pore-matrix model with fibers filling the entire wide portion of the cleft does not fit the data. The results for the 5.5 nm radius and 8nm gap height pores show that the addition of fiber matrix components in the wide part of the cleft leads to even larger deviations from the measured value of ω than the equivalent results for a cleft without matrix components. This occurs because the matrix contributes a larger resistance to water flow than to the diffusive resistance of small and intermediate solutes except in the limit where the solute

diameter approaches the open gap Δ. The results that indicate this behavior are shown in Figure 4.7.

In Figure 4.7, the effects of the fibers on the hydraulic and diffusive resistances are plotted for different fiber solid fractions. $R_{w\ fiber}$ represents the diffusive resistance for a cleft with fibers present and $R_{wo\ fiber}$ is that for a cleft without fibers present. The dashed curve shows the ratio of the hydraulic resistance for a cleft with fibers to that without fibers. This Figure shows that adding a fiber matrix into a cleft contributes a larger resistance to water flow than to a diffusive resistance for solutes when the solute size falls to the left of the dashed line. For example, for S=0.02, the fiber matrix contributes more to the hydraulic resistance than to the diffusive resistance for solute radius $r_s < 2.48$ nm.

One concludes from Figure 4.6 and 4.7 that including fibers throughout the wide part of the cleft can not resolve the difficulty in fitting the experimental data for the permeability of solutes greater than 0.5 nm radius. For the 5.5 nm circular pore and 8x22 nm rectangular slit pore, the addition of fibers leads to an even larger disagreement between theory and experiment. The junction pore structure which suggests the best agreement for ω for the intermediate size solutes is the large 22 nm high pore. The results in Figure 4.5b show that without adding fibers the model underpredicts ω for small ions whereas the results in Figure 4.6b indicate that adding a fiber matrix with Δ=7nm to the entire wide part of the cleft leads to an overestimate of ω for small ions. In order to correctly predict ω and, at the same time, preserve the proper sieving properties, we shall now examine what happens when we introduce a fiber matrix which fills only a portion of the cleft.

4.3.3 Cleft with Junction Strands and A Fiber Layer at the Cleft Entrance

The previous feasibility studies for the junction-pore model and the fiber matrix model suggest that a cleft with rectangular junction pores of 22x44 nm and a fiber matrix filling part of the cleft is the most likely structure to explain the existing data. To test this idea, one examines the effects of the following parameters:

(a) Relative Contribution of Junction Strand and Fiber Matrix Structures

In Figure 4.8, the results for ω are shown for clefts with different junction pore spacings. All the junction pore-matrix combinations shown here are first required to satisfy the measured L_p of 5.9×10^{-7} cm/s/cm-H_2O for frog mesentery capillary. Before the fiber matrix is added into a cleft, its hydraulic conductivity is denoted by L_{p0}. L_f is the thickness of the fiber layer. The fiber radius a=0.6 nm and S=0.035. This correspond to a dense matrix with Δ=4.5 nm. As shown in Figure 4.8, the L_p for a cleft without fibers or junction strands is 436 cm/s/cm-H_2O. Adding a fiber layer of 139 nm thickness to this cleft will reduce the value of L_p to the measured level. Other clefts with 22x44 nm junction pores and with 2D=260, 335, and 480 correspond to L_{p0}= 240, 200, and 150. The required value of L_f to achieve the measured L_p for each of these pore spacing is indicated. Finally, a cleft with 2D=1200 achieves the measured value of L_p without any fiber layer present.

The present model predicts that a cleft with 2D=480 nm and L_f=95nm can fit the measured value of ω for K^+ ions, 67-70 $\times 10^{-5}$ cm/s (Crone, 1978), using the measured value of its free molecular diffusion coefficient, see the open circles in Figure 4.8. Adamson (1990) observed a two to three fold increase in capillary L_p after partial degradation of the endothelial cell glycocalyx. For this cleft structure, the model predicts that $L_p$will be increased to L_{p0} =15 $\times 10^{-7}$cm/s/cm-H_2O when the matrix is degraded. The 2.5 fold

increase in L_p when the fiber layer is removed is thus in good agreement with Adamson's measurement.

(b) The effect of fiber radius

In Figure 4.9, the results for ω are shown for a cleft with a junction strand with pore spacing 2D=480 nm for the 22x44 nm pore. This junction structure fits the value of ω for small ions and also the measured value of L_p when the fiber matrix is degraded. Results for fiber matrices with fiber radii 0.6, 2.0, and 5.0 nm are plotted. The fiber densities are chosen to provide the same open spacing Δ=5 nm for different fiber radii. The results show that, although the fiber radii are different, the predicted curves for ω almost overlap. This clearly indicates that the open spacing Δ, and not the fiber radius or solid fraction S, is the most crucial parameter in determining the hydraulic and diffusive resistances of a fiber array. The solid lines shown in this Figure are obtained for the strand only model when L_p=15 and 6 x 10^{-7}cm/s/cm-H_2O. One notes that the solutions for clefts with fiber present approach the curve for the cleft with the same junction pore structure but without fiber present in the small ion region. Adding fibers to a cleft thus has little effect on the diffusive resistance of small solutes.

(c) The Effect of the Fiber Solid Fraction

While the results in Figures 4.8 and 4.9 for the 22x44 nm pore are able to predict both ω for small solutes and the changes in L_p that occur when matrix components are enzymatically degraded, none of the curves successfully predict ω for intermediate solutes with radii from 1.0 to 2.0 nm. All of these results indicate that the junction-pore-matrix structure in the present model does not offer enough resistance for these intermediate size molecules. In Figure 4.10(a,b), we have attempted to increase the diffusive resistances for the intermediate size molecules by substantially increasing the fiber solid fraction. For a constant fiber radius a=0.6nm, S has been

increased to 0.0415 for the periodic array (Δ=4 nm), Figure 4.10a, and S=0.2 for the random array, Figure 4.10b. In both cases, the results indicate that increases in S primarily improve the agreement for albumin, but have only a small effect on the intermediate size solutes.

4.4 Summary

The new models developed herein indicate that neither a junction-pore model with small pores of the required size to be the primary molecular sieve nor a simple fiber matrix model filling the entire cleft can explain all the measured data for L_p, ω, and σ. Feasibility studies show that a cleft with larger junctional breaks, typically 22x44nm, and a fiber layer at the cleft entrance is the most possible cleft structure to reconcile the structural and permeability data. A more sophisticated three-dimensional junction-pore-matrix model has been proposed to examine this hypothesis. In this model, a modified theory has been developed to examine the effects of an additional fiber layer at the entrance of the cleft. The Hele-Shaw model for junction pore interaction and the new analysis of the fiber matrix theory developed in chapter 3 are applied in this combined model. The results of this combined model show that although a cleft with large junctional gaps of 22x44nm and 2D=480nm and a fiber matrix with open spacing $\Delta \approx$ 7nm can fit the measured values for ω for small ions and large molecules of size close to albumin and the values for L_p with and without a surface fiber layer present, it can not also fit the measured values of ω for the intermediate size solutes between 1 and 2 nm radius. This difficulty is also encountered for both the three-dimensional junction-pore theory in chapter 2 and the new fiber matrix theory in chapter 3. It is now clear that by considering the hydrodynamic forces alone, a cleft with uniform size junctional pores and a fiber matrix layer does not offer enough diffusive resistance

for the intermediate size solutes. To resolve this discrepancy, several possibilities will need to be examined more carefully. First, in the present study, the solute molecules are treated as spherical particles. However, when the particle size becomes comparable to the pore size, the shape effects involved in the solute-pore interaction should provide additional resistance to the solute diffusion. Second, the surfaces of endothelial cells are known to carry a negative charge and the glycocalyx is associated with cation-binding sites. Therefore, the electro-hydrodynamic effect may also add additional forces affecting molecular diffusion. Finally, the present model indicates that by fitting the L_p and the ω for small ions, the cleft with a uniform size junction pore may not sufficiently general to account for the intermediate size solutes. Because the hydraulic resistance is proportional to r_p^4, while for the nonrestricted diffusion, the diffusive resistance is only proportional to r_p^2, increasing r_p will make the pore more permeable to water flow. One, therefore, suspects that there might be a multiple size pore system, which includes tiny pores which are permeable to the small ions and large pores which are responsible for most of the water flow. By examining these possibilities and designing future experiments based on the present study, one hopes that a self consistent picture will finally emerge for the structural pathways that determine capillary permeability.

Table 4.1:

A comparison of (a) the hydraulic conductivity L_p, (b) the diffusive permeability ω for K^+ ions predicted by the present three-dimensional model and the traditional one-dimensional model. R_w represents the hydraulic resistance at the wide part of the cleft and FR_n is the fraction of the resistance at the junction pore region.

(a)

		3-D Model			1-D Model		
Pore Size	2D	$L_p x10^8$	$R_w x10^{-8}$	FR_n	$L_p x10^8$	$R_w x10^{-8}$	FR_n
r_p=5.5nm	90nm	59.4	.31E-2	0.82	62.6	.22E-2	0.86
2b=8nm 2d=44nm	360nm	61.0	.45E-2	0.73	70.9	.22E-2	0.85
2b=22nm 2d=44nm	1200nm	61.1	.14E-1	0.15	215.	.22E-2	0.53

(b)

		3-D Model			1-D Model		
Pore Size	2D	$\omega x10^5$	$R_w x10^{-5}$	FR_n	$\omega x10^5$	$R_w x10^{-5}$	FR_n
r_p=5.5nm	90nm	94.2	.72E-2	0.32	117.	.51E-2	0.40
2b=8nm 2d=44nm	360nm	71.4	.10E-1	0.25	116.	.51E-2	0.41
2b=22nm 2d=44nm	1200nm	27.4	.33E-1	0.11	110.	.51E-2	0.44

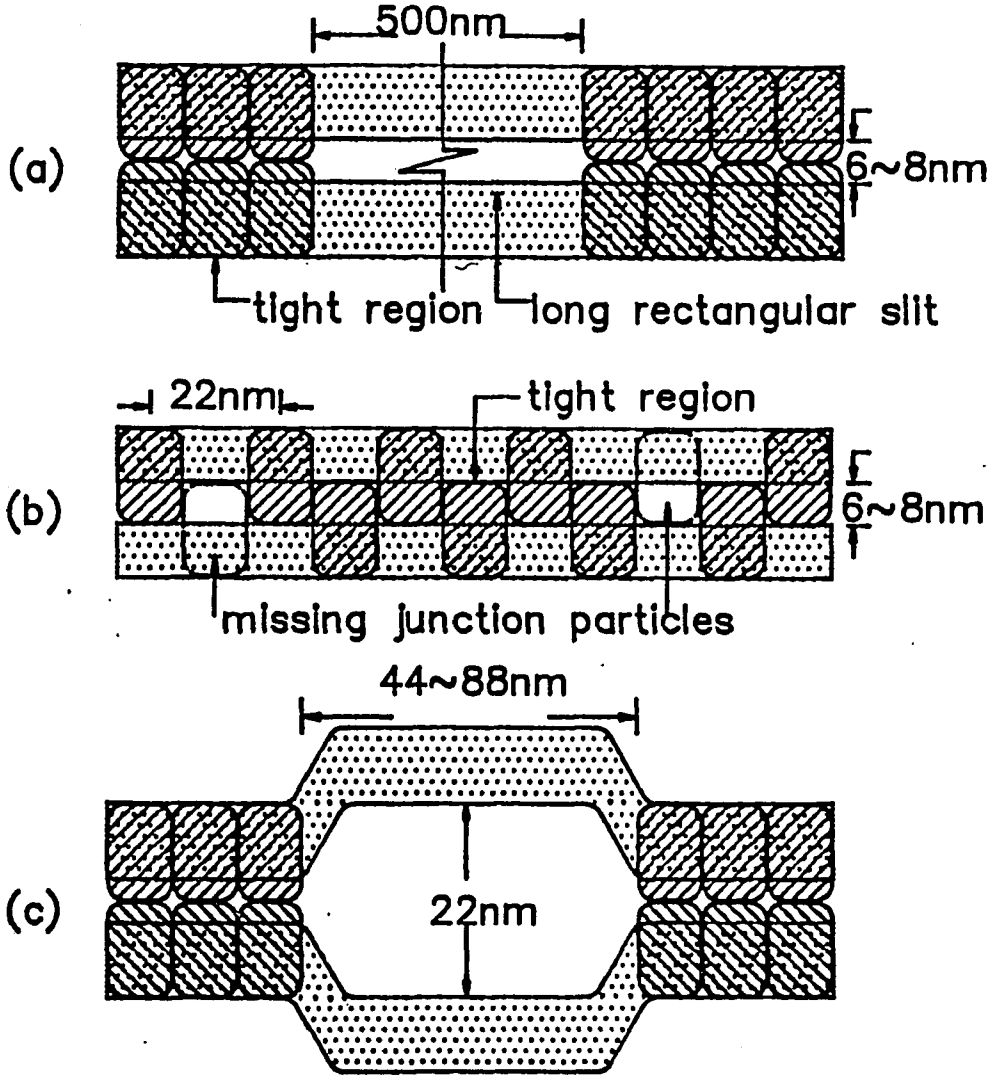

Fig.4.1: Three schematic diagrams of junction protein arrangement. These protein arrangement correspond to (a) the long rectangular junctional pores in a one-dimensional constricted channel model. (b) small gaps suggested by Bungaard's (1984) ultrathin sections. The zigzag protein pattern is first proposed in Tsay et al. (1989). (c) large pores with discontinuities of 44-88nm in protein strands.

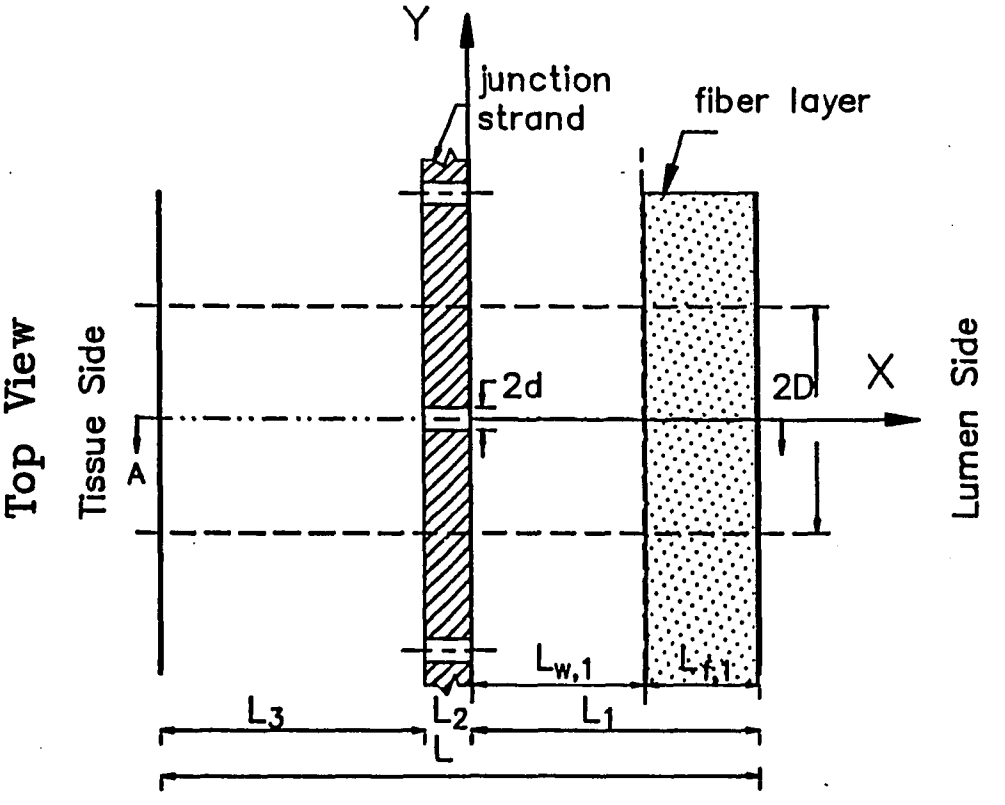

Fig.4.2: Sketch of the three dimensional junction-pore-matrix model of intercellular channel. A protein strand with periodic holes lies parallel to the luminal front,. L_2 is the depth of pores in protein strand and L_1 and L_3 are depths between protein strand and luminal and abluminal fronts. A portion of the wide part of the cleft is filled with cross-bridging fibers which are represented by either a periodic square array or a random array of cylindrical posts. The thickness of the fiber layer is L_f. The distance between two adjacent pores is 2D.

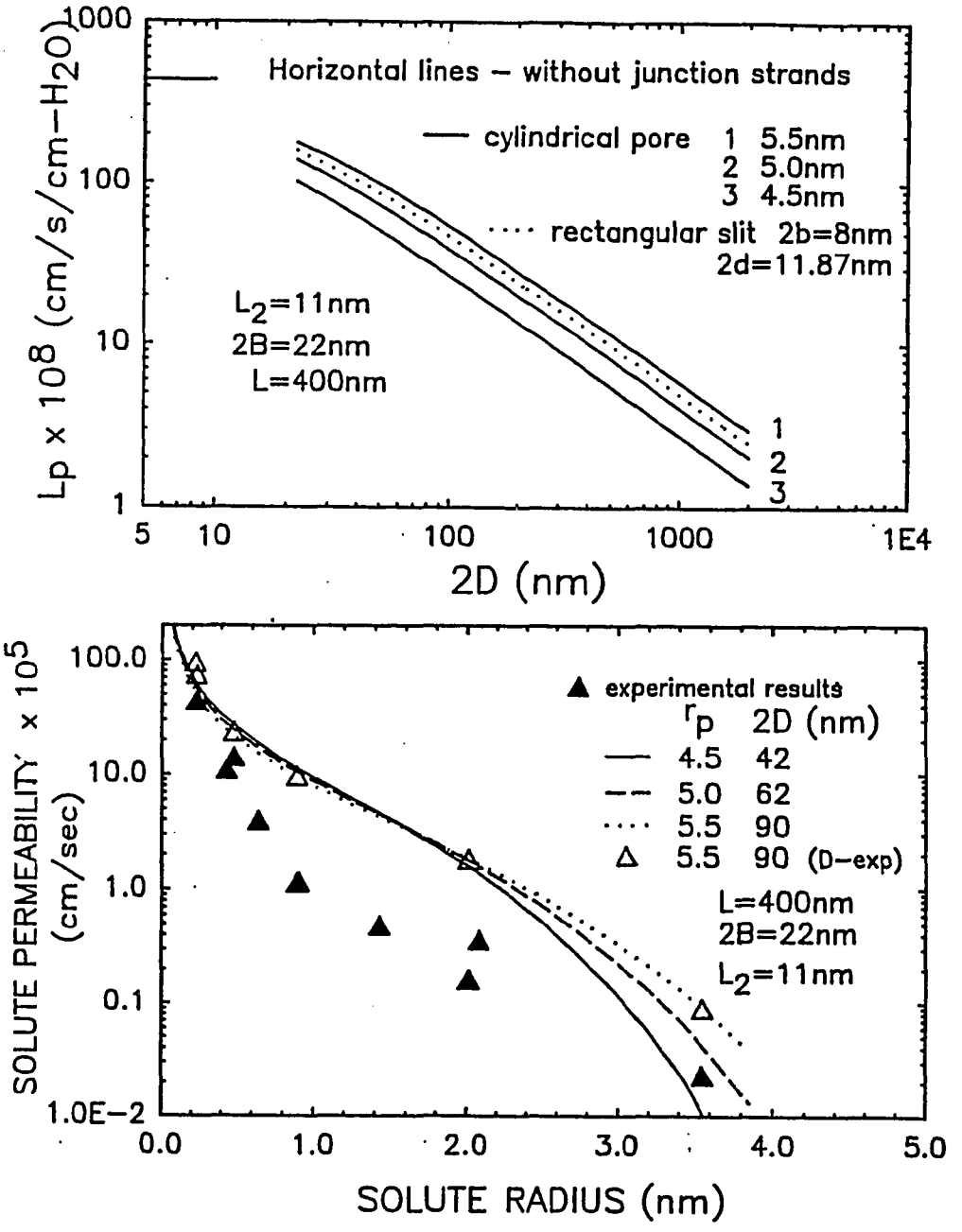

Fig.4.3: Solutions for the hydraulic conductivity and the diffusive permeability for clefts with circular pores in the junctional strands are presented in (a) and (b) respectively. Three different pore radii, r_p=4.5, 5.0 and 5.5, are shown. The spacing between pores, 2D, used in (b) is determined from (a) by fitting the hydraulic conductivity data for frog mesentery 5.9×10^{-7} cm/s/cm-H_2O. The solid triangles in (b) are directly measured values for the solute permeability. The open triangles are calculations of solute permeability based on measured values of the free diffusion coefficients of the respective ions or solutes. The continuous curves use the Stokes-Einstein relation to determine the solute diffusion coefficient.

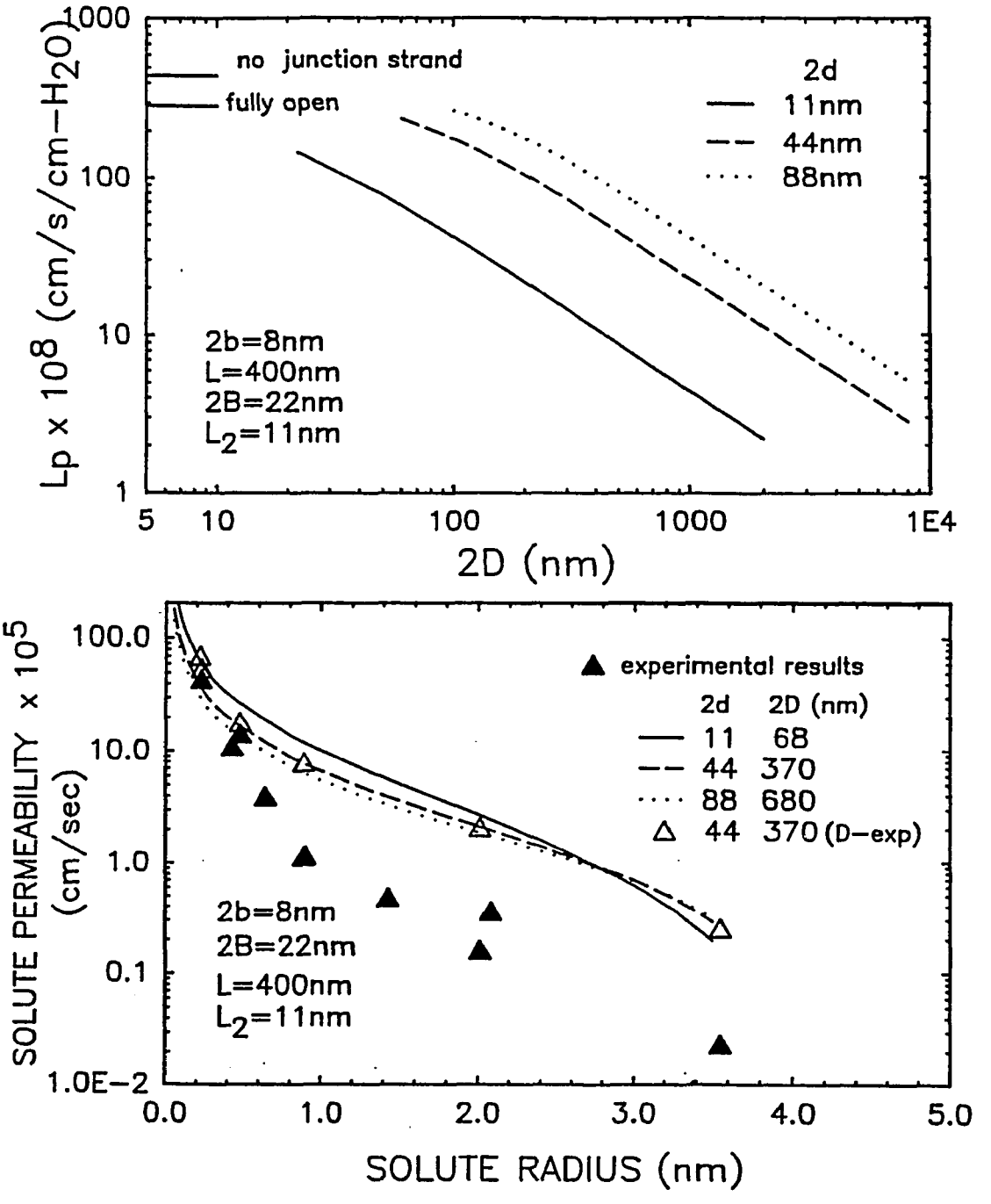

Fig.4.4: Solutions for the hydraulic conductivity and the diffusive permeability for clefts with 8 nm high rectangular junction pores are showed in (a) and (b). The 2D selected in (b) is determined from (a) by fitting the hydraulic conductivity data. Pores of 11, 44 and 88 nm wide are presented.

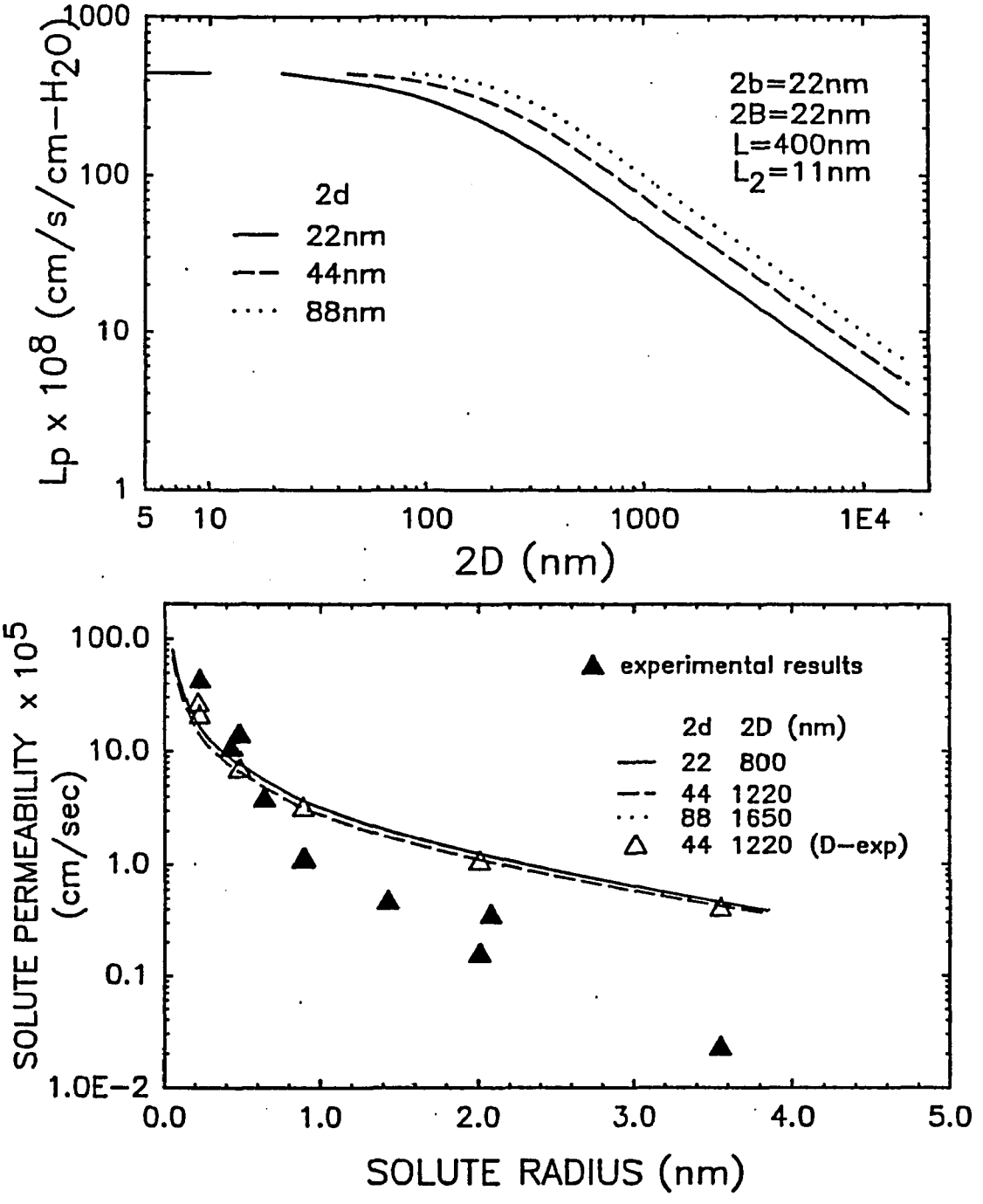

Fig.4.5: Solutions for the hydraulic conductivity and the diffusive permeability for clefts with 22 nm high rectangular junction pores are showed in (a) and (b). Similar to fig. 4.3 and 4.4, the 2D selected in (b) is determined from (a) by fitting the hydraulic conductivity data. Pores of 22, 44 and 88 nm wide are presented.

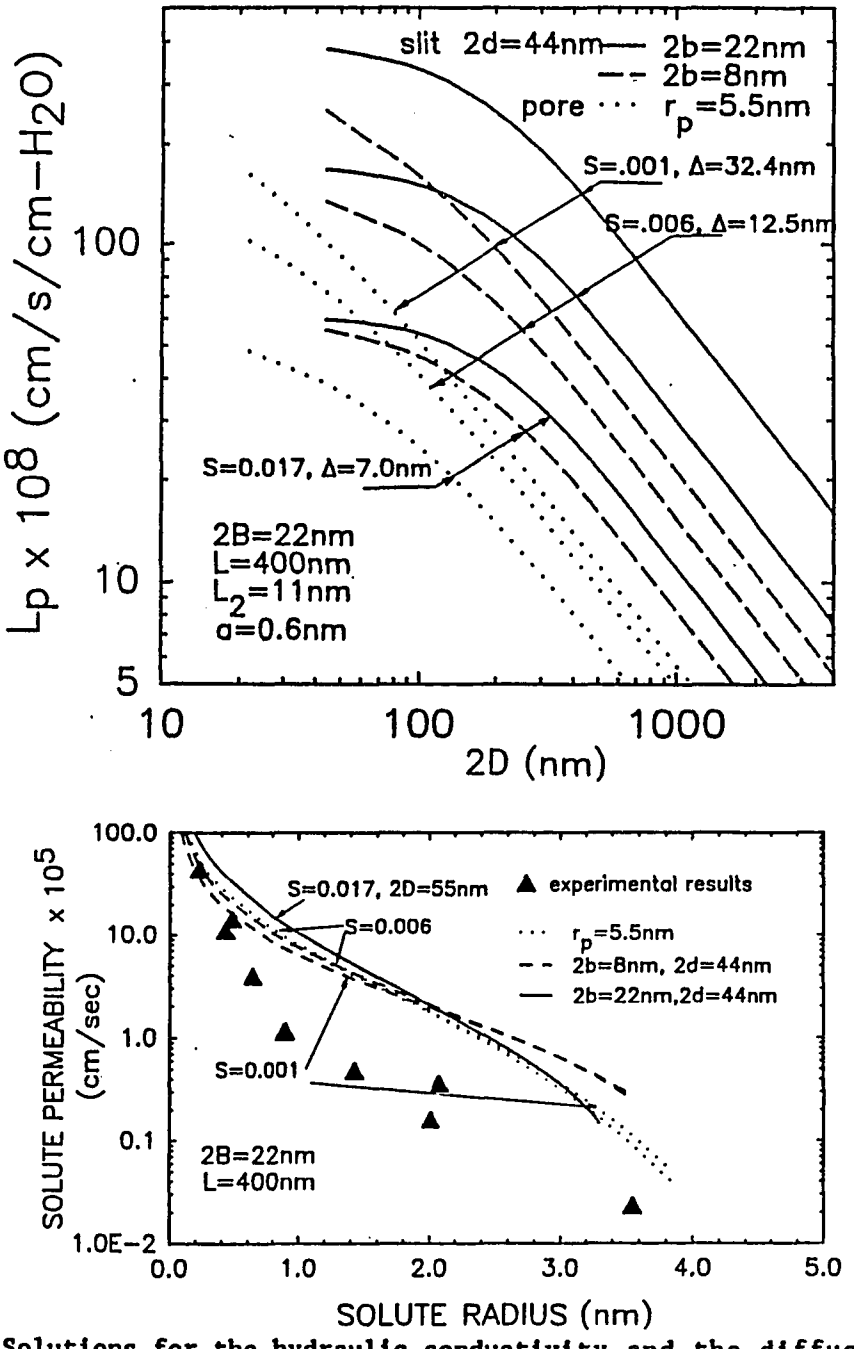

Fig.4.6: Solutions for the hydraulic conductivity and the diffusive permeability for clefts with junction strands and fiber matrix are presented in (a) and (b). Three sets curves, junction strands with circular pores of 5.5nm radius, with rectangular slit pores of 8x44 nm, and with slit pores of 22x44nm, are shown. In (a), each set of curves shows the results for a combined junction-pore-matrix model with three different fiber densities, S=0.001, 0.006 and 0.017. In (b), results are presented only for those cases in (a) where the measured value of L_p can be achieved and either the pore size or the fiber spacing Δ is of the dimensions for an adequate molecular sieve for albumin.

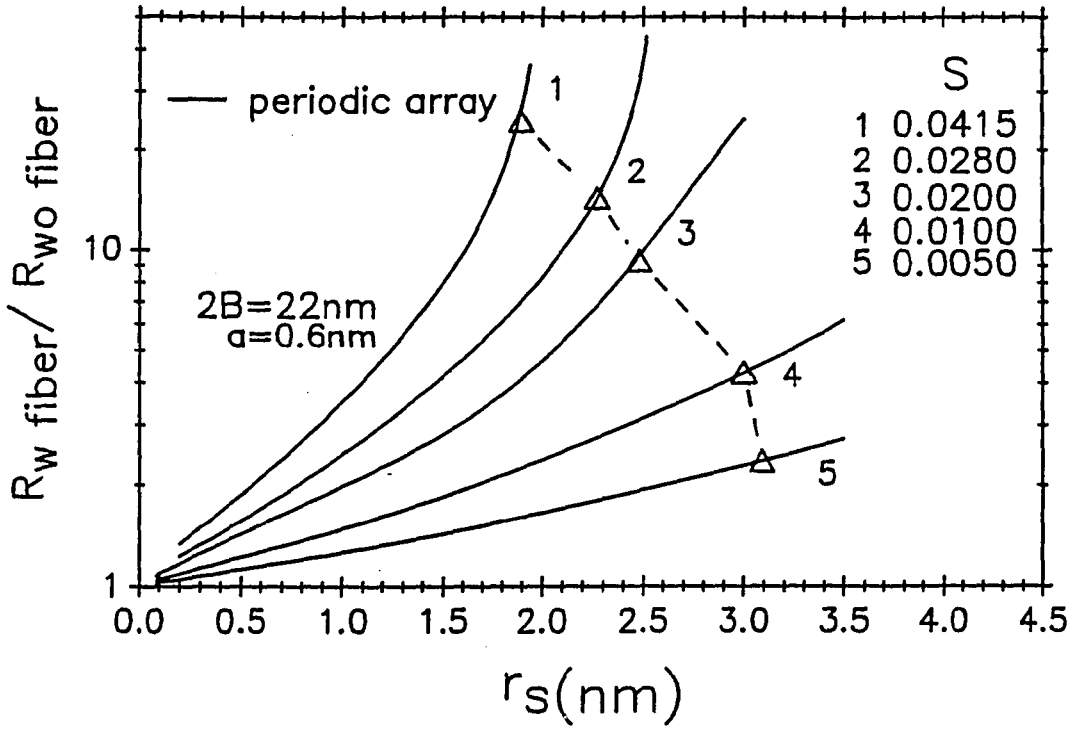

Fig.4.7: The effects of the fibers on the hydraulic and diffusive resistances are plotted for different S. $R_{w\ fiber}$ represents the resistance for a cleft with fibers present and $R_{wo\ fiber}$ denotes that for a cleft without fibers present. The solid curves show solutions for the ratio of diffusive resistances. The open triangles indicate the ratios of the hydraulic resistances.

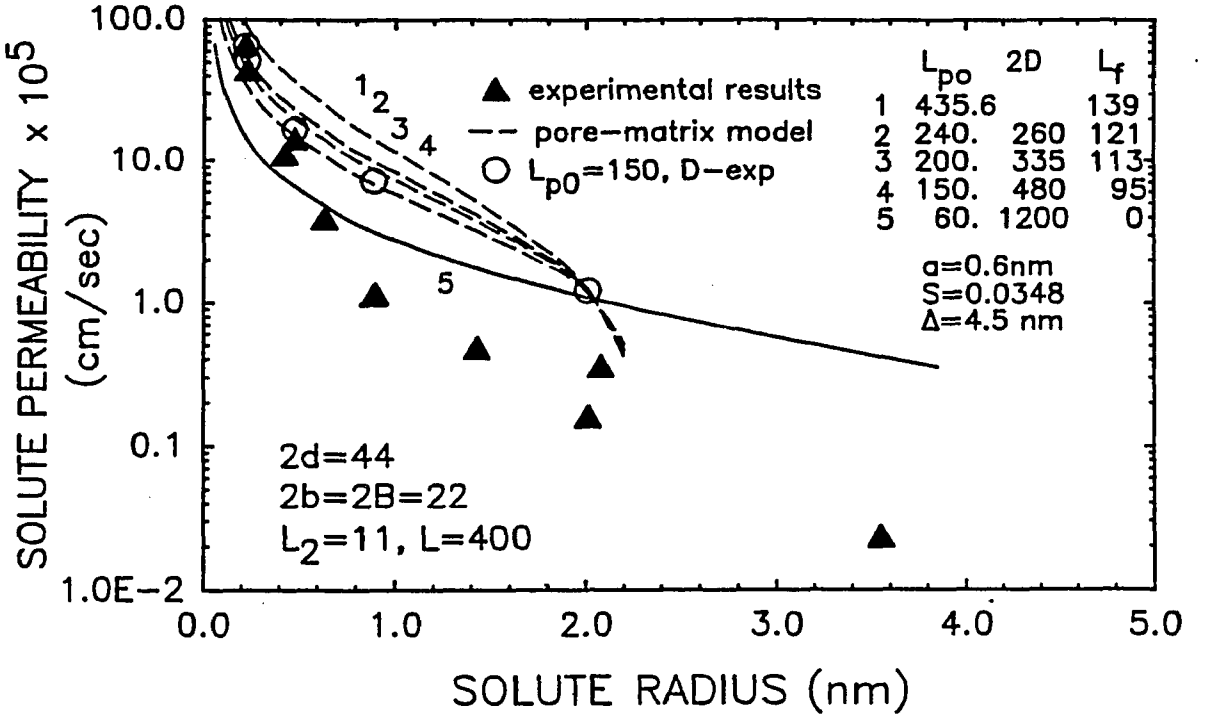

Fig.4.8: Solutions for ω are shown for clefts with different junction pore spacings, 2D. L_{p0} represents the hydraulic conductivity before the fibers are added into the cleft. The fiber layer thickness L_f are selected to satisfy the measured value of L_p for frog mesentery. The results are shown for a periodic fiber array with fiber radius a=0.6 nm and S=0.0348.

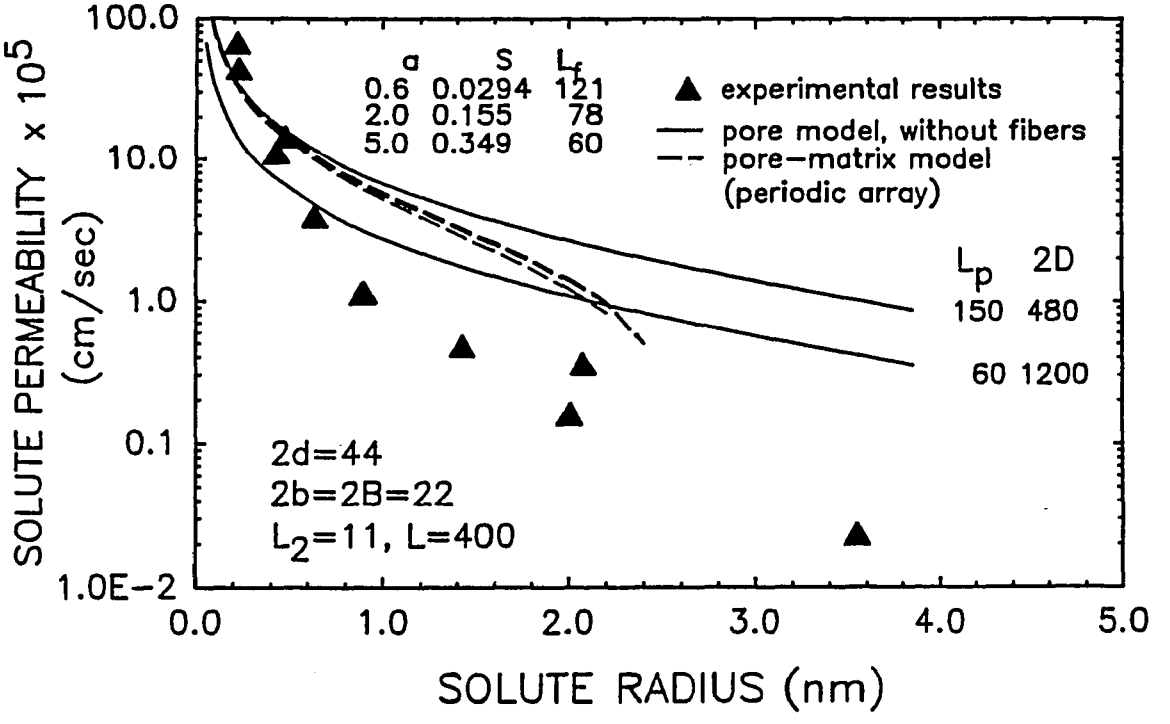

Fig.4.9: Solutions for ω are shown for a cleft with junction pores of 22 width and 44 nm length. The effects of fiber matrices with fiber radii 0.6, 2.0 and 5.0 are examined. The fiber densities are chosen to provide the same open spacing Δ=5 nm for different fiber radii.

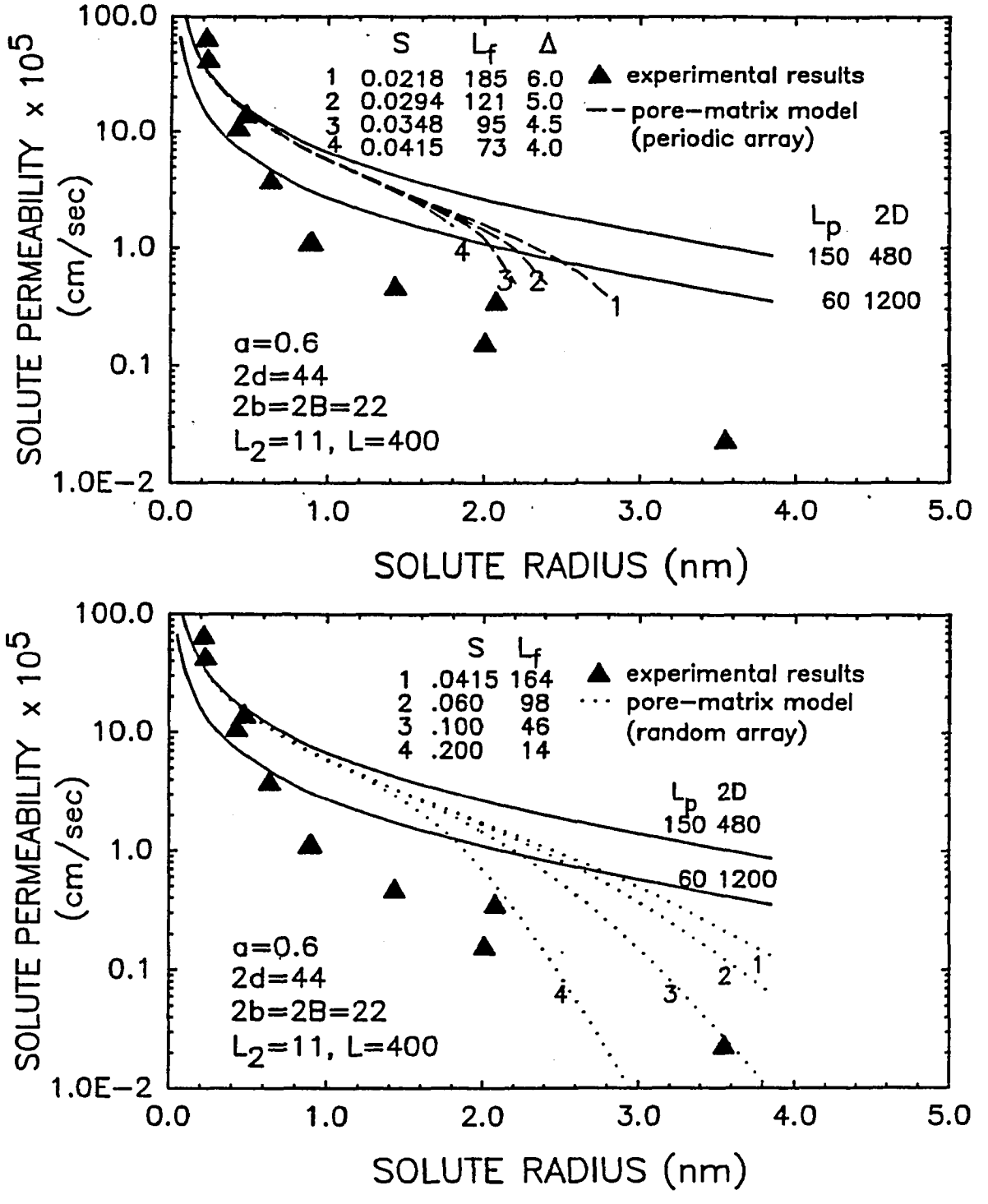

Fig.4.10: Solutions for ω for clefts with the same junctional pore structure but with different fiber densities are shown in (a) and (b). The results in (a) are for periodic fiber arrays and in (b) are for random fiber arrays.

CHAPTER V

SUMMARY

5.1 Conclusion

In summary, the present study has developed a three-dimensional model based on ultrastructure and microperfusion studies to examine the role of the intercellular cleft and its structural components in the regulation of capillary permeability. In this model, the transport behavior of a cleft with a junction strand with discrete pores and fiber matrix components in its wide parts is examined. Three different molecular models for the junction strand pores, a more frequent circular pore of 5.5 nm radius formed by isolated missing proteins, a restricted rectangular slit of 8 nm gap height and 1 to 8 missing proteins, and larger more infrequent breaks of 2 to 8 missing proteins with a gap height of 22 nm (the width of the wide part of the cleft), are analyzed. The fibers are assumed to fill all or a portion of the wide part of the cleft.

In chapter 2, a Hele-Shaw model is developed to examine the effects of a junction strand with its pores on the hydraulic conductivity of capillary interendothelial clefts. The results show that due to the lateral spreading at the entrances/exits of the junctional pores and the hydrodynamic interaction between them, the capillary permeability is not proportional to the length of the open junction. For a cleft with large infrequent pores, the lateral spreading effect can be very significant and traditional one-dimensional models can be off by a factor of two or more.

In chapter 3, new hydrodynamic theories have been developed to examine the effects of cross-bridging fibers in the wide part of the cleft. A rigorous solution for the viscous flow past a square array of circular cylindrical fibers confined between two parallel walls is obtained. This doubly periodic solution successfully describes the transition in behavior from the Hele-Shaw potential flow limit to the viscous two-dimensional limiting case for the hydrodynamic interaction between the fibers. These results are also compared with the solutions of the Brinkman approximation. The excellent approximation provided by the Brinkman approximation when $B/a > 5$ justifies the use of a Brinkman approach in developing the effective Darcy permeability $K_{p,eff}$ and the effective diffusive coefficient $D_{iw,eff}$ for a random fiber array. Also, an approximate hydrodynamic expression for the solute diffusion coefficient, which includes the far field hydrodynamic interaction of the surrounding fibers, has been proposed. For the random fiber array the results are close to those obtained using the stochastic approach of Ogston (1973).

The new theories developed herein indicate that neither a junction-pore model with small pores of the required size for these pores to be the primary molecular sieve nor a simple fiber matrix model filling the entire cleft can explain all the measured data for L_p, ω, and σ. Feasibility studies show that a cleft with larger junctional breaks, typically 22x44 nm, and a fiber layer at the cleft entrance is the most likely cleft structure to reconcile the structural and permeability data. In chapter 4, a more sophisticated three-dimensional junction-pore-matrix model has been proposed to examine this hypothesis. In this model, a modified theory has been developed to examine the effects of an additional fiber layer at the entrance of the cleft. The Hele-Shaw model for the junction pore interaction and the new analysis of the fiber matrix theory developed in chapter 3 are applied in this combined model. The results of this

combined model show that although a cleft with large junctional gaps of 22x44 nm with spacing 2D=480 nm and a fiber matrix with open spacing $\Delta \approx 7$nm can fit the measured values of ω for small ions and large molecules of size close to albumin and the measured values for L_p with and without a surface fiber layer present, it can not also fit the measured values for ω for the intermediate size solutes between 1 and 2 nm radius.

5.2 Future Studies

In the present study, a rigorous solution for the water filtration through a confined fibrous bed has been developed; however, the simplified theory proposed for solute diffusion is based on a Brinkman approximation which does not properly take into account the near field interaction between the solute and the fibers. In order to predict the solute diffusivity for solutes with size close to the open gaps between fibers, one needs to treat this problem properly. Also, shape effects will need to be more carefully studied especially for strong particle fiber interactions. It is now clear that by considering hydrodynamic forces alone, a cleft with uniform size junctional pores and a fiber matrix layer does not offer enough diffusive resistance for the intermediate size solutes. To know whether a multiple pore size system is feasible, or if there are other missing factors in the model, one needs to have a better knowledge of the detailed three dimensional structure of a junctional cleft. Based on the present theoretical work, three types of experiments are suggested in future studies: (i) Due to the heterogeneity of the microvascular bed, the capillary hydraulic conductivity and permeability should be measured in the same specimens for which morphological structural measurements are obtained. Also, the hydraulic conductivity and the diffusive permeability should be measured in the same single capillary microperfusion experiment. (ii)

Because of the limitation of the resolution of random section electron microscopic studies, the size and frequency of the junction pores need to be examined in serial section tracer experiments. Instead of observing the junction pores directly, one can attempt to reconstruct the tracer concentration profiles in the wake of the junction strand. A three-dimensional convective-diffusive model for this wake will need to be developed in the future. By matching the theoretical concentration profile with the shape of the experimental wake for tracer diffusion and convection, one should be able to estimate the size and frequency of the junction pores and the relative importance of convection and diffusion. (iii) In order to test for the location of the molecular filter, steady state ultrafiltration experiments need to be performed using electrondense macromolecules, such as myoglobin, HRP, or cytocrome C, as the test solute. A convective-diffusion model of osmotic structure at the pore entrance would then be used to predict the concentration distribution of the large molecules around the sites with the highest localized water flux.

Acknowledgement

Chapter 2 has been published as a paper (Tsay et al.) in Chemical Engineering Communication, 82, 1989. The portion of chapter 3 denoted to the hydraulic resistance has been published as part of a paper (Tsay and Weinbaum 1991) in the J. Fluid Mechanics 226, 1991. The material for diffusive resistance is part of the paper (Weinbaum *et al.* 1991) submitted for publication in Microvascular Research.

APPENDIX:

Orthorgonal expansions for the various functions of z appearing in equation (3.7)-(3.10) can be written in the form

$$1-\left(\frac{z}{B}^2\right) = \sum_{n=0}^{\infty} l_n \cos\lambda_n z$$

$$-\frac{1}{\alpha_j}\frac{dq_j}{dz} = \sum_{n=0}^{\infty} e_{jn}\cos\lambda_n z \qquad \text{(A.1)}$$

$$q_j(z) = \sum_{n=1}^{\infty} f_{jn} Y_n(z)$$

where λ_n is given by equation (3.13) and

$$l_n = \frac{32(-1)^n}{\pi^3(2n+1)^3}$$

$$e_{jn} = \frac{4(-1)^n\lambda_n\alpha_j}{B^2(\alpha_j^2-\lambda_n^2)^2} \qquad \text{(A.2)}$$

$$f_{jn} = \frac{8\sqrt{2}\nu_n^3\alpha_j^3}{B^2(\nu_n^4-\alpha_j^4)^2}\left[\tan\alpha_j B \coth\nu_n B - \frac{\alpha_j}{\nu_n}\right]$$

The expressions for $\bar{U}_{mn}$, $\bar{V}_{mn}$ and $\bar{W}_{mn}$ appearing in equation (3.31) are given by the following:

$$\bar{U}_{mn}(r) = l_n(\delta_{m1}+b_m r^{-2m}+\sum_{p=1}^{\infty} A_{mp} b_p r^{2m-2})$$

$$+ \frac{(2m-1)}{\lambda_n r}[c_{nm} K\lambda_{nm} + \sum_{p=1}^{\infty} B_{nmp} c_{np} I\lambda_{nm}] \qquad \text{(A.3)}$$

$$+ \text{Re} \sum_{j=1}^{\infty} \left[\frac{e_{jn}}{\alpha_j^2}(-d_{jm} DK\alpha_{jm} + \sum_{p=1}^{\infty} D_{jmp} d_{jp} DI\alpha_{jm})\right]$$

$$\tilde{V}_{mn}(r) = l_n(\delta_{m1} - b_m r^{-2m} + \sum_{p=1}^{\infty} A_{mp} b_p r^{2m-2})$$

$$+ \frac{1}{\lambda_n}\left[c_{nm} DK\lambda_{nm} + \sum_{p=1}^{\infty} B_{nmp} c_{np} DI\lambda_{nm}\right] \qquad (A.4)$$

$$+ \text{Re} \sum_{j=1}^{\infty} \left[\frac{(2m-1)e_{jn}}{\alpha_j^2 r}(-d_{jm} K\alpha_{jm} + \sum_{p=1}^{\infty} D_{jmp} d_{jp} I\alpha_{jm})\right]$$

$$\tilde{W}_{mn}(r) = \text{Re} \sum_{j=1}^{\infty} \frac{f_{jn}}{\alpha_j}(d_{jm} K\alpha_{jm} - \sum_{p=1}^{\infty} D_{jmp} d_{jp} I\alpha_{jm}) \qquad (A.5)$$

where

$$K\alpha_{jm} = \frac{K_{2m-1}(\alpha_j r}{K_{2m-1}(\alpha_j)} \qquad I\alpha_{jm} = \frac{I_{2m-1}(\alpha_j r)}{I_{2m-1}(\alpha_j)},$$

$$K\lambda_{nm} = \frac{K_{2m-1}(\lambda_n r}{K_{2m-1}(\lambda_n)} \qquad I\lambda_{nm} = \frac{I_{2m-1}(\lambda_n r)}{I_{2m-1}(\lambda_n)},$$

$$DK\alpha_{jm} = \frac{K'_{2m-1}(\alpha_j)}{K_{2m-1}(\alpha_j)} \qquad DI\alpha_{jm} = \frac{I'_{2m-1}(\alpha_j)}{I_{2m-1}(\alpha_j)},$$

$$DK\lambda_{nm} = \frac{K'_{2m-1}(\lambda_n)}{K_{2m-1}(\lambda_n)} \qquad DI\lambda_{nm} = \frac{I'_{2m-1}(\lambda_n)}{I_{2m-1}(\lambda_n)},$$

$$K_m' = \frac{dK_m}{dr}, \qquad I_m' = \frac{dI_m}{dr}.$$

BIBLIOGRAPHY

1. Adamson, R.H. (1990) J. Physiol., **428**, 1-13.
2. Anderson, J.L. and Malone, D.M. (1974) Biophys. J., **14**, 957-982.
3. Anderson, J.L. (1981) J. Theor. Biol., **90**, 405-426
4. Bird, R.B., Stewart, W.E. and Lightfoot, E.N. (1960) Transport Phenomena, John Wiley & Sons, New York..
5. Brinkman, H.C. (1947) Proc. K. Ned. Akad. Wet., **50**, No.6, 618-24, No7, 821.
6. Bundgaard, M. (1980) Annu. Rev. Physiol., **42**, 325.
7. Bundgaard, M. and Frokjaer-Jensen, J. (1982) Microvasc. Res., **23**, 1-30.
8. Bundgaard, M. (1984) J. Ultrastructure Res. **88**, 1-17.
9. Casely-Smith, J.R., Green, J.L., and Wadey, P.J. (1975) Microvasc. Res., **10**, 43-64.
10. Casely-Smith, J.R. and Caon, M. (1976) Microvasc. Res., **11**, 265.
11. Clough, G. and Michel, C.C. (1988) J. Physiol. **405**. 563-576.
12. Conte. S.D. and Boor, C.D. (1980) Elementary Numerical Analysis, McGrall-Hill, New York.
13. Crone, C. and Christensen, O. (1981) J. Gen. Physiol., **77**, 349.
14. Crone, C. (1984), in Recent Advance in Physiology, Churchill-Livingston, London, 125.
15. Crone, C. and Levitt, D. (1984): Capillary permeability to small solutes. in Handbook of Physiology (E.M. Renkin and C.C. Michel eds.), sect.2, The Cardiovascular System, Vol.4, The Microcirculation, Bethesda, Md, American Physiological Society, 411-466.
16. Curry, F.E., Mason, J.C., and Michel, C.C. (1976) J. Physiol. London, **261**,319.
17. Curry, F.E. and Michel, C.C. (1980) Microvasc. Res., **20**, 96-99.
18. Curry, F.E. and Stoklosa, R.T. (1981) Microvasc. Res. **21**, 240-241, (Abstract).
19. Curry, F.E., Huxley, V.H. and Adamson, R.H. (1983) Am. J. Physiol., **245**, H495-505.
20. Curry, F.E. and Frokjaer-Jensen, J. (1984) J. Physiol. London, **305**, 293.
21. Curry, F.E. (1984): Transcapillary exchange. in Handbook of Physiology (E.M. Renkin and C.C. Michel eds.), sect.2, The Cardiovascular System, Vol.4, The Microcirculation, Bethesda, Md, American Physiological Society, 309-374.
22. Curry, F.E. (1985) Fed. Proc., 44,, 2610.

23. Curry, F.E., (1986) Circ. Res. **59**, 367-380.

24. Curry, F.E., Michel, C.C., and Phillips, M.E. (1987) J. Physiol., **387**, 69-82.

25. Dagan, Z., Weinbaum, S., and Pfeffer, R. (1982) J. Fluid Mech., **115**, 505-523.

26. Drummond, J.E. and Tahir, M.I. (1984) J. Multiphase flow, **10**, No 5, 515.

27. Ethier, C.R. and Kemm, R.D. (1989) PhysicoChemical Hydrodynamics, **11**, 219.

28. Firth, J.A., Bauman, K.F., and Sibley, C.P. (1983) J. Ultrastructure Res., **85**, 45-57.

29. Fung, Y.C. and Sobin, S.S. 1969 J. Appl. Physiol. **26**, 472.

30. Ganatos, P., Weinbaum, S., and Pfeffer, R. (1980) J. Fluid Mech., **99**, part 4, 755-783.

31. Ganatos, P., Weinbaum, S., Fischbarg, J. and Liebovith, L. (1981) Adv. Bioengng., 3, 193-196.

32. Gingell, D. (1976) in Mammalian Cell Membranes, edited by G.A. Jamieson and D.M. Robinson, Boston, 1, 198-223.

33. Gosslin, R.E. and Stibitz, G.R. (1977) Microvasc. Res., 14, 363.

34. Happel, J. (1959) AIChE J., **5** ,174-177.

35. Happel, J. and Brenner, H. (1973) Low Reynolds Number Hydrodynamics, 2nd edn, Printice-Hall, Englewood, Cliffs N.J.

36. Hele Shaw, H.S. (1898) Nature, **58**, 34.

37. Hsiung, C.C. (1984) Ph.D. Thesis, Columbia University, New York.

38. Karnovsky, M.J. (1967) J. Cell Biol. **35**, 213-236.

39. Karnovsky, M.J. (1968) J. Gen. Physiol., **52**, 645.

40. Keller, H. and Sachs, D. (1964) J. Appl. Phys., **35**, 537.

41. Kuwabara, S. (1959) J. Phys. Soc. Japan, 14, No 4, 527.

42. Landis, E.M. and Pappenheimer, (1963): Exchange of substances through the capillary walls. in Handbook of Physiology. Circulation, edited by W.F. Hamilton, Washington, DC, Am. Physiol. Soc. sect. 2, 2, 961-1034.

43. Lassen, N.A. and Trap-Jensen, J. (1970) in Capillary Permeability, edited by C. Crone and N.A. Lassen, Copenhagen, Munksgaard, 647.

44. Larson, R.E. and Higdon, J.L. (1986) J. Fluid Mech., **166**, 449.

45. Lee, J.S. (1969) J. Biomech., 2, 187-198.

46. Lee, J.S. and Fung, Y.C. (1969) J. Fluid Mech., **37**, 657-672.

47. Levitt, D.G. (1975) Biophys. J., 15, 533-563.

48. Luft, J.H. (1966) Fed. Proc., **25**, 1773-1788.

49. Michel, C.C., Mason, J.C. Curry, F.E. and Tooke, J.E. (1974) Q. J. Exp. Physiol., **59**, 283-309.

50. Michel, C.C. (1978) Arch. Int. Physiol. Biochem., **86**, 657.

51. Michel, C.C. (1979) Acta Physiol. Scand. Suppl., **463**, 67.

52. Michel, C.C. (1980) J. Physiol., **309**, 341.

53. Michel, C.C. (1984): Fluid movements through capillary walls. in Handbook of Physiology (E.M. Renkin and C.C. Michel eds.), sect.2, The Cardiovascular System, Vol.4, The Microcirculation, Bethesda, Md, American Physiological Society, 375-410.

54. Michel, C.C. (1985) The Malpighi Award Lecture, Int. J. Microcirc. Clin. Exp. 4, 265-284.

55. Neale, G. and Nader, W. (1974) Can. J. Chem. Engng. **52**, 475.

56. O'Brien, R.W. (1979) J. Fluid Mech., **91**, part 1, 17.

57. Ogston, A.G., Preston, B.N., and Wells, J.D. (1973) Proc. R. Soc. London, ser. **A333**, 297-316.

58. Paine, P.L. and Scherr, P. (1975) Biophys. J., 15, 1087.

59. Palade, G.E., Simionescu, M. and Simionescu, N. (1979) Acta Physiol. Scand. Suppl. **463**, 11-32.

60. Pappenheimer, J.R., Renkin, E.M. and Borrero, L.M. (1951) Am. J. Physiol. **167**, 13-46.

61. Pappenheimer, J.R. (1953) Physiol. Rev., **33**, 387.

62. Perl, W. (1971) Microvasc. Res., 3, 233-251.

63. Perrins, W.T., McKenzie, D.R., and McPhedran, R.C. (1979) Proc. R. Soc. London, **A369**, 207.

64. Perry, M.A. (1980) Microvasc. Res., **19**, 142-157.

65. Rayleigh, R.S. (1892) Phil. Mag., **34**, 481.

66. Renkin, E.M. (1977) Circ. Res., **41**, 735-743.

67. Renkin, E.M., and Curry, F.E. (1978) in Transport Across Biological Membranes: Transport Organs, edited by G. Giebisch and D.C. Tosteson. Berlin: Springer-Verlag, 4, 1.

68. Rippe, B. and Haraldsson, B. (1983) Acta Physiol. Scand. Suppl., **508**, 60.

69. Sangani, A.S. and Acrivos, A. (1982) Int. J. Multiphase Flow, 8, 193-206.

70. Schneeberger, E. E. and Hamelin, M. (1984) Am. J. Physiol., 247, H206-217.

71. Sibley, C.P., Bauman, K.F. and Firth, J.A. (1982) Cell Tissue Res., **223**, 165-178.

72. Sibley, C.P., Bauman, K.F. and Firth, J.A. (1983) Cell Tissue Res., **229**, 365-377.

73. Silberberg, A. (1987) in Microcirculation - an update, edited by M. Tsuchiya et al., Elsevier, Amsterdam, 1, 153-154.

74. Simionescu, M., Simionescu, N., and Palade, G.E. (1975) J. Cell Biol., 67, 863.

75. Simionescu, M., Simionescu, N., Silbert, J.E. and Palade, G.E. (1981) J. Cell Biol. 90, 614-621.

76. Simionescu, M., Simionescu, N. (1984): Ultrastructure of the microvascular wall: functional correlations. in Handbook of Physiology (E.M. Renkin and C.C. Michel eds.), sect.2, The Cardiovascular System, Vol.4, The Microcirculation, Bethesda, Md, American Physiological Society, 41-101.

77. Simionescu, M., Simionescu, N., Santoro, F. and Palade, G.E. (1985) J. Cell Biol. 100, 1396-1407.

78. Simionescu, N. (1983) Physilo. Rev. 63, 1536-1579.

79. Southard, T.H. (1964) In Handbook of Mathematical Functions edited by M. Abrambowitz and I.A. Stagun, Dover, New York. 627

80. Spielman, L. and Goren, S.L. (1968) Envir. Sci. Tech., 2, No 4, 279.

81. Starling, E.H. (1909): The Fluid of body. London, Constable, 186.

82. Sullivan, R.R. and Hertel, K.L. (1942) Adv. Colloid Sci., 1, 37.

83. Thompson, B.W. 1968 J. Fluid Mech. 31, 397.

84. Tsay, R., Weinbaum, S., and Pfeffer, R. (1989) Chem. Eng. Comm. 82, 67-102.

85. Tsay, R., Weinbaum, S. (1991) J. Fluid Mech, 226.

86. Turner, M.R., Clough, G. and Michel, C.C. (1983) Microvasc. Res. 25, 205-222.

87. Vargas, F., and Blackshear, G. (1980) Am. J. Physiol., 239, H464.

88. Ward, B.J., Bauman, K.F., and Firth, J.A. (1988) Cell Tissue Res., 252,57-66.

89. Watson, G.N. 1980 : A Treatise on the Theory of Bessel Functions. Cambridge University Press, England.

90. Weinbaum, S. 1980 J. Theor. Biol. 83, 63.

91. Weinbaum, S., Tzeghai, G., Ganatos, P., Pfeffer, R. and Chen, S. (1985) Am. J. Physiol. 248, H945.

92. Weinbaum, S., Ganatos, P. and Yan, Z.Y. (1990) Annu. Rev. Fluid Mech. 22, 275.

93. Weinbaum, S., Tsay, R. and Curry, F.E. (1991) submitted to Microvasc. Res. for publication.

94. Whittaker, E.T. and Watson, G.N. (1944) A Course of Modern Analysis. Cambridge University Press, England.

95. Wissig, S.L. (1979) Acta Physiol. Scand. Supply., 463, 33-44.

96. Yan, Z.Y., Weinbaum, S. and Pfeffer, R. (1986) J. Fluid Mech. **162**, 415.

97. Yu, C.P. and Soong, T.T. (1975) J. Appl. Mech., Trans, ASME, June 301-304.